AD-A143 001   SIMULATIONS OF EROSION/CORROSION SURFACE CHEMICAL   1/2
REACTIONS WITH A LASER BEAM(U) LAWRENCE LIVERMORE
NATIONAL LAB CA C W PRICE 01 NOV 83 UCRL-53468
UNCLASSIFIED   ARO-15812.7-MS MIPR-26-78   F/G 7/4   NL

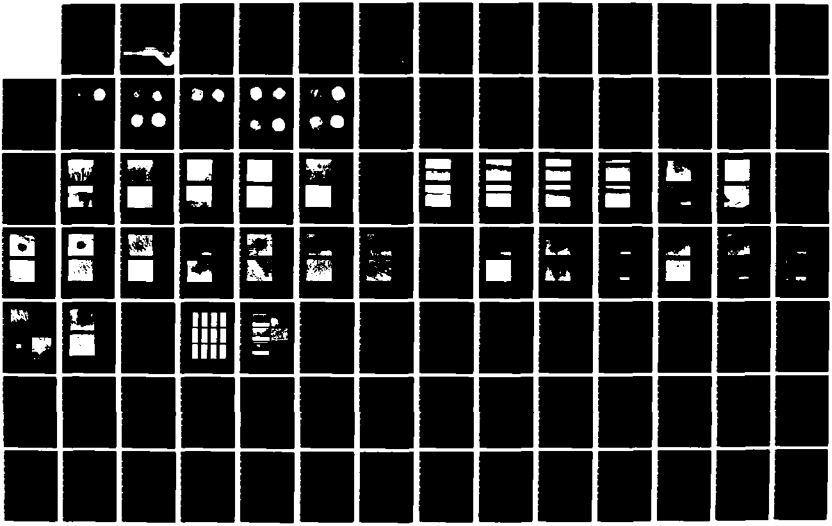

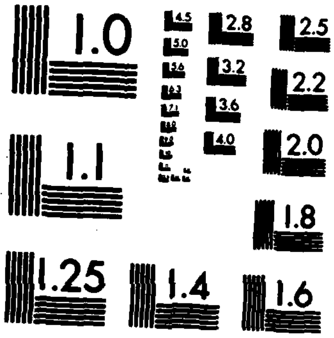

MICROCOPY RESOLUTION TEST CHART
NATIONAL BUREAU OF STANDARDS-1963-A

ARO 13012.7-MS

UCRL-53468

②

Simulations of Erosion/Corrosion Surface Chemical Reactions with A Laser Beam

C. W. Price

November 1, 1983

Lawrence Livermore National Laboratory

This document has been approved for public release and sale; its distribution is unlimited.

DISCLAIMER

Work performed under the auspices of the U.S. Department of Energy by Lawrence Livermore National Laboratory under Contract W-7405-Eng-48.

UNCLASSIFIED
SECURITY CLASSIFICATION OF THIS PAGE (When Data Entered)

AD-A143001

REPORT DOCUMENTATION PAGE

READ INSTRUCTIONS
BEFORE COMPLETING FORM

1. REPORT NUMBER ARO 15812.7-MS	2. GOVT ACCESSION NO. N/A	3. RECIPIENT'S CATALOG NUMBER N/A
4. TITLE (and Subtitle) Simulations of Erosion/Corrosion Surface Chemical Reactions with A Laser Beam		5. TYPE OF REPORT & PERIOD COVERED Technical Report
		6. PERFORMING ORG. REPORT NUMBER
7. AUTHOR(s) C. W. Price		8. CONTRACT OR GRANT NUMBER(s) MIPR 26-78, 27-80, 8-81 5-82
9. PERFORMING ORGANIZATION NAME AND ADDRESS Calif, Univ-Livermore		10. PROGRAM ELEMENT, PROJECT, TASK AREA & WORK UNIT NUMBERS
11. CONTROLLING OFFICE NAME AND ADDRESS U. S. Army Research Office Post Office Box 12211 Research Triangle Park, NC 27709		12. REPORT DATE Nov 83
		13. NUMBER OF PAGES
14. MONITORING AGENCY NAME & ADDRESS(if different from Controlling Office)		15. SECURITY CLASS. (of this report) Unclassified
		15a. DECLASSIFICATION/DOWNGRADING SCHEDULE

16. DISTRIBUTION STATEMENT (of this Report)

Approved for public release; distribution unlimited.

17. DISTRIBUTION STATEMENT (of the abstract entered in Block 20, if different from Report)

NA

18. SUPPLEMENTARY NOTES

The view, opinions, and/or findings contained in this report are those of the author(s) and should not be construed as an official Department of the Army position, policy, or decision, unless so designated by other documentation.

19. KEY WORDS (Continue on reverse side if necessary and identify by block number)

20. ABSTRACT (Continue on reverse side if necessary and identify by block number)

Surface chemical reactions in highly transient reactive environments frequently contribute to material degradation and subsequent loss by erosion/corrosion mechanisms. An attempt was made to simulate these reactions with a pulsed laser system in a pressure chamber. Gaseous carburizing and nitriding reactions were studied because of their frequent occurrence in erosion/corrosion environments. Reactions in pure iron and AISI 4340

DD FORM 1473 1 JAN 73 EDITION OF 1 NOV 65 IS OBSOLETE

UNCLASSIFIED
SECURITY CLASSIFICATION OF THIS PAGE (When Data Entered)

ARO 15812.7-MS

20. ABSTRACT CONTINUED:

steel were characterized by secondary ion mass spectroscopy (SIMS), optical metallography, and scanning electron microscopy (SEM). Gases used for laser-pulsing included argon, methane, carbon monoxide, ammonia, and nitrogen. The effect of gas pressure also was investigated. The results demonstrate that significant amounts of the reactive species can be driven into metal surfaces if the energy of the laser pulse exceeds the threshold for surface melting to occur. Specimen response appears to be reproducibly sensitive to the environment even in the relatively short time frame of the 600-μs laser pulse. Tests also were performed on ~~AISI 4340~~ steel specimens coated with tungsten to demonstrate the capability of the laser system to test candidate coating materials.

UCRL-53468
Distribution Category UC-25

Simulations of Erosion/Corrosion Surface Chemical Reactions with A Laser Beam

C. W. Price

Manuscript date: November 1, 1983

In partial fulfillment of a final report for the
Army Research Office under Contract No. 15812-MS

LAWRENCE LIVERMORE NATIONAL LABORATORY
University of California • Livermore, California • 94550

Available from: National Technical Information Service • U.S. Department of Commerce
5285 Port Royal Road • Springfield, VA 22161 • $13.00 per copy • (Microfiche $4.50)

Contents

Simulations of Erosion/Corrosion Surface Chemical Reactions with A Laser Beam

Abstract

Surface chemical reactions in highly transient reactive environments frequently contribute to material degradation and subsequent loss by erosion/corrosion mechanisms. An attempt was made to simulate these reactions with a pulsed laser system in a pressure chamber. Gaseous carburizing and nitriding reactions were studied because of their frequent occurrence in erosion/corrosion environments. Reactions in pure iron and AISI 4340 steel were characterized by secondary ion mass spectroscopy (SIMS), optical metallography, and scanning electron microscopy (SEM). Gases used for laser-pulsing included argon, methane, carbon monoxide, ammonia, and nitrogen. The effect of gas pressure also was investigated. The results demonstrate that significant amounts of the reactive species can be driven into metal surfaces if the energy of the laser pulse exceeds the threshold for surface melting to occur. Specimen response appears to be reproducibly sensitive to the environment even in the relatively short time frame of the 600-μs laser pulse. Tests also were performed on AISI 4340 steel specimens coated with tungsten to demonstrate the capability of the laser system to test candidate coating materials.

Introduction

Many military devices are either exposed to or operated in highly transient reactive environments that generate extensive material degradation by the simultaneous occurrence of erosion and corrosion mechanisms. Pulsed high-temperature combustion environments are typical examples of processes that generate such environments. The flow of particulate material during high-temperature high-pressure gas pulses can cause serious material loss by erosion. In reactive environments, the occurrence of erosion is suspected to periodically expose fresh surfaces on the substrate material for surface chemical reactions to occur. These surface reactions can significantly alter the composition of the substrate material and exert an important influence on erosion/corrosion mechanisms. However, the extent to which these reactions occur and the effect they have on erosion/corrosion mechanisms are not clearly defined. Therefore, a laser pressure-chamber system was developed to simulate selected transient reactions that occur in gaseous erosion/corrosion environments.

Although most erosion/corrosion mechanisms operate in a dynamic flow environment, the laser system operates in a quasi-static gas environment. However, the thermal pulse of the laser system is considered to be similar to thermal pulses encountered in many highly transient erosion/corrosion conditions, and thermal gradients induced in specimens pulsed with a laser beam closely resemble those encountered by critical components during actual operation. Experiments performed in the early phases of this program[1] demonstrated that the laser system was a viable tool for these simulations.

Various types of gaseous surface chemical reactions can occur in erosion/corrosion environments. Some of these reactions are discussed in Appendix 1. Unfortunately, the reactions that operate in an erosion/corrosion environment are difficult to predict from static experimental data. However, the identity of the surface chemical reactions that occur in erosion/corrosion is perhaps not as important as the extent to which they alter the surface and particularly the subsurface composition. In fact, material loss by erosion/corrosion mechanisms is strongly affected by subsurface mechanisms. Therefore, the success of this program ultimately requires that the extent to which surface chemical reactions alter subsurface properties and the subsequent effect on the operative erosion/corrosion mechanisms be identified. This also dictates that the material parameters that control these mechanisms be properly isolated. This is a difficult task, however, because many of the practical materials used for erosion/corrosion applications, such as steels, have complex microstructures. These microstructures are difficult to analyze unambiguously, particularly when attempting to isolate the subtle microstructural and chemical changes that occur during erosion/corrosion reactions. Therefore, an attempt was made to utilize simplified model materials and reactions. A sealed, high-pressure chamber was developed for simulating high-pressure and energy-pulse environments.

The substrate materials selected were pure iron and AISI 4340 steel. Pure iron was selected to enhance the detection and analysis of changes in the chemical composition and microstructural changes; it has proven to be an ideal model material for this study. AISI 4340 steel was selected as the second material since it is used in several erosion/corrosion environments. Additional reasons for restricting the study to these two materials were to facilitate development of analytical techniques and determine the reproducibility of the laser system.

Emphasis was placed on carburizing and nitriding reactions, particularly since these reactions are suspected to be dominant in many erosion/corrosion environments. Gases that have been used in the pressure chamber include air, argon, methane-and-argon mixtures, carbon monoxide, nitrogen, and ammonia. Some information also was obtained on oxidizing reactions, since impurities resulted in slight oxidation during the inert gas experiments. An important aspect of these experiments was to investigate the effect of gas pressure on the extent of the reaction.

To improve the resistance of critical components exposed to erosion/corrosion conditions, an obvious and frequently applied technique is to coat the component with material that is more resistant to erosion/corrosion than the unprotected substrate. Therefore, tests were performed on AISI 4340 specimens that had been coated with tungsten. The results demonstrate that the laser system can produce useful data on the performance of candidate coating materials for erosion/corrosion applications.

Experimental Procedures

Target Materials

The purity of the iron available for this study was nominally 99.96%. The chemical composition is listed in Table 1. The carbon, nitrogen, and oxygen contents of 18.0, 1.0, and 33.0 ppm, respectively, were sufficiently low to facilitate the detection of small changes in the concentrations of these elements induced by laser pulsing.

The composition of the AISI 4340 steel is listed in Table 2. The material was in the quenched and tempered condition, which resulted in a uniform tempered martensitic microstructure.

Gases

Carbon monoxide is a frequent combustion product that forms in erosion/corrosion environments. The dissociation of carbon monoxide in a reducing atmosphere can cause carburization (Appendix 1), and carbon monoxide was an obvious choice for a carburizing gas. However, the dissociation of carbon monoxide is known to require catalysis at moderately low temperatures,[2] particularly for carburization of iron, and this suggested that dissocation of carbon monoxide may be difficult within the short time frame of a laser pulse. To insure that carburization did occur, methane was selected as a second carburizing gas. Methane is used in industrial carburizing processes, and it does not require catalysis for dissociation.[2] Early experiments revealed that methane decomposed during laser pulsing at relatively low gas pressures to form soot on the internal surfaces of the pressure chamber. This caused absorption of the laser beam and impaired reproducibility. Consequently, dilute mixtures of methane in argon were used.

The dissociation of nitrogen in the laser system was subject to similar uncertainties, and this led to the selection of both ammonia and nitrogen in attempts to sustain nitriding reactions in the laser pressure-chamber system. Ammonia tended to condense on the walls of the pressure chamber at pressures above 100 psi, so the ammonia experiments were limited to this pressure. Purified argon and air also were included in the program

Table 1. Chemical analysis of high-purity iron.

Element	Amount (ppm – atom fraction)
C	18.0
O	33.0
H	< 1.00
N	< 1.00
Al	60.0
Na	ND[b]
Mg	< 10.0
P	ND
S	40.0
Cl	ND
K	ND
Ca	< 10.0
Ti	< 10.0
Fe	Major
Cu	30.0
Si	50.0
Cr	30.0
Ni	< 10.0
Zn	ND
Ga	ND
Zr	ND
Nb	ND
Mo	30.0
Pd	ND
Ag	<5.0
In	ND
Sn	<30.0
Sb	ND
Ta	ND
W	ND
Pt	ND
Au	ND
Pb	<30.0

[a] Analytical techniques: emission spectroscopy, vacuum fusion (gases), and conductometric (carbon).

[b] Not detected.

to check the operation of the system and to provide baseline data for the carburizing and nitriding reactions. Thus, the following gases were used for this study:

Argon
10% methane in argon*
Carbon monoxide
Ammonia
Nitrogen
Air

Table 2. Chemical analysis of 4340 steel.

Element	Amount (wt%)
C	0.42
Mn	0.75
P	0.13
S	0.011
Si	0.25
Cr	0.77
Ni	1.70
Mo	0.26
Cu	0.06
Al	0.03
Sn	0.01

All gases except air were obtained from commercial gas cylinders.

An important consideration in these experiments is that impurities can significantly modify surface reactions. Possible sources of impurities are contamination in the bottled gas, residual air and water vapor not completely purged from the pressure chamber, and contamination adsorbed onto the specimen and the internal surfaces of the pressure chamber. Initial efforts were made to purify the gases, but slight amounts of oxidation appeared in most of the experiments, particularly those conducted with argon. This proved to be fortuitous, however, because it demonstrated the sensitivity of specimen response to the environment and provided additional information on oxidation reactions.

Specimen Preparation

The iron and AISI 4340 specimens were 1/2-in.-diameter disks approximately 1/8-in. thick. The surface of each specimen that was to be exposed to the laser beam was metallographically polished. This enhanced detection of surface damage and also provided a more uniform surface for SIMS analysis. For the energy-absorption computations, each specimen was weighed to within 0.5 mg, and the specimen thickness was measured with a micrometer. A Chromel-Constantan (Type E) thermocouple was spot-welded to the center of the back surface of each specimen. The thermocouple wire diameter was 0.005 in. Experiments were performed on the use of piezoelectric crystals to generate frequency-response and pressure-response data, but time did not permit the development of this technique for routine use.

---

* Hereafter denoted as methane/argon.

Laser System

The laser available for this study was a two-stage neodymium-glass laser capable of generating a pulse of up to 100 J in the normal mode; the pulse duration was 600 μs, and the beam diameter was 19 mm. A schematic diagram of the laser system is shown in Fig. 1, and an engineering safety evaluation of the pressure chamber is detailed in Appendix 2. The beam was directed through two glass beam splitters. A small portion of the beam was diverted into a calorimeter by one beam splitter to monitor beam energy and into a photodiode by the other beam splitter to provide a trigger pulse for the recording oscilloscope. As shown in Fig. 1, the main beam then passed through a converging lens and an aperture (not indicated in the figure), entered the pressure chamber through the entrance window, and was deposited on the specimen. The lens focused the beam to a diameter of 3.2 mm (1/8 in.) on the surface of the specimen. The pressure-chamber system was enclosed in a vented hood to minimize toxicity and combustion hazards in the event that a window failed.

Sapphire was chosen for the window material. It has a transmissivity of about 0.83 at a wavelength of 1.06 μm, the operational wavelength of the neodynium glass laser. In addition, sapphire cracks slowly; it does not have a tendency to fail catastrophically as quartz and other transparent materials do. Unfortunately, the quality of the sapphire windows was not consistent, and impingement of the laser beam on impurities tended to initiate pitting and cracking. This, in turn, reduced the transmitted intensity of the beam. Therefore several precautions were taken to protect the window. In high-pressure experiments, the lens was positioned inside the pressure chamber. This permitted a larger-diameter beam to be passed through the window and reduced the

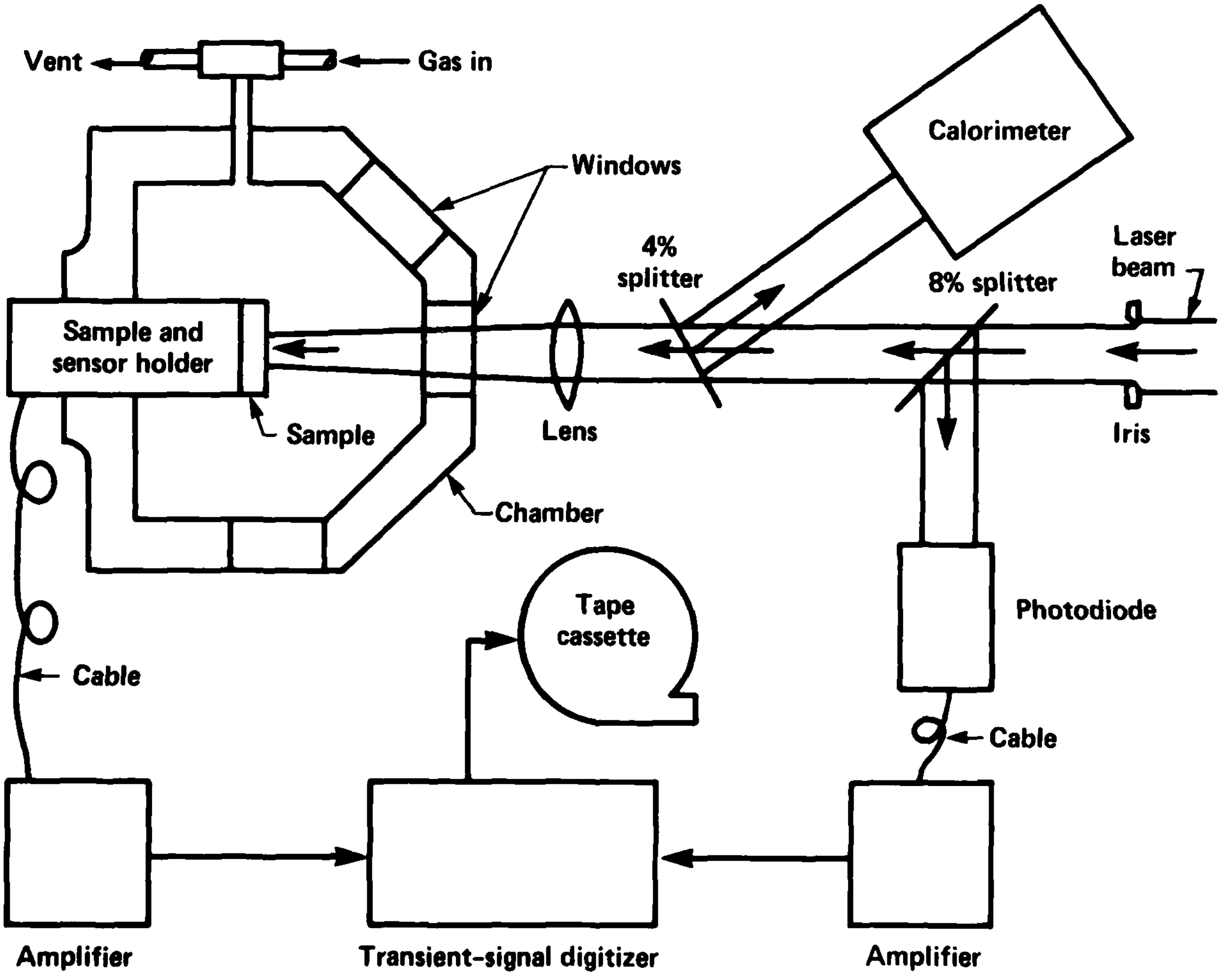

Fig. 1. Schematic diagram of the laser system.

energy density of the beam in the sapphire window. This also reduced the decomposition of the carburizing gases at high pressures that caused deposition of soot films both on the specimen and on the internal optical surfaces of the pressure chamber. A cover glass placed between the specimen and the internal lens eliminated redeposition of metallic elements from the specimen onto the back surface of the lens. A new cover glass was inserted for each run. Further protection of the lens and window was obtained by tilting the specimen 4 degrees off axis. This shifted the reflected beam and substantially reduced damage to the back surface of the sapphire window.

Intensity fluctuations in the energy profile of the laser beam are inherent in the laser system that was available for this study. Attempts were made in the early stages of the program to improve the uniformity and reproducibility of specimen response to the laser beam, but the improvements were marginal. The best and most consistent beam uniformity was obtained by focusing the beam to a small diameter. The smallest beam diameter considered to be acceptable for SIMS and metallographic analysis was 3.2 mm. Alignment of the laser system was critical and was checked repeatedly during the program.

To conduct an experiment, we inserted a specimen into the specimen holder and clamped it with three point-contact set screws. The thermocouple leads from the back of the specimen were attached to a feed-through connector in the specimen holder assembly, and the assembly was inserted into the rear port of the pressure chamber and tightened to seal the system. The exterior feed-through wires were connected in differential mode to a dc amplifier. The amplifier output was connected to a digital oscilloscope. A cable was connected from the capacitor bank of the laser power supply to the oscilloscope to act as a trigger. The appropriate gas bottle was connected to the pressure-vessel inlet manifold, and the chamber was pressurized and emptied several times to minimize air contamination. The gas pressure was controlled with a regulator and montiored with a pressure transducer. Once the proper pressure was achieved, the oscilloscope was armed, the capacitor banks were charged, and the laser was fired.

The time–temperature curve obtained from the back-surface thermocouple output was collected by a digital oscilloscope and stored on a soft magnetic disk. The energy output of the laser was measured by the calibrated calorimeter, which was sensitive to the 1.06-μm wavelength of the neodymium glass laser. The energy absorbed by the sample and the absorption coefficient were calculated from from the sample's back-surface temperature rise.

SIMS Analysis

Surface reaction products that form within the short time frame of a laser pulse were not expected to be extensive, and the detection and analysis of these products were suspected to require highly sensitive surface analytical techniques. Both Auger electron spectroscopy (AES) and secondary ion mass spectroscopy (SIMS) were considered. AES is extremely sensitive for the analysis of thin surface films, and *in situ* ion milling in an Auger instrument can be used to determine the relative concentrations of elements as a function of depth below the surface. With appropriate standards, these depth profiles can permit quantitative analyses of the amounts of reactants introduced into a substrate. SIMS involves the continuous removal of material from a surface with an ion beam and, therefore, is not as ideal for surface analysis as AES. However, the rate of material removal in SIMS is much greater than in AES, and SIMS is more ideal for depth-profile analysis than AES. In addition, SIMS is much more sensitive than AES for the analysis of low concentrations of most elements. Since the depth of penetration of low concentrations of reactive species was of more interest than reaction products formed on the surface, chemical composition changes were monitored by SIMS.

The SIMS analyses for this portion of the study were performed with CAMECA IMS-3f instruments. Initially, both Cs^+ and O_2^+ primary ion beams were used, but the Cs^+ ion beam was found to be most suitable for the analysis of interstitial elements. The Cs^+ ion beam yields better sensitivity for elements with higher electron affinities, and it is used primarily for electropositive elements; these include hydrogen, carbon, oxygen, and silicon. The O_2^+ ion beam yields better sensitivity for elements with low ionization potentials, and it is used for the electronegative or metallic elements. Unfortunately, nitrogen has both a very low electron affinity and a high ionization potential and is one of the more difficult elements to analyze with SIMS. Depth profiles obtained for ^{14}N using a primary O_2^+ beam appeared to be insensitive to the nitrogen concentration. However, useful information on nitrogen concentration gradients has been generated by analyzing for molecular combinations of nitrogen with carbon and iron using a primary Cs^+ beam. Thus, mass isotopes 26 (^{12}C + ^{14}N) and 70 (^{56}Fe + ^{14}N) were used to monitor changes in the nitrogen concentration. Some precaution has to be used, however, because mass isotopes 26 and 70 are subject to interferences with other molecular combinations (e.g., ^{10}B + ^{16}O, $^{12}C_2$ + $^{1}H_2$, ^{54}Fe + ^{16}O, and ^{58}Fe + ^{12}C).

Problems associated with the use of SIMS for generating depth concentration profiles have been reviewed by Zinner,[3] and many of these problems were encountered in this study. One of the problems was that high sputtering rates were required to penetrate the layer of material affected by the laser beam in reasonable times. The sputtering rates were on the order of 0.05 μm/s. Although the required penetration was achieved, the surfaces of the craters generated by the high sputtering rates were quite rough. This compromised the accuracy of the depth calibration, but most profiles corresponded remarkably well to reaction depth measurements obtained from the metallographic cross sections. Additional problems were encountered with the topography of the laser-pulsed surfaces, redeposition of sputtered material, and contamination. When melting occurred during laser pulsing, the surface became rough and uneven and occasionally affected the relative intensities of some of the profiles. This condition usually was obvious and could be corrected at least partially with a normalization technique. Redeposition of sputtered material that collects on the aperture system of the instrument also can alter the shape of the profile and falsely increase the apparent depth of reaction indicated by the profile. This problem is somewhat more difficult to recognize. Both of these problems can be circumvented to some extent by conducting step-scan profiles on metallographic cross sections through the affected surface layer, but the combination of edge effects and the limited depth of the layers precluded this. In addition, residual contamination can be caused by gases absorbed onto the surface of the specimen and residual gases still present during the recovery period of the ultrahigh-vacuum system after a specimen change. This tends to produce slightly higher profiles of carbon, oxygen, and hydrogen, particularly in the initial portions of the profiles. Once this problem was recognized, it was minimized by allowing sufficient time for the vacuum system to recover.

Metallography

Upon completion of the SIMS analyses, SEM examinations were conducted on the surfaces of the exposed areas to determine whether the dominant damage mechanism was deformation, recrystallization, or melting. Optical metallographic examinations were then conducted on polished and etched cross sections taken normal to the exposed surfaces to generate information on the depth of microstructural changes induced by laser pulsing.

To prepare the specimens for metallographic examinations, we sectioned them through the centers of the laser-impacted regions. A low-speed diamond cut-off wheel was used to minimize cutting damage. The sections were cut normal to the laser-impacted surfaces so that the structural changes from the surface into the bulk could be examined. The specimens were mounted and ground on conventional silicon carbide papers, polished sequentially with 1-μm and then 1/4-μm diamond compounds on a vibratory polisher, and final-polished on a conventional polishing wheel with aluminum oxide. A 2% Nital etch was used to reveal the structure. Many of the specimens were over-etched to reveal the structure of the as-quenched martensite.

Coating Experiments

AISI 4340 steel specimens were plated with tungsten using chemical vapor deposition (CVD) for the reduction of WF_6 with hydrogen. The technique is described in greater detail in the previous publication.[1] Since tungsten does not adhere to iron in the presence of the fluoride,[1] an intermediate coating of electroplated nickel was used. Nickel thicknesses of 2, 6, and 10 μm were applied in an attempt to duplicate the previous results, which indicated that the sensitivity of tungsten to cracking was affected by the thickness of the nickel. A nominal 250-μm CVD tungsten deposit was applied over the nickel. The surfaces of the tungsten deposits were ground through 600-grit silicon carbide paper to provide a uniform surface condition for laser pulsing.

Results for Iron and AISI 4340 Steel Specimens

The iron and AISI 4340 steel specimens exposed for these experiments are listed in Table 3. Included in the table are the average beam energy for the total number of pulses applied to the specimen and the average beam energy absorbed by the specimen.

Visual Observations

Optical macrographs of the laser-pulsed regions are presented in Figs. 2 through 7. Pure iron specimens are shown in Figs. 2 through 6, and AISI 4340 steel specimens are shown in Fig. 7.

Pure Iron Specimens

Figure 2 shows the difference in surface damage on pure iron specimens that were laser-pulsed with different beam energies in argon at 150 psi. Figure 2a is from Iron A,* which was pulsed with a 10-J beam, and Fig. 2b is from Iron B, which was pulsed with a 40-J beam. Inhomogeneity of the laser beam is evident in Fig. 2a, but specimen response became more uniform as the beam energy increased. The energy at the center of the beam was sufficiently high to cause localized melting.

---

* Specimen identities are presented in Table 3.

Table 3. Experiments conducted in the laser pressure-chamber system on high-purity iron and AISI 4340 steel.

Sample	Gas	Pressure (psi)	No. pulses	Average energy (J)	Energy absorbed (%)
Iron 40	10% CH_4/Ar	150	10	11.2	29.1
Iron 43	10% CH_4/Ar	150	10	39.6	31.9
Iron 50	10% CH_4/Ar	150	1	37.8	33.3
Iron 51	10% CH_4/Ar	150	2	38.8	33.0
Iron 52	10% CH_4/Ar	150	5	39.4	31.9
Iron 53	10% CH_4/Ar	150	10	42.1	30.4
Iron 54	10% CH_4/Ar	150	25	43.8	30.4
Iron 55	10% CH_4/Ar	150	50	43.5	28.7
Iron 58	CO 99.99%	150	10	11.8	27.4
Iron 59	CO 99.99%	150	10	43.4	29.4
Iron 60	N_2 99.9995%	150	10	12.1	29.5
Iron 61	N_2 99.9995%	150	10	44.1	30.1
Iron 62	NH_3 99.998%	100	10	12.2	–
Iron 63	NH_3 99.998%	100	10	43.4	29.2
Iron 68	Air	15	10	11.0	a
Iron 69	Air	15	10	39.6	b
Iron 70	10% CH_4/Ar	15	10		
Iron A	Ar 99.999%	150	10	11.1	29.2
Iron B	Ar 99.999%	150	10	40.1	31.4
4340 A	Ar 99.999%	150	10	12.2	28.0
4340 B	Ar 99.999%	150	10	43.1	31.0
4340 40	10% CH_4/Ar	150	10	12.1	28.7
4340 41	10% CH_4/Ar	150	10	23.6	30.5
4340 42	10% CH_4/Ar	150	10	32.5	31.9
4340 43	10% CH_4/Ar	150	10	42.6	30.7
4340 50	10% CH_4/Ar	150	1	42.0	30.8
4340 51	10% CH_4/Ar	150	2	41.8	31.6
4340 52	10% CH_4/Ar	150	5	42.7	31.3

[a] The energy absorbed varied from 32% on the first pulse to 54% on the tenth pulse.
[b] The energy absorbed varied from 34% on the first pulse to 43% on the tenth pulse.

(a) Iron A, 10 pulses at 10 J. **(b) Iron B, 10 pulses at 40 J.**

Fig. 2. Laser-affected regions on the surfaces of pure iron specimens laser-pulsed in argon at 150 psi (10×).

Some of the small spots outside of the central melted region were caused by preferential response of inclusions. Slight discoloration was visible around the edges of the laser-impacted region. This probably was a thin reaction film caused by contamination of residual air or water vapor. Figure 2b shows the surface roughness resulting from the increased beam energy. A crater formed at the center of the laser-impacted region where the beam energy density was sufficiently high to cause surface melting.

Figure 3 compares the laser-affected regions of pure iron specimens which received different numbers of pulses in 10% methane/argon at 150 psi. The energy of the laser beam was 40 J for these experiments. Figure 3a is from Iron 50, which received 1 pulse, Fig. 3b is from Iron 51, which received 2 pulses, Fig. 3c is from Iron 52, which received 5 pulses, and Fig. 3d is from Iron 55, which received 50 pulses. These figures show the increase in damage that accumulated as the number of pulses increased, particularly around the periphery of the region where the energy density of the beam was lower. They also show that the first few pulses caused a slight increase in the depth of the crater that formed in the melted region, but then the crater depth remained essentially constant. The dark spots at two positions in the melted region of Fig. 3d and the single dark spot outside of the laser-affected region are craters generated by the primary ion beam of the SIMS instrument. As in the argon experiments, some evidence of film formation was evident around the edges of the laser-affected regions, and the surface darkened as the number of shots increased.

Pure iron specimens that were laser-pulsed in 10% methane/argon and carbon monoxide are compared in Fig. 4a from Iron 53 pulsed in 10% methane/argon and in Fig. 4b from Iron 59 pulsed in carbon monoxide. Both specimens received 10 pulses with a 40-J beam. The laser-affected region of Iron 59 in Fig. 4b is much darker than that of Iron 53 in Fig. 4a. As will be shown in the results from the SIMS analyses, this could be related to a significant increase in the subsurface oxygen concentration of the specimen pulsed in carbon monoxide. Again, the large dark spots in these figures are the positions at which SIMS analyses were made.

Specimens laser-pulsed in nitrogen and ammonia are shown in Figs. 5a and 5b, respectively. Both specimens received 10 pulses with a 40-J beam. Iron 61 in Fig. 5a was pulsed at 150 psi in nitrogen. Because of the condensation problem of ammonia at high pressures, Iron 63 was pulsed at only 100 psi in ammonia. The morphology of both regions appeared to be very similar, but Iron 61 (pulsed in nitrogen) appeared to have more damage around the periphery of the laser-affected region than Iron 63 (pulsed in ammonia). Positions of SIMS analyses also are evident in these figures.

(a) Iron 50, 1 pulse.

(b) Iron 51, 2 pulses.

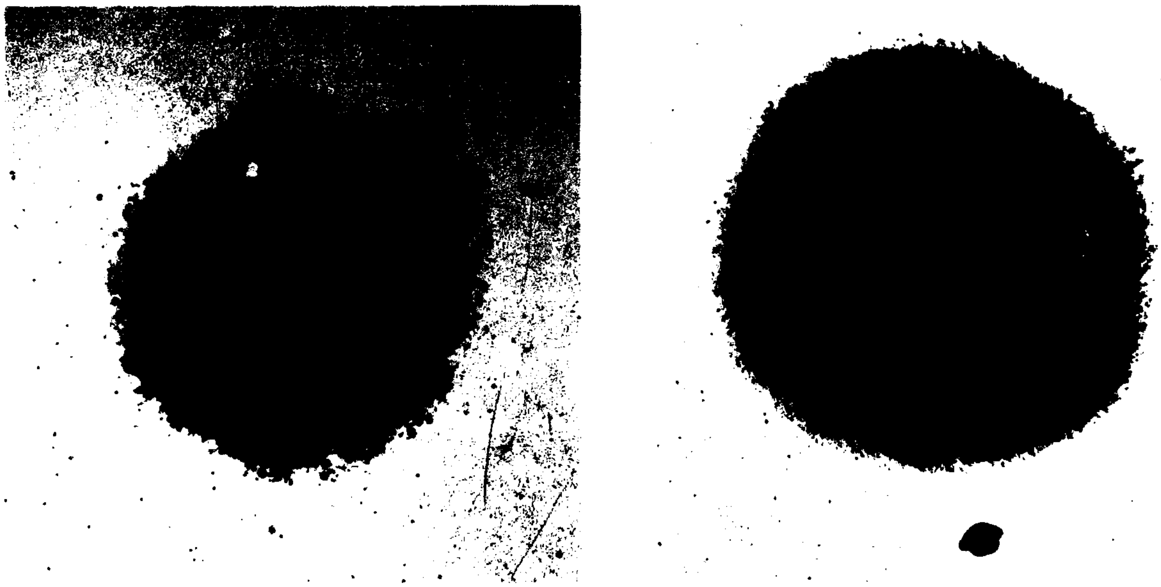

(c) Iron 52, 5 pulses.

(d) Iron 55, 50 pulses.

Fig. 3. Laser-affected regions on pure iron specimens pulsed with a 40-J beam in 10% methane/argon at 150 psi (10×).

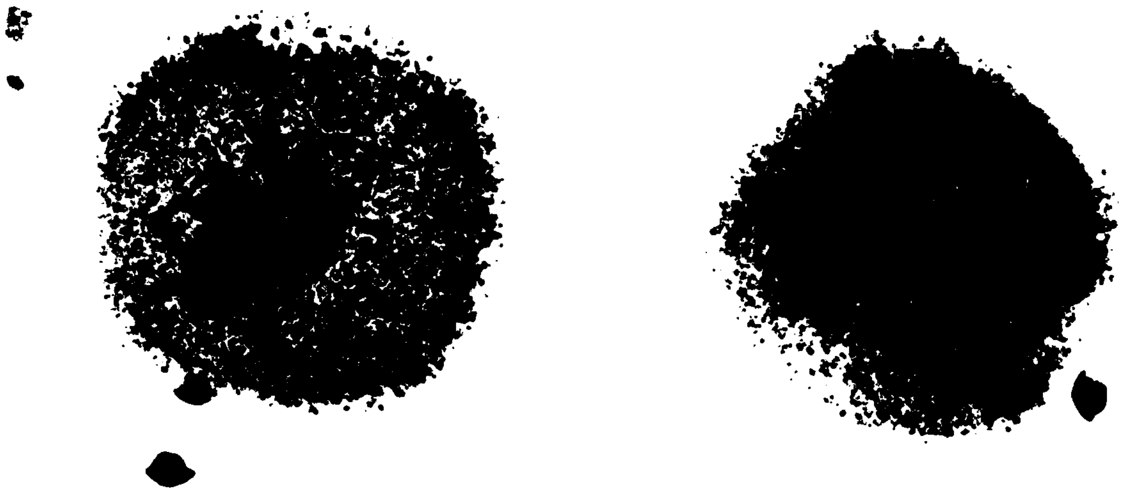

(a) Iron 53 pulsed in 10% methane/argon. (b) Iron 59 pulsed in carbon monoxide.

Fig. 4. Comparison of the laser-affected regions on pure iron pulsed with a 40-J beam in 10% methane/argon and carbon monoxide at 150 psi for 10 pulses (10×).

Specimens that received 10 pulses in air at 15 psi are shown in Fig. 6. Figure 6a is from Iron 68, which was pulsed with a 10-J beam, and Fig. 6b is from Iron 69, which was pulsed with a 40-J beam. The heavy oxide film that formed on these specimens is evident in the figures. Reference to the energy absorbed in Table 3 shows that formation of the oxide films caused a substantial increase in energy coupling between the laser beam and the oxidized specimens as the film formed during the first few pulses. This was unique to specimens laser-pulsed in air.

When the laser-pulsed surfaces were examined at high magnification, the first regions to exhibit damage had wavy slip lines, indicating that plastic deformation had occurred. As the energy of the laser beam increased, the damaged structures that occurred, in sequence, were recrystallization of the cold-worked structure, recrystallization and martensite formation, and surface melting. Evidence of fine grains with a superimposed martensitic structure could be seen in the melted regions. These structures will be described in greater detail in the following sections.

AISI 4340 Steel Specimens

AISI 4340 steel specimens that were pulsed in argon and 10% methane/argon at 150 psi are shown in Fig. 7. Sample 4340 A in Fig. 7a received 10 pulses in argon with a 10-J beam, 4340 B in Fig. 7b received 10 pulses in argon with a 40-J beam, 4340 50 in Fig. 7c received 1 pulse in 10% methane/argon with a 40-J beam, and 4340 43 in Fig. 7d received 10 pulses in 10% methane/argon with a 40-J beam. The laser-affected regions appeared to be similar to those formed in the pure iron specimens. However, when the specimens were examined at high magnification, plastic deformation and recrystallization were not observed in the AISI 4340 specimens.

SIMS Analyses

Pure Iron Specimens

The laser-impacted specimens were analyzed with the Cs$^+$ primary ion beam for mass isotopes ^{1}H, ^{12}C, ^{16}O, ^{28}Si, ^{34}S, and ^{56}Fe. In addition, analyses were conducted for mass isotope ^{11}B in some of the specimens. The depth-concentration profiles were normalized to ^{56}Fe equivalence. This was an attempt to compensate for intensity drift caused by the depth of the SIMS craters formed by the primary beam, surface roughness caused by surface melting, and drift in the primary beam current. It was effected by arbitrarily plotting the ^{56}Fe data along a straight line at a fixed intensity level and appropriately adjusting the other intensity data by the relative amount required to shift

(a) Iron 61 pulsed in nitrogen at 150 psi. **(b) Iron 63 pulsed in ammonia at 100 psi.**

Fig. 5. Laser-affected regions on pure iron specimens that received 10 pulses in nitriding gases with a 40-J beam (10×).

(a) Iron 68 pulsed at 10 J. **(b) Iron 69 pulsed at 40 J.**

Fig. 6. Laser-affected regions on pure iron specimens that were pulsed 10 times in air at 15 psi with a 40-J beam (10×).

(a) 4340 A, 10 pulses in argon at 10 J.

(b) 4340 B, 10 pulses in argon at 40 J.

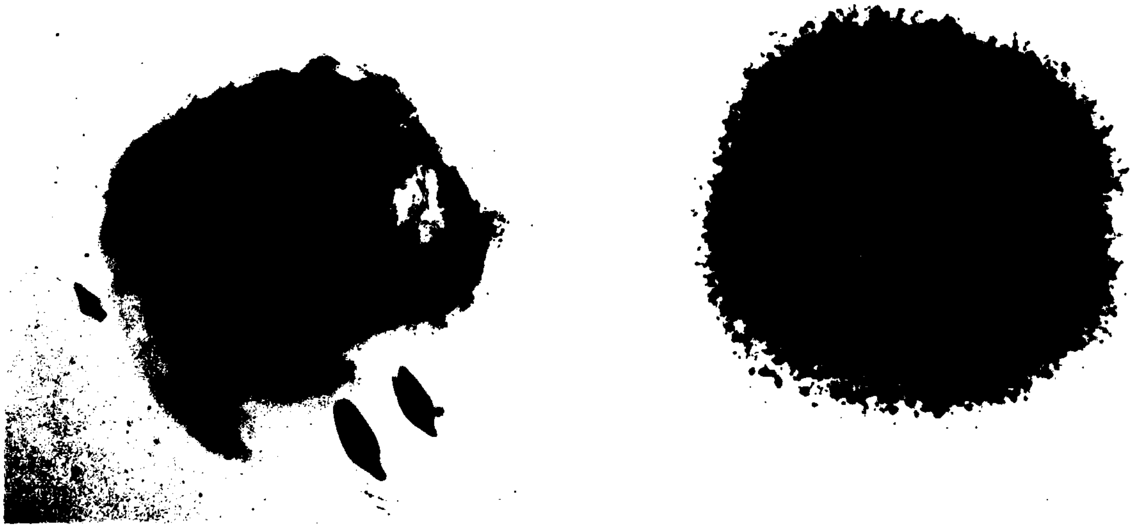

(c) 4340 50, 1 pulse in 10% methane/argon at 40 J.

(d) 4340 43, 10 pulses in 10% methane/argon at 40 J.

Fig. 7. Laser-affected regions on AISI 4340 steel specimens pulsed in argon and 10% methane/argon at 150 psi (10×).

the ^{56}Fe data. This is only an approximate correction, however, since the relative ion-extraction efficiencies also can be affected by concentration changes.

SIMS depth profiles were taken both outside of and within the laser-affected regions, so that compositional changes induced by the laser beam could be compared with the unexposed composition of the base material. As already mentioned, many of the areas analyzed by SIMS are visible in Figs. 2 through 7. Variations did occur in the relative intensities of the profiles from the base material of different specimens, and this appeared to reflect actual composition differences in the ppm range. However, contamination also could have contributed to this difference. As stated previously, the contamination probably was caused both by absorbed gases on the specimen and residual gases still present during the recovery period of the ultrahigh-vacuum system. This problem was not recognized in the initial phases of this study. Once it was recognized, it was minimized by allowing sufficient time for the vacuum system to recover.

Argon. The specimens laser-pulsed in argon at 150 psi demonstrated the effect of contamination in the pressure chamber and also provided an initial basis for comparison. Depth profiles from the unexposed and the laser-pulsed regions of Iron A, which was pulsed at 10 J, are shown in Figs. 8a and 8b, respectively; corresponding depth profiles from Iron B, which was pulsed at 40 J, are shown in Figs. 8c and 8d, respectively. Comparison of these depth profiles shows that laser-pulsing in argon significantly increased the oxygen concentration in the melted regions. The profiles indicate that the oxidation reaction occurred to a depth of about 20 μm in Iron A, which was pulsed with a 10-J beam, and to a depth of about 80 μm in Iron B, which was pulsed with a 40-J beam. Another significant reaction is demonstrated in these figures: whenever strong oxidation occurred in the absence of carburization, a noticeable but slight amount of decarburization occurred.

The rapid intensity fluctuations in the ^{12}C and ^{16}O profiles in Figs. 8a and 8c were much greater than the instrument noise level and were consistently observed in the base material of the pure iron. Corresponding intensity flucutations also occurred in the mass isotope 26 and 70 profiles. These fluctuations disappeared in the laser-pulsed regions whenever surface melting occurred. This is demonstrated by the smooth concentration profiles of carbon and oxygen in the laser-affected regions of Figs. 8b and 8d. Thus, these fluctuations appeared to be uniquely related to the cold-worked structure, and their absence provided an indication of the depth to which carbon and oxygen were homogeneously redistributed into solution, apparently by surface melting and rapid cooling. Further significance of these fluctuations is discussed in Appendix 3.

The profiles for mass isotopes 26 and 70 in Fig. 8b show increases near the surface nearly identical to the ^{16}O profile. In contrast, the profile for mass isotope 70 in Fig. 8d shows significantly less increase near the surface than the ^{16}O profile, while the mass isotope 26 profile actually shows a slight decrease that is very similar to the ^{12}C profile. This implies that nitrogen contamination occurred during the pulsing of Iron A but was absent during the pulsing of Iron B. Consequently, the major source of oxygen could have been air contamination in Iron A and residual water vapor in Iron B. This reflects some difficulty in purging the pressure chamber. The ^{1}H profiles in these specimens did not appear to be affected by laser-pulsing.

10% Methane/Argon. Depth profiles from specimens laser-pulsed in 10% methane/argon at 150 psi with a nominal beam energy of 40 J are shown in Fig. 9. Figure 9a was obtained from Iron 50, which received only 1 pulse, Fig. 9b from Iron 52, which received 5 pulses, Fig. 9c from Iron 53, which received 10 pulses, and Fig 9d from Iron 55, which received 50 pulses. These figures demonstrate that significant increases did occur in the carbon content as the number of pulses increased, although the exact quantitative amounts remain to be determined because of the lack of standards. Comparison with depth profiles from the AISI 4340 specimens indicated that the maximum carbon level reached in these figures was approximately 0.40%. The flat ^{12}C profile projecting from the surface of Iron 55 in Fig. 9d could indicate that saturation occurred. If this is true, the resultant carbon content may correspond to a quasi-equilibrium value for these specific conditions.

The oxygen content also increased slightly in Figs. 9a through 9d as the number of pulses increased. This corresponds with the increased darkening of the laser-pulsed surfaces shown in Figs. 3a through 3d. As discussed in the argon experiments, this is suspected to be caused by trace amounts of water vapor and/or air in the pressure-chamber system. Although the mass isotope 70 profile had not been entered into the program at the time that Iron 53 and Iron 55 were analyzed, the profiles for mass isotopes 26 and 70

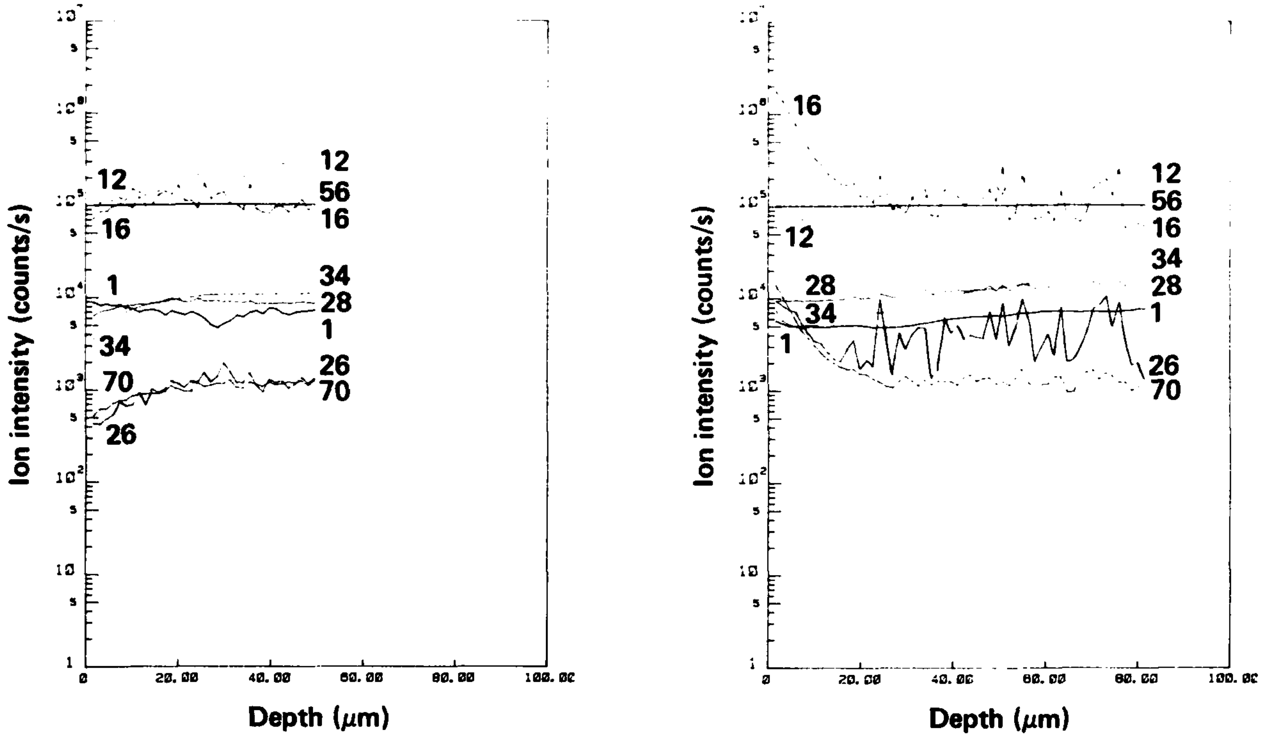

(a) Iron A, unexposed area.

(b) Iron A, 10 pulses at 10 J.

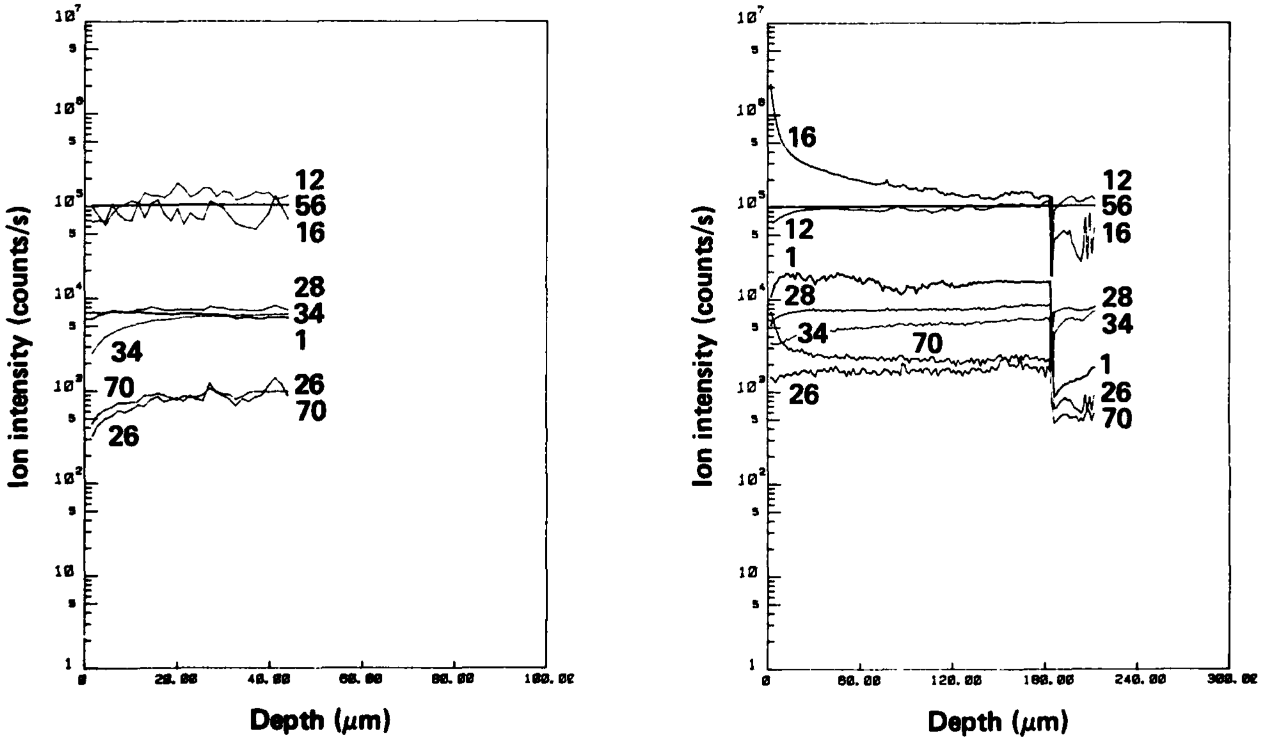

(c) Iron B, unexposed area.

(d) Iron B, 10 pulses at 40 J.

Fig. 8. SIMS depth profiles from pure iron specimens laser-pulsed in argon at 150 psi.

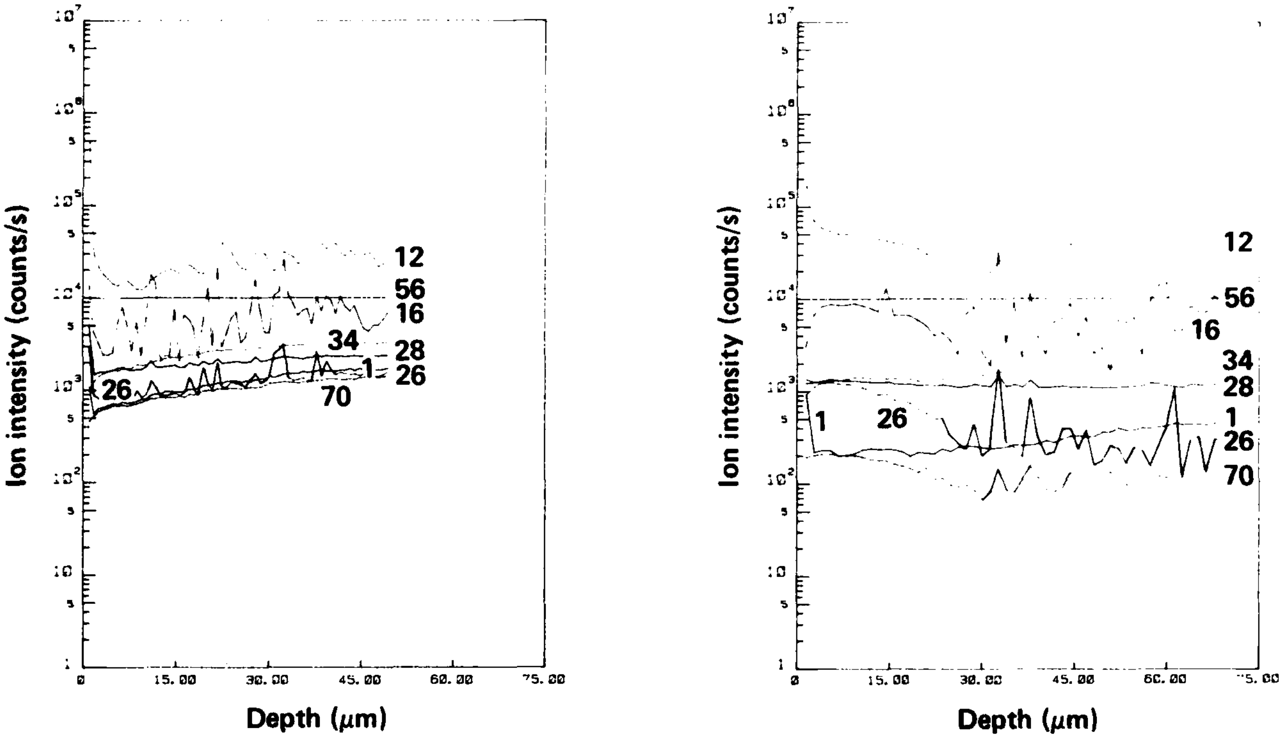

(a) Iron 50, 1 pulse.

(b) Iron 52, 5 pulses.

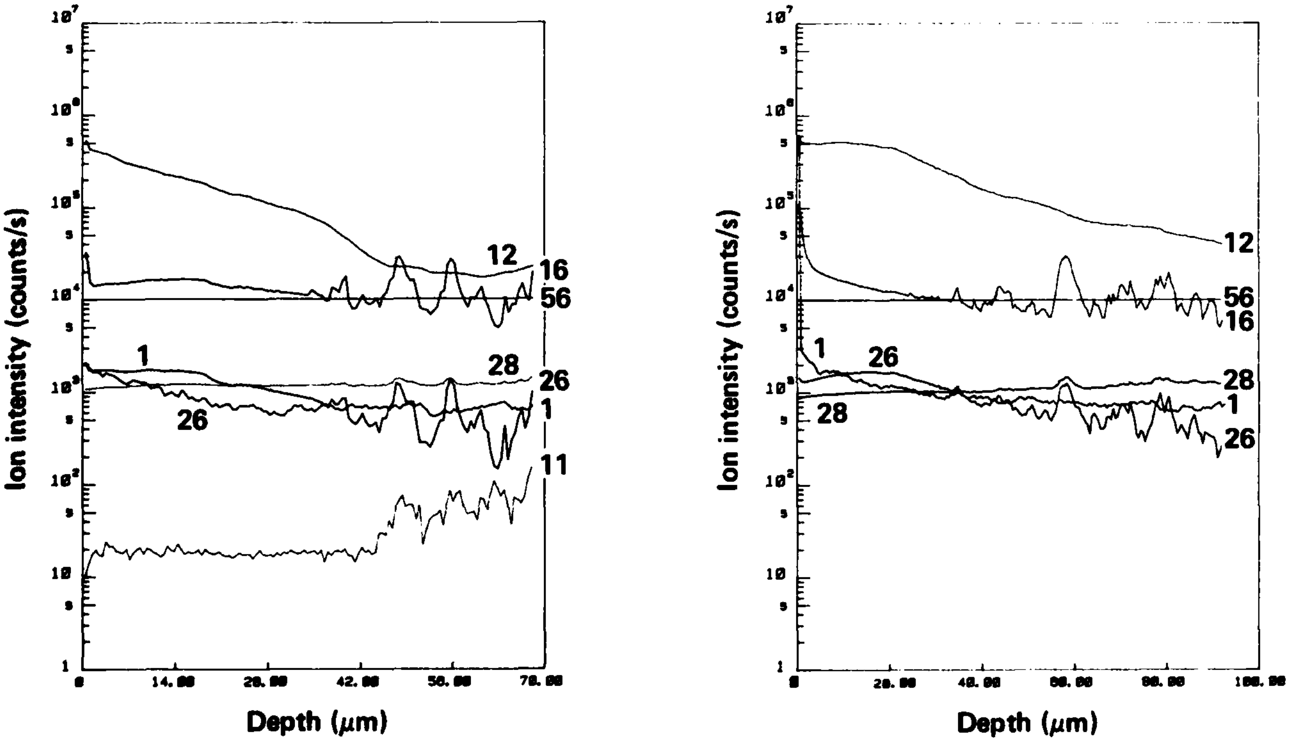

(c) Iron 53, 10 pulses.

(d) Iron 55, 50 pulses.

Fig. 9. SIMS depth profiles from pure iron specimens laser-pulsed in 10% methane/argon at 150 psi with a 40-J beam.

in Figs. 9b through 9d show increases near the surfaces similar to both the ^{12}C and ^{16}O profiles. The ^{1}H profiles also appeared to increase slightly near the surfaces, but did not consistently correspond with the increase in the ^{16}O profiles. The actual increase in hydrogen contamination is not suspected to be significant.

Depth profiles obtained from pure iron specimens laser-pulsed at different gas pressures and beam energies in 10% methane/argon are compared in Fig. 10. Each specimen received 10 laser pulses. Figures 10a and 10b are from Iron 70 which was pulsed at 15 psi with a nominal beam energy of 40 J. Figure 10a is from the center of the pulsed region and indicates that the damaged region extended only a few micrometers in depth. Figure 10b is from the rim of the pulsed region and shows significant carbon pickup to a depth of about 20 μm. This strongly implies that the energy of the laser beam was sufficient to either soften or melt the surface material, and the pressure generated during the laser pulse extruded the metal from the center of the impacted region to form the rim. Similar laser-induced reactions have been discussed by Anthony and Cline.[4] This type of crater formation could be suggestive of an important erosion/corrosion mechanism involving the extrusion of softened or molten material by a pulse of high-pressure gas.

Depth profiles from specimens pulsed at 150 psi are shown in Figs. 10c and 10d. Figure 10c is from Iron 40, which was pulsed with a 10-J beam, and Fig. 10d is from Iron 43, which was pulsed with a 40-J beam. Comparison of the depth profiles in Fig. 10 demonstrates the systematic response that was obtained by varying gas pressure and beam energy. The depth of carbon penetration increased with increasing beam energy and with increasing pressure. In contrast, macroscopic observations indicated that the crater depth decreased with increasing pressure.

Iron 43 in Fig. 10d and Iron 53 in Fig. 9c are duplicate specimens. The depths of carbon penetration indicated in Figs. 9c and 10d are nearly identical. This demonstrates the reproducibility of the laser pressure-chamber system. The higher ^{12}C profile in Fig. 10d is suspected to be related to surface roughness and is not considered to be significant.

Carbon Monoxide. The results from laser-pulsing in carbon monoxide were somewhat unexpected and provide an interesting comparison of the carburization reactions in carbon monoxide and in 10% methane/argon. Iron 59 received 10 pulses in carbon monoxide at 150 psi with a beam energy of 40 J. The depth profile from this specimen is shown in Fig. 11. The significant increase in the oxygen concentration in comparison with that in specimens pulsed in 10% methane/argon is obvious in the figure, and the amount of carburization also is noticeably less. Figure 11 also shows an increase in the mass isotope 26 profile comparable to those in specimens pulsed in 10% methane/argon. This suggests that air contamination did not contribute to the increased oxygen concentration evident in Fig. 11. One further observation from Fig. 11 concerns the flatness of the ^{12}C and ^{16}O profiles progressing from the surface of Iron 59. This may indicate that saturation occurs at an earlier stage in carbon monoxide than in 10% methane/argon.

Nitriding. As already discussed, SIMS analyses of specimens laser-pulsed in nitriding environments were not unambiguous because of the difficulty in analyzing for nitrogen by SIMS. Depth profiles from Iron 61 and Iron 63 generated with a primary Cs^+ beam are shown in Figs. 12a and 12b, respectively. Iron 61 received 10 pulses in nitrogen at 150 psi with a nominal beam energy of 40 J, and Iron 63 received 10 pulses in ammonia at 100 psi also at 40 J. These profiles were generated in the early stages of the SIMS work, and mass isotope 70 was not profiled because of the interference between ^{56}Fe + ^{14}N and ^{54}Fe + ^{16}O.

The profile for mass isotope 26 in Fig. 12a shows a substantial increase near the surface. The profile for ^{16}O also shows an increase, but comparison with the profiles obtained for the specimens pulsed in argon in Figs. 8b and 8d indicate that the relative increase in the mass isotope 26 profile is much greater in Fig. 12a. This strongly indicates that the increase is related to nitrogen, particularly since the ^{12}C profile shows a slight decrease in the same region. The profiles indicate that the depth of nitrogen penetration was about 40 μm.

Problems associated with the condensation of the ammonia gas at pressures over 100 psi appear to be reflected in the depth profile from Iron 63 in Fig. 12b. The ^{16}O profile is anomalously high; this probably was caused by absorption of water vapor in the ammonia. The ^{1}H profile also increases substantially near the surface. This could be associated with the dissociation of ammonia into nitrogen and hydrogen (cf. nitriding reactions in Appendix 1). The profile for mass isotope 26 also increased near the surface, but not to the extent it did in the nitrogen experiment in Fig. 12a. The profiles indicate that nitrogen penetrated to a depth of 20 to 30 μm and hydrogen penetrated to

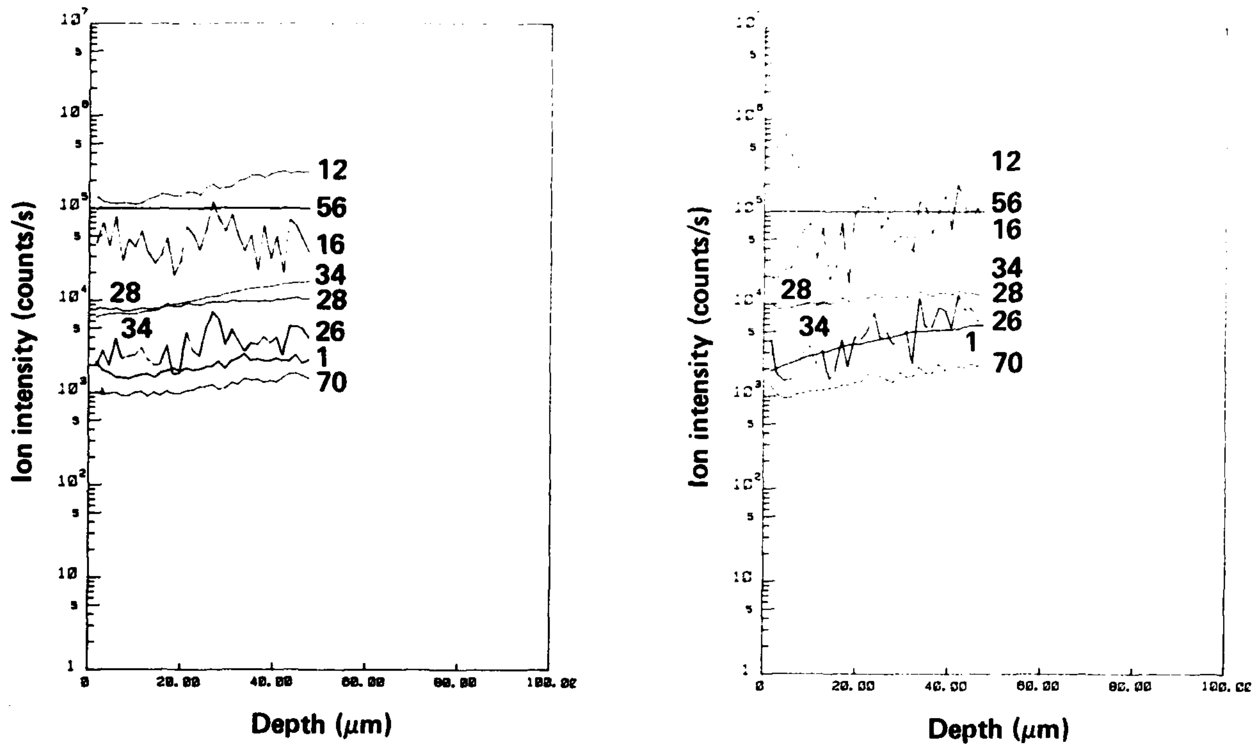

(a) Iron 70, 15 psi, 40 J, center of laser-pulsed region.

(b) Iron 70, 15 psi, 40 J, rim of laser-pulsed region.

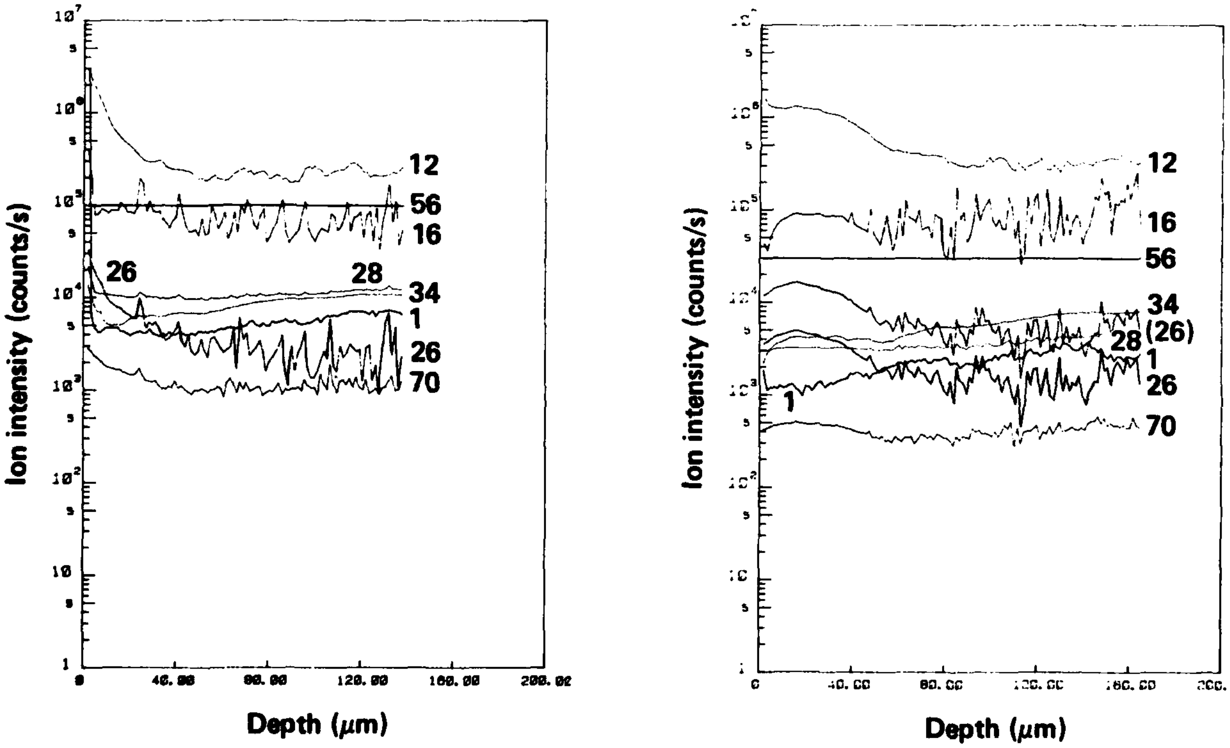

(c) Iron 40, 150 psi, 10 J.

(d) Iron 43, 150 psi, 40 J.

Fig. 10. SIMS depth profiles from pure iron specimens laser-pulsed in 10% methane/argon for 10 pulses at different pressures and beam energies.

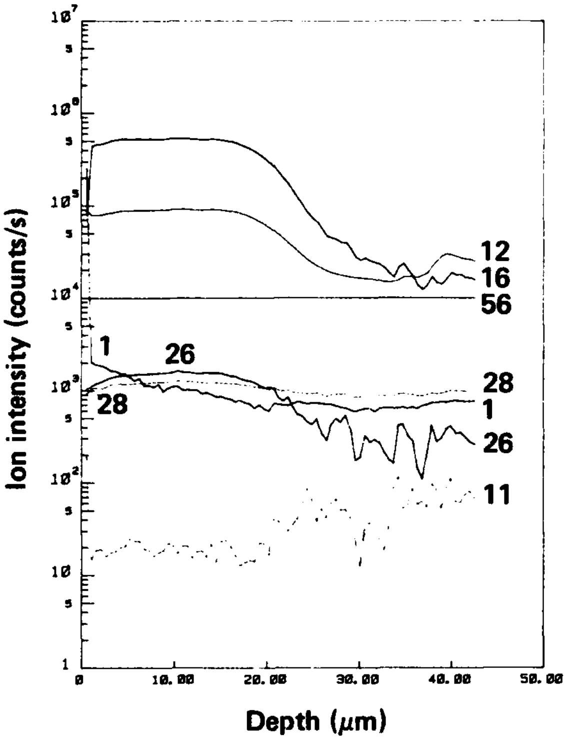

Fig. 11. SIMS depth profile from Iron 59 exposed for 10 pulses in carbon monoxide at 150 psi with a 40-J beam.

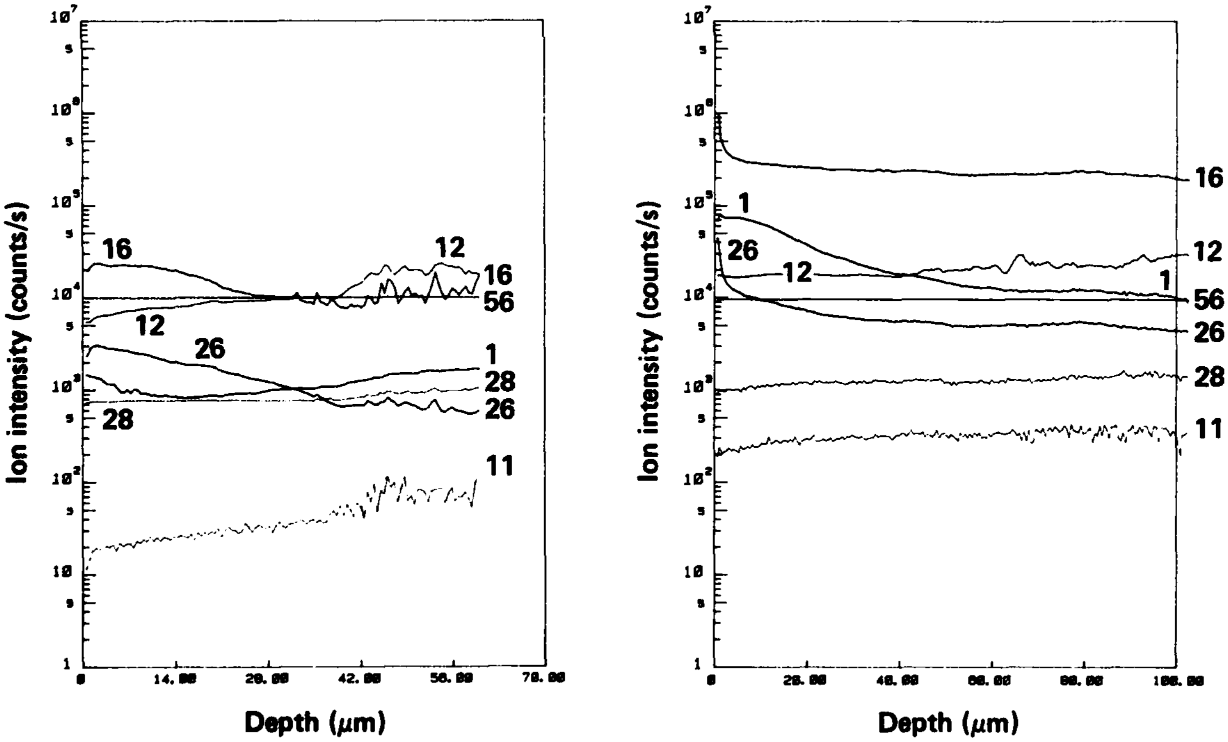

(a) Iron 61, nitrogen, 10 pulses, 150 psi, 40-J beam.

(b) Iron 63, ammonia, 10 pulses, 100 psi, 40-J beam.

Fig. 12. SIMS depth profiles in pure iron specimens laser-pulsed in nitriding gases.

a depth of about 60 μm. This is consistent with the higher diffusivity of hydrogen than nitrogen in iron.

AISI 4340 Steel Specimens

Depth profiles obtained from some of the AISI 4340 steel specimens are presented in Fig. 13. These specimens were tested at 150 psi with a nominal beam energy of 40 J. As in the previous depth profiles, the AISI 4340 profiles were normalized to ^{56}Fe equivalence. In addition to the mass isotopes analyzed in the pure iron specimens, depth profiles were obtained in the AISI 4340 steel specimens for ^{11}B and ^{35}Cl. Figures 13a and 13b were obtained from 4340 50, which received one pulse in 10% methane/argon. Figure 13a represents the composition of the unaffected base material outside of the laser-pulsed region. As listed in Table 2, the carbon content of this material was reported to be 0.42 wt%. This provides a calibration point for carbon. The calibration is tentative for the pure iron specimens, however, since the alloy content of AISI 4340 could modify the ion-extraction efficiency of carbon.

The depth profile from the center of the laser-pulsed region of 4340 50 is shown in Fig. 13b. The ^{12}C profile is slightly higher than in Fig. 13a, but this probably is related to surface roughness. A significant increase in carbon content did not occur in this specimen. Figure 13c is from the center of the laser-pulsed region in 4340 43, which received 10 pulses in 10% methane/argon. The ^{12}C profile increased slightly at the surface. Figure 13d shows the depth profile for 4340 B, which received 10 pulses in argon. The ^{12}C profile in this figure is slightly lower than the ^{12}C profile in Fig. 13a, but again not by a significant amount. The fact that laser-pulsing AISI 4340 steel in 10% methane/argon did not cause a significant increase in the carbon content indicates that the maximum carburization potential of 10% methane/argon is about or slightly below 0.40 wt% carbon for these experimental conditions.

The most obvious change in the depth profiles in Figs. 13b through 13d is the significant increase in the ^{16}O profiles near the surfaces. The large peaks occurring in the ^{16}O profiles probably are related to oxygen-bearing inclusions, which commonly occur in these steels. The large increases in the ^{1}H profiles near the surfaces in Figs. 13b and 13d are considered to indicate inadequate recovery of the instrument vacuum prior to initiating the profiles. This also may have contributed to the increases in the ^{16}O profiles in these figures. However, the ^{1}H profile in Fig. 13c is relatively flat, and this indicates that the increase in the oxygen concentration is significant. The mass isotope 26 profiles in Figs. 13b and 13c decreased near the surfaces. This also may be related to residual contamination in the vacuum system but cannot be explained at the present time. These problems reflect difficulties sometimes encountered in the interpretation of SIMS results.

Optical Metallography

Optical metallographic examinations were conducted both on the surfaces of the laser-pulsed specimens and on cross sections through the centers of the laser-pulsed regions. The surfaces of the specimens had been polished prior to laser-pulsing to facilitate the detection of laser-induced damage. Optical examination of these surfaces stimulated more detailed examinations with a scanning electron microscope, and details of the surface structural changes are presented in the next section on "Scanning Electron Microscopy." This section describes the subsurface microstructural changes that were revealed in metallographic examinations of polished and etched cross sections taken through the laser-damaged surface layers.

Pure Iron Specimens

The iron used for this study had a cold-worked structure. An example of the cold-worked structure is shown in Fig. 14. The bar apparently had been swaged or drawn, and the structure was heavily banded along the axis of the bar. This cold-worked structure provided a convenient reference structure that contrasted sharply with the microstructural changes induced by laser-pulsing. As already mentioned, the first damage threshold encountered was plastic deformation. This was manifest as wavy slip lines on the surface of the specimen, but it was not evident in the previously cold-worked structure in the metallographic cross sections. This damage mechanism was followed, in order, by recrystallization of the cold-worked structure, the formation of martensite, and surface melting. Surface melting generated crater formation and caused considerable surface roughness. As will be shown, the martensitic structure observed in the polished cross sections appeared to exhibit subtle changes that corresponded to the different gases that were used.

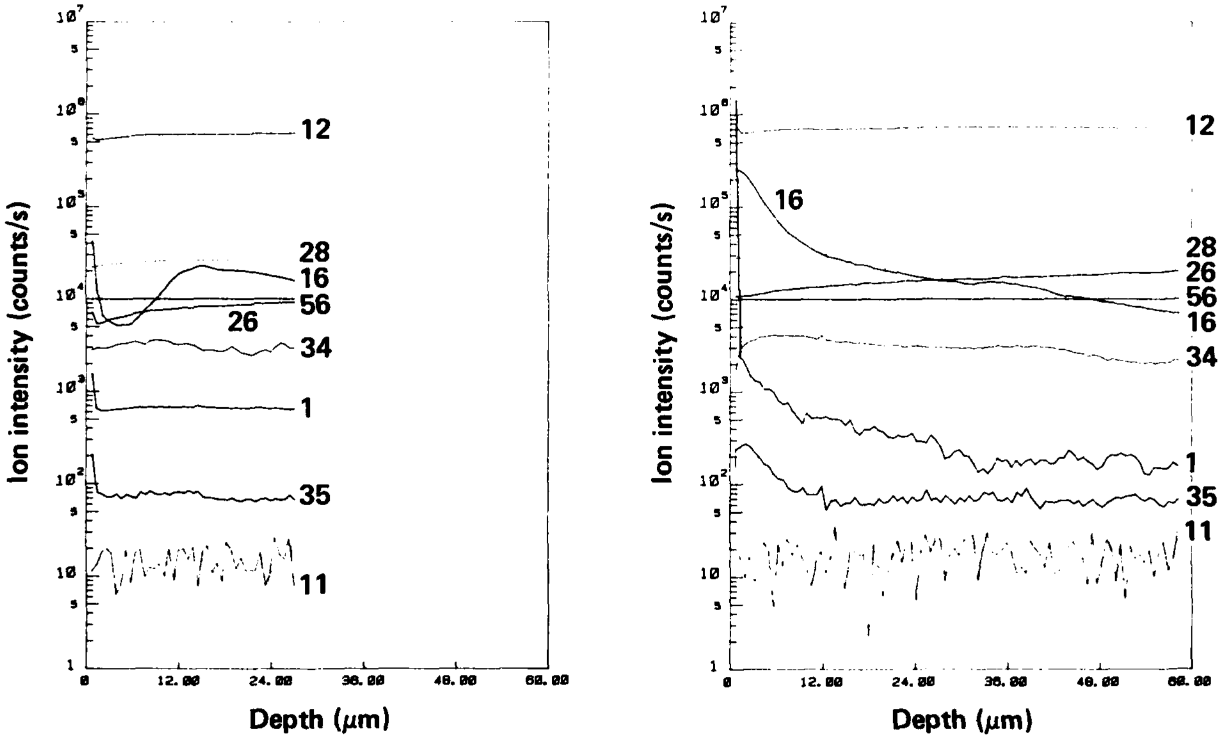

(a) 4340 50, unexposed region.

(b) 4340 50, 1 pulse in 10% methane/argon.

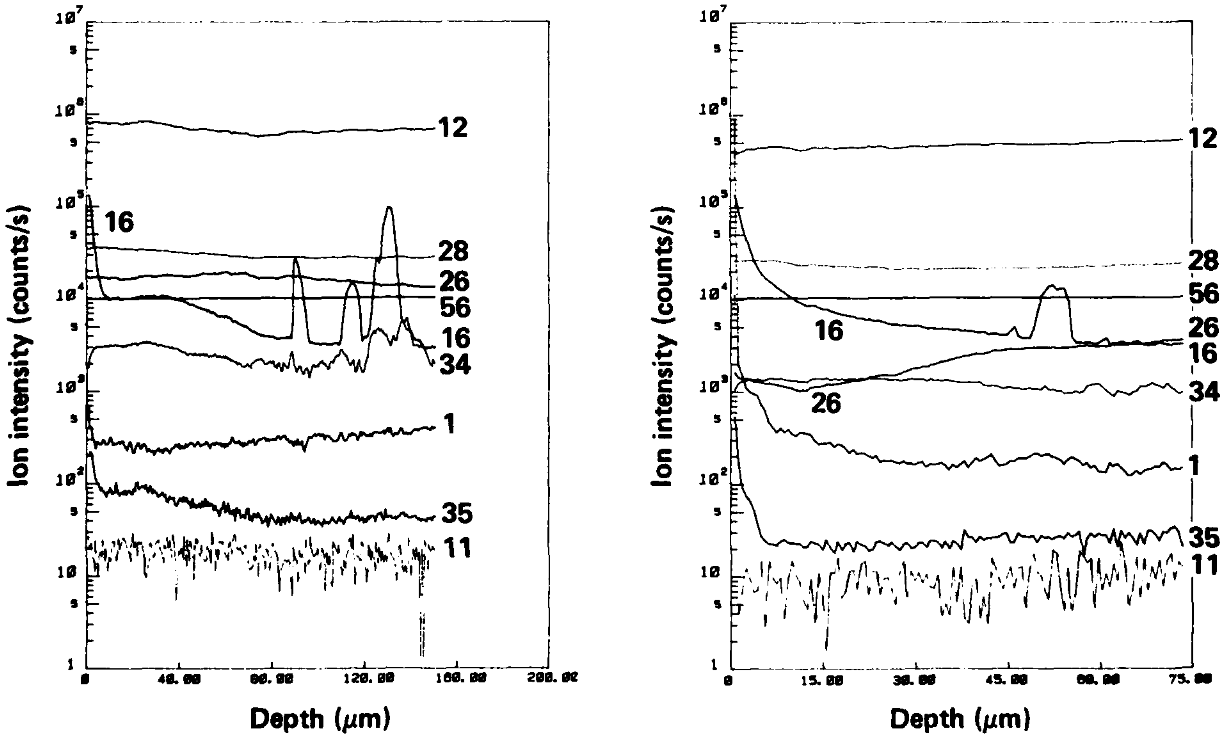

(c) 4340 43, 10 pulses in 10% methane/argon.

(d) 4340 B, 10 pulses in argon.

Fig. 13. SIMS depth profiles from AISI 4340 steel specimens laser-pulsed at 150 psi with a 40-J beam.

Argon. Examples of microstructural changes induced by laser-pulsing in argon at 150 psi are shown in Figs. 15a and 15b. Figure 15a is from Iron A, which received 10 pulses at a nominal energy of 10 J, and Fig. 15b is from Iron B, which received 10 pulses at a nominal energy of 40 J. The corresponding SIMS depth profiles for these specimens are shown in Figs. 8b and 8d, respectively. The surface structure in Fig. 15a appears to be predominantly recrystallized, with some indication of martensite. The depth of melting was not revealed in the metallographic inspections of these specimens. The depth of the laser-affected structure in Fig. 15a is approximately 20 μm; this is nearly identical to the depth of penetration of oxygen indicated in the SIMS depth profile in Fig. 8b. The surface structure in Fig. 15b also is predominately martensite but extends to a significantly greater depth than in Fig. 15a. Some indication of the recrystallized layer between the martensite and the cold-worked structure is evident at the bottom of the figure. The depth of the martensite layer in Fig. 15b varies from 70 to 100 μm. This compares reasonably well with the smooth portion of the ^{16}O profile extending from the surface of the specimen in Fig. 8d to a depth of about 80 μm. The ^{16}O profile in Fig. 8d continues to decrease beyond the smooth portion of the profile. Although this could be an artifact of both the surface morphology of the SIMS crater and memory effects caused by redeposition of ion-sputtered material in the instrument, it may imply that oxygen has diffused into the recrystallized material.

Carburizing. The depth of craters formed by laser-pulsing at a given beam energy significantly decreased as the gas pressure increased. Consequently, one of the deepest craters that formed was in Iron 70 from the low-pressure series of specimens. A low-magnification micrograph of a section through the crater is shown in Fig. 16a. The depth of the laser-affected structure can be seen to be much thicker at the rim on either side of the figure than at the center of the crater. This is shown at higher magnification in Figs. 16b and 16c. Figure 16b is from the center of the crater, and Fig. 16c is from one side of the rim. These structures correlate with the SIMS depth profiles presented in Figs. 10a and 10b, respectively. The SIMS profiles indicated that the surface material at the rim contained much more carbon and to significantly greater depth than in the center of the crater. As mentioned previously, these results imply that the surface material was either melted or softened by the thermal response to the laser beam, and the pressure pulse generated by the laser beam caused the material to be extruded from the center of the impacted region.

Comparison of the structures generated by laser-pulsing in 10% methane/argon and carbon monoxide is shown in Fig. 17. Figure 17a is from Iron 53, which received 10 pulses in 10% methane/argon at 150 psi with a 40-J beam, and Fig. 17b is from Iron 59, which received 10 pulses in carbon monoxide at 150 psi with a 40-J beam. The corresponding SIMS depth profiles from these specimens are shown in Figs. 9c and 11, respectively. Although differences in the martensitic structures of the two specimens are subtle, they are considered to be significant. The prior austenite grain size is faintly indicated in these figures by changes in the orientation of the martensite platelets. The prior austenite grain size appears to be significantly greater in Fig. 17a for Iron 53 than in Fig. 17b for Iron 59. The martensitic structures generated in other pure iron specimens by laser-pulsing in 10% methane/argon appeared to be quite similar to that shown in Fig. 17a for Iron 53. Therefore, the increased oxygen concentration induced by laser-pulsing in carbon monoxide appears to have promoted a finer grain size in the reaction zone. The difference in these structures strongly suggests that the increased oxygen content also may have increased the retained austenite content in Iron 59.[4]

Nitriding. Further change in the appearance of the martensitic structure occurred in specimens that were laser-pulsed in nitriding gases. Figure 18a is from Iron 61, which received 10 pulses in nitrogen at 150 psi with a 40-J beam, and Fig. 18b is from Iron 63, which received 10 pulses in ammonia at 100 psi with a 40-J beam. The corresponding SIMS depth profiles for these specimens were presented in Figs. 12a and 12b, respectively. The martensite platelets in the nitrided specimens appear to be more sharply delineated than in the previous specimens. The effect of the increased oxygen content in Iron 63 was not evident. The depth of the martensite layer in Fig. 18a varies from about 40 to 50 μm, and the depth in Fig. 18b is about 50 μm. This is in approximate agreement with the SIMS depth profiles.

AISI 4340 Steel Specimens

The AISI 4340 steel had a quenched and tempered martensitic structure. Examination of the laser-pulsed surfaces did not reveal evidence of plastic deformation. Only martensitic transformations and surface melting occurred. When surface melting occurred, two distinct zones formed. The

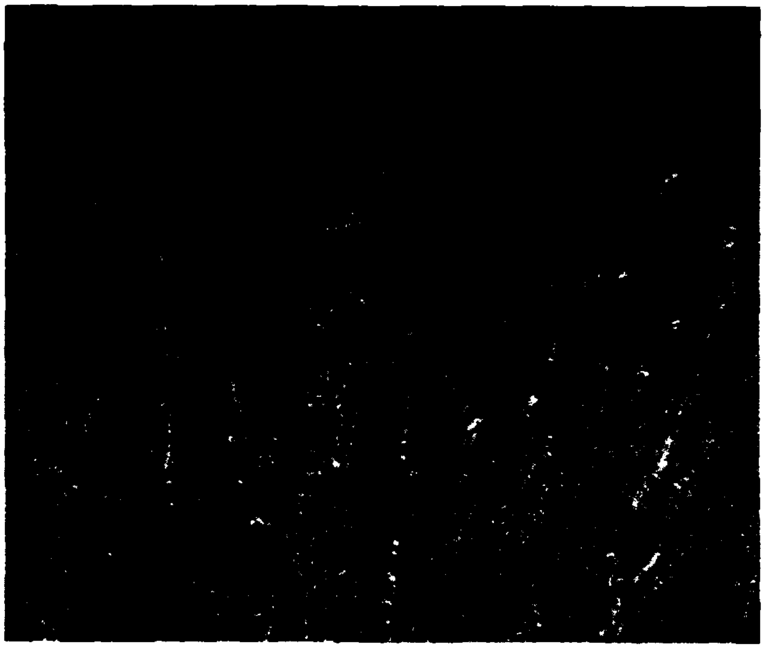

Fig. 14. Cold-worked structure of the pure iron (800×).

Fig. 15. Microstructural changes induced in pure iron by laser-pulsing in argon at 150 psi.

(a) Iron A, 10 pulses at 10 J (1000X).

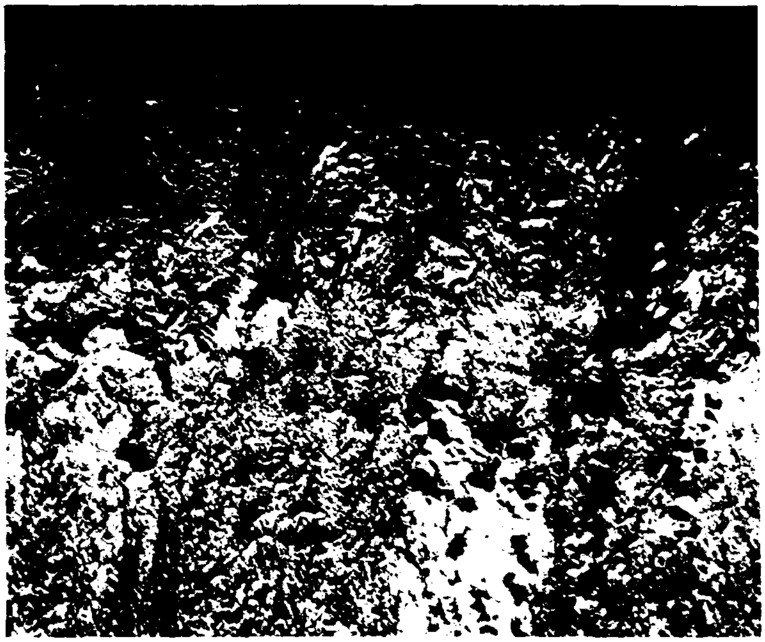

Fig. 15. (continued)

(b) Iron B, 10 pulses at 40 J (800X).

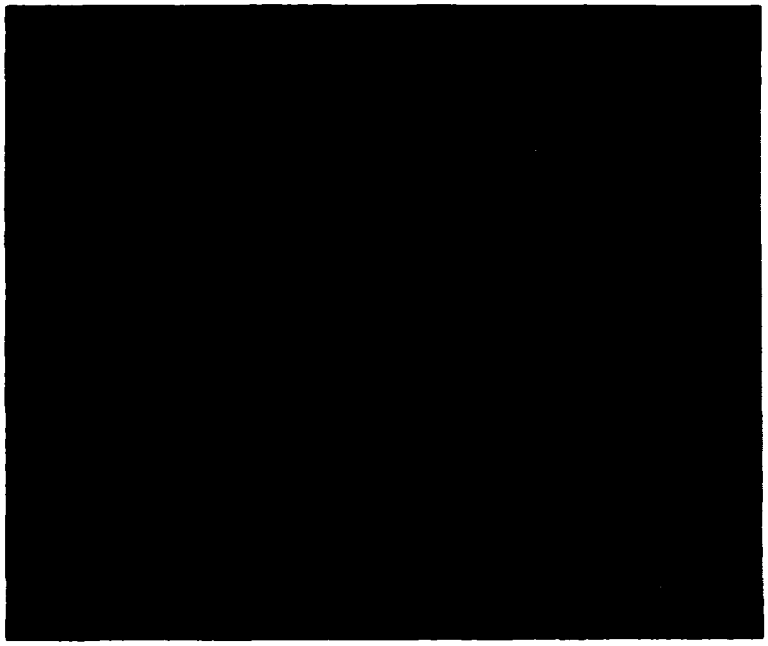

Fig. 16. Structures formed in the crater of Iron 70, which received 10 pulses in 10% methane/argon at 15 psi with a 40-J beam.

(a) Low-magnification view of the crater (50×).

Fig. 16. (continued)

(b) Structure at the center of the crater (800×).

(c) Structure at the rim of the crater (800×).

Fig. 17. Comparison of pure iron specimens laser-pulsed in 10% methane/argon and carbon monoxide (1000×).

(a) Iron 53, 10% methane/argon, 10 pulses, 150 psi, 40 J.

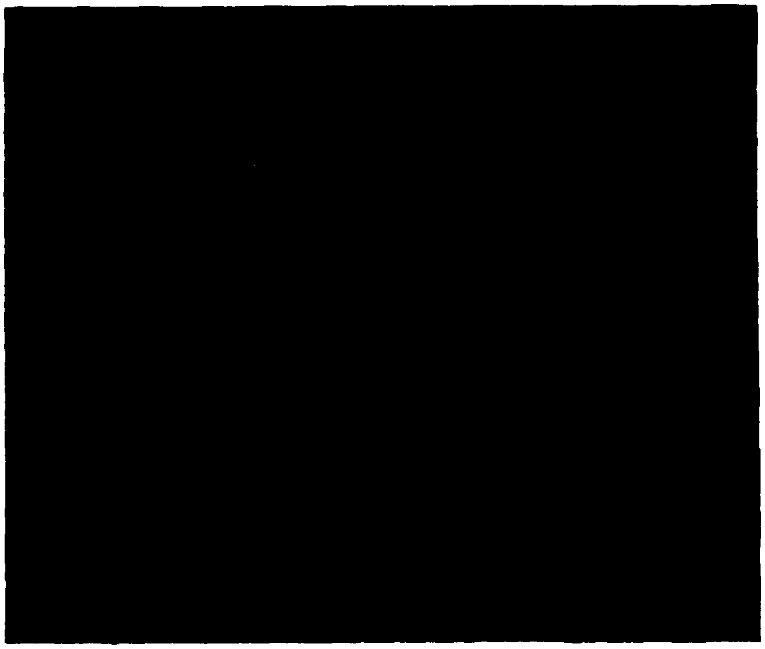

(b) Iron 59, carbon monoxide, 10 pulses, 150 psi, 40 J.

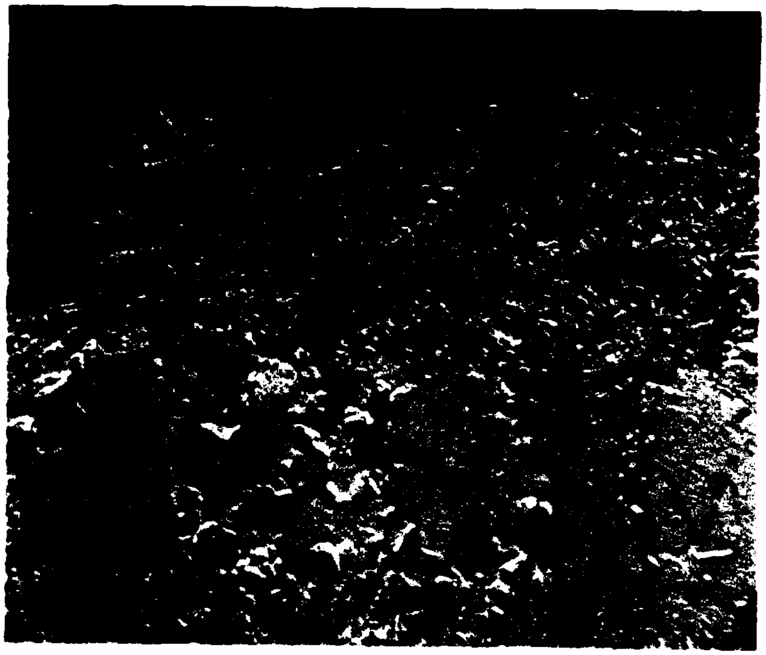

Fig. 18. Pure iron specimens laser-pulsed in nitriding gases (800×).

(a) Iron 61, nitrogen, 10 pulses, 150 psi, 40 J.

(b) Iron 63, ammonia, 10 pulses, 150 psi, 40 J.

zone formed at the surface was light-etching, as-quenched martensite. This was followed by a zone of intermediate-etching martensite. The constant appearance of the etched structure in the intermediate zone suggests that the A_{c3} temperature for the complete transformation of the prior structure to austenite had been exceeded. This in turn suggests that the light-etching zones had exceeded the melting point, although the position of the melting interface was not apparent in the metallographic examinations. The martensitic structures in the AISI 4340 steel specimens did not appear to be sensitive to the gaseous environment. This is shown in Figs. 19 and 20.

The microstructures in the light- and intermediate-etching zones were similar to those found in the first two zones in the previous investigation.[1] Whereas the substrate structure was tempered martensite in this study, the substrate structure was ferrite and pearlite in the previous study. Consequently, a third zone was detected in the previous study that was suspected to correspond to the zone that exceeded the A_{c1} temperature for the start of the transformation to austenite on heating but did not exceed the A_{c3} temperature for the complete transformation to austenite. Apparently, the detection of this zone in the previous study was enhanced by its sharp contrast to the pearlitic structure.

Figure 19 is from metallographic cross sections of some of the AISI 4340 steel specimens that showed the laser-affected surface structures. Figures 19a and 19b compare specimens that were laser-pulsed with different beam energies in argon. Figure 19a is from 4340 A, which received 10 pulses in argon at 150 psi with a 10-J beam, and Fig. 19b is from 4340 B, which received 10 pulses in argon at 150 psi with a 40-J beam. Views of the surface damage were shown in Figs. 7a and 7b, respectively. Figure 19a is from the central damaged region in Fig. 7a and shows that the light-etching layer did form at the surface in this region. Figure 19b is from the crater in Fig. 7b and shows an even thicker light-etching layer. Figures 19c and 19d compare specimens that received different numbers of pulses in 10% methane/argon at 150 psi with a 40-J beam. The surface damage that occurred in these specimens is shown in Figs. 7c and 7d, respectively. The light-etching layers appeared to be noticeably thicker in specimens pulsed in 10% methane/argon than in specimens pulsed in argon. The irregularities in the surface layers of these specimens reflect the surface roughness caused by melting and inhomogeneities in the energy density of the laser beam.

The surface structures in Figs. 19a through 19d are shown at higher magnifications in Figs. 20a through 20d, respectively. These figures show the light-etching and intermediate-etching martensitic structures more clearly. In contrast to the pure iron specimens, the structures do not appear to be sensitive to the environment. As mentioned previously, the light-etching martensite appeared to be associated with surface melting, but the depth of melting was not indicated in the microstructure.

The thickness of the light-etching layer was only about 1 to 2 μm in 4340 A. This implies that 10 J is near the threshold energy for surface melting to occur in AISI 4340 steel. The thickness of the light-etching layer in 4340 50 was about 10 to 12 μm (Fig. 20c), and it was about 18 to 25 μm in 4340 43 (Fig. 20d). The thickness of the intermediate-etching layer was about 30 μm (Figs. 20c and 20d). The thickness of the light-etching layer definitely appears to increase as the number of pulses increases. This is supported by the ^{16}O profile in Fig. 13c. The flat portion of the ^{16}O profile at an ion intensity of about 10^4 counts/s may be associated with the light-etching layer, although it extends to a depth of about 40 μm. As mentioned previously, the portion of the profile extending from a depth of about 40 μm to about 80 μm decreases smoothly from about 10^4 to about 4×10^3 counts/s, and this could be related to diffusion of oxygen into the intermediate-etching layer. In addition, the ^{16}O profile in Fig. 13c descends from slightly above 10^5 counts/s to 10^4 counts/s within a depth of about 10 μm below the surface. If this is related to the increased solubility of oxygen in molten iron, this would indicate that surface melting extended only partially into the light-etching layer.

Scanning Electron Microscopy

Pure Iron Specimens

Argon. Scanning electron micrographs of the laser-affected regions in pure iron specimens pulsed in argon at 150 psi with a 10-J beam are shown in Fig. 21. Figure 21a shows the laser-affected region at low magnification; this corresponds to the optical macrograph of the same area in Fig. 2a, which was taken before the SIMS analyses. The light triangular areas in Fig. 21a are craters generated by the primary ion beam during

Fig. 19. Comparison of low-magnification views of laser-affected surface structures in AISI 4340 steel specimens (100×).

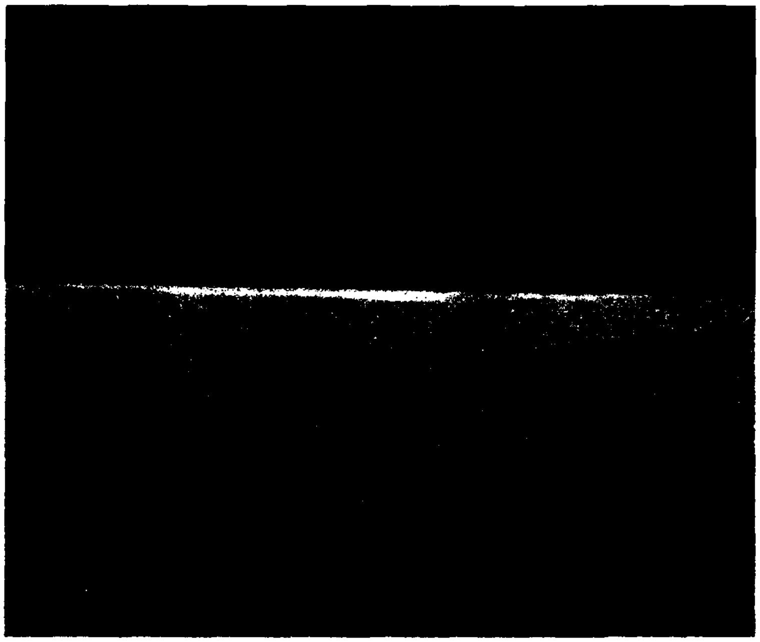

(a) 4340 A, 10 pulses in argon, 150 psi, 10 J.

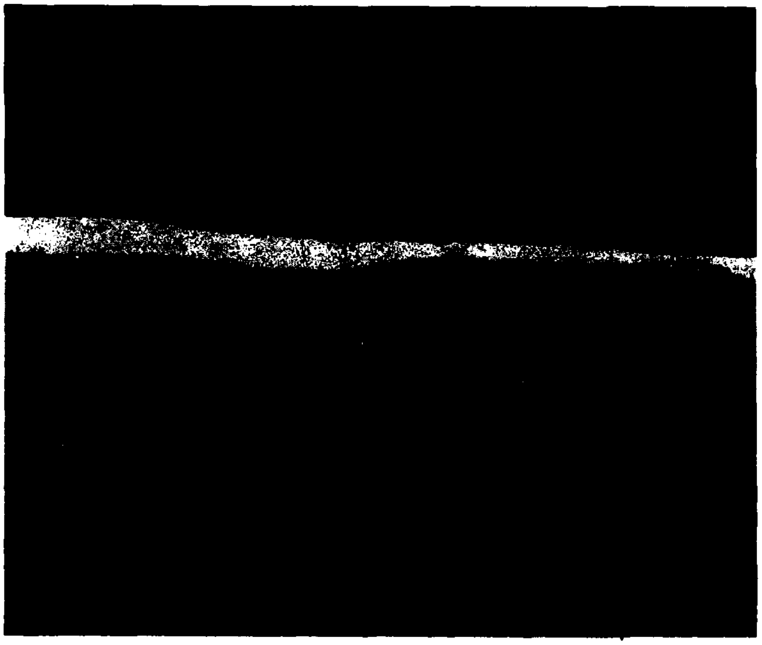

(b) 4340 B, 10 pulses in argon, 150 psi, 40 J.

Fig. 19. (continued)

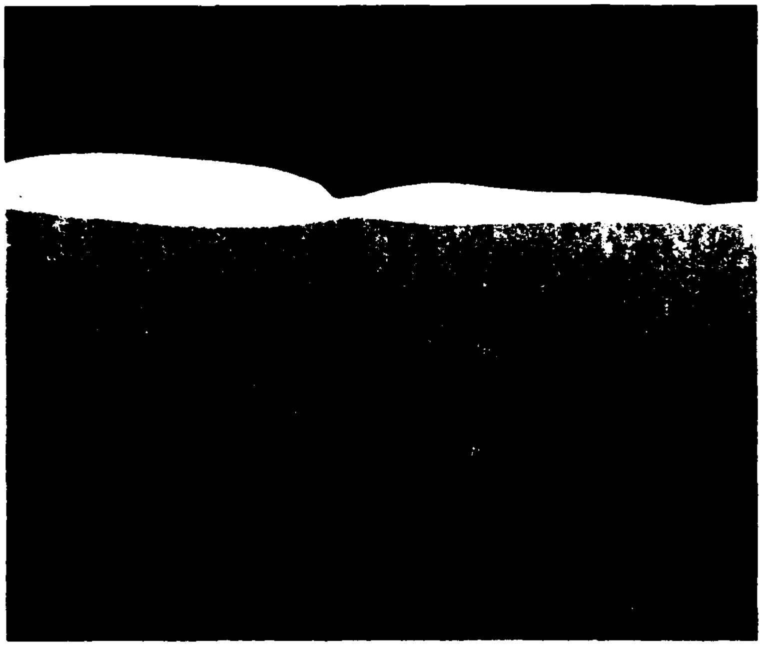

(c) 4340 50, 1 pulse in 10% methane/argon, 150 psi, 40 J.

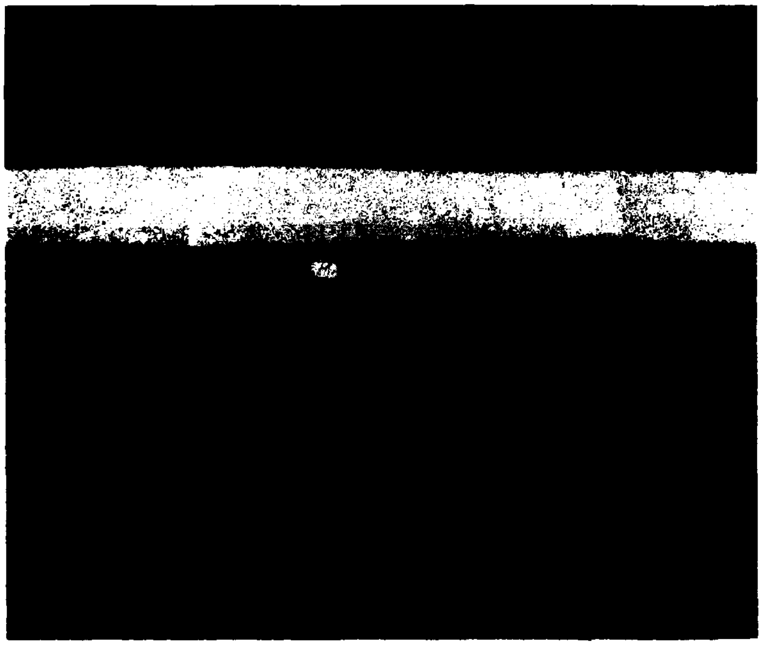

(d) 4340 43, 10 pulses in 10% methane/argon, 150 psi, 40 J.

Fig. 20. High-magnification views of the microstructural changes in laser-pulsed AISI 4340 steel specimens (1000×).

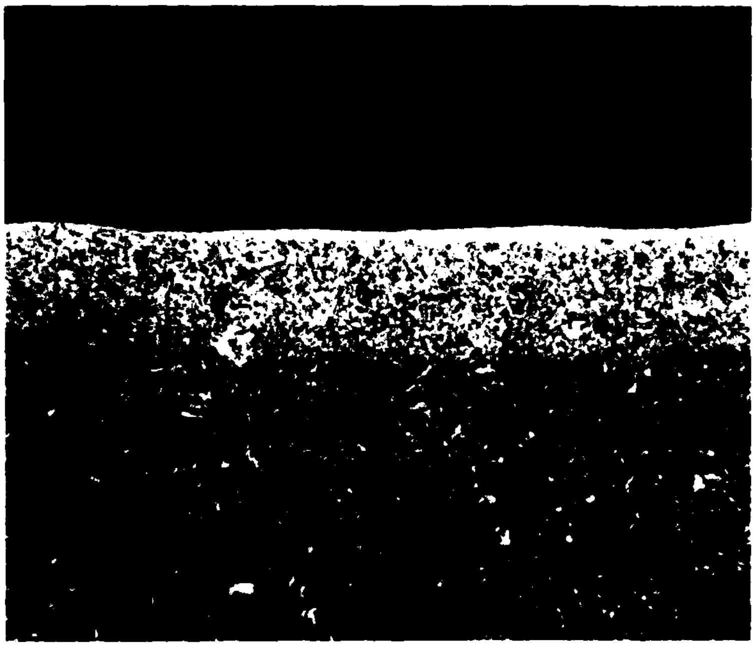

(a) 4340 A, 10 pulses in argon, 150 psi, 10 J.

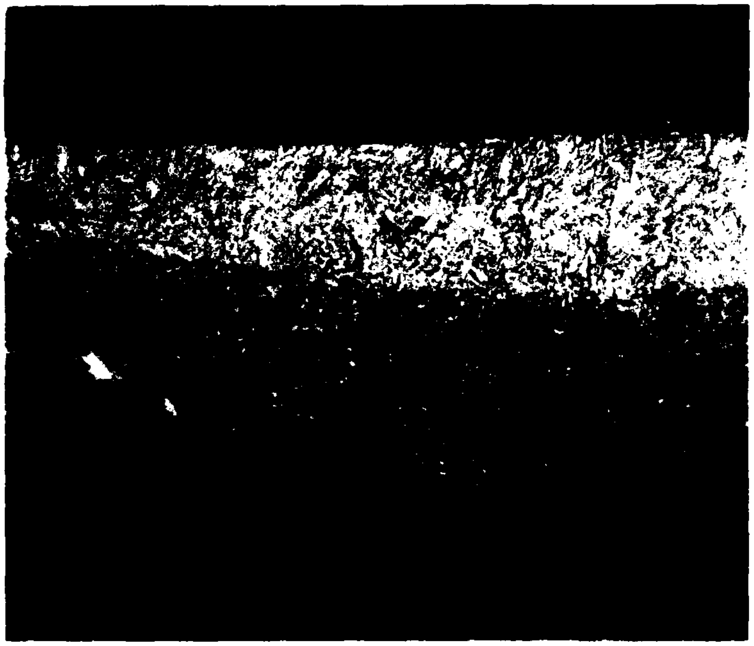

(b) 4340 B, 10 pulses in argon, 150 psi, 40 J.

Fig. 20. (continued)

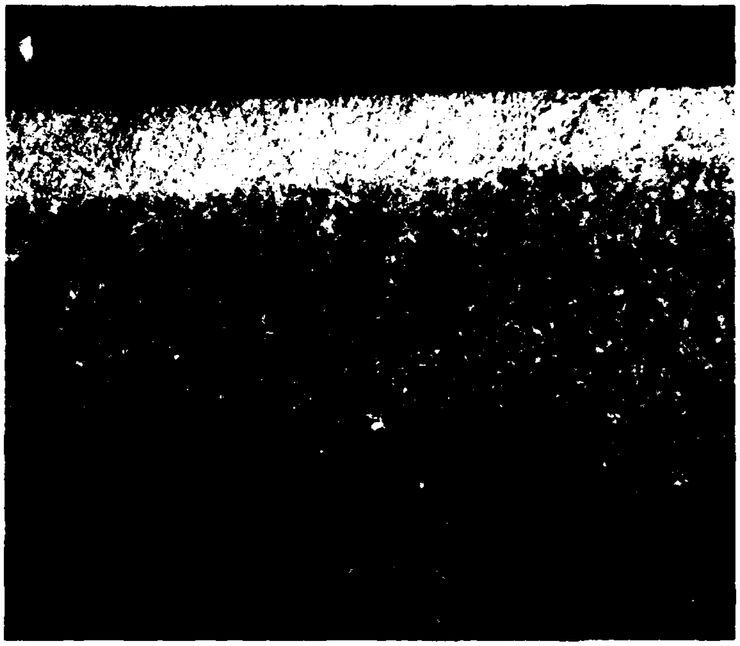

(c) 4340 50, 1 pulse in 10% methane/argon, 150 psi, 40 J.

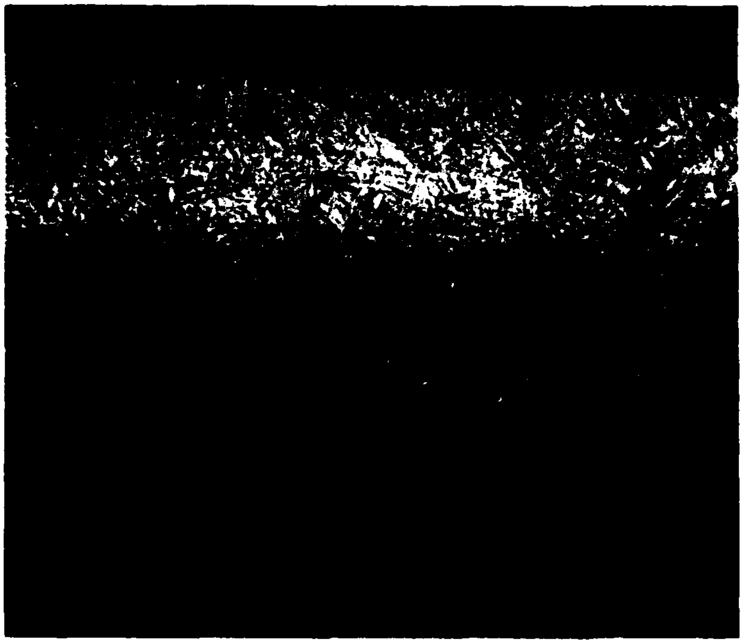

(d) 4340 43, 10 pulses in 10% methane/argon, 150 psi, 40 J.

Fig. 21. Scanning electron micrographs of Iron A, 10 pulses in argon at 150 psi with a 10-J beam.

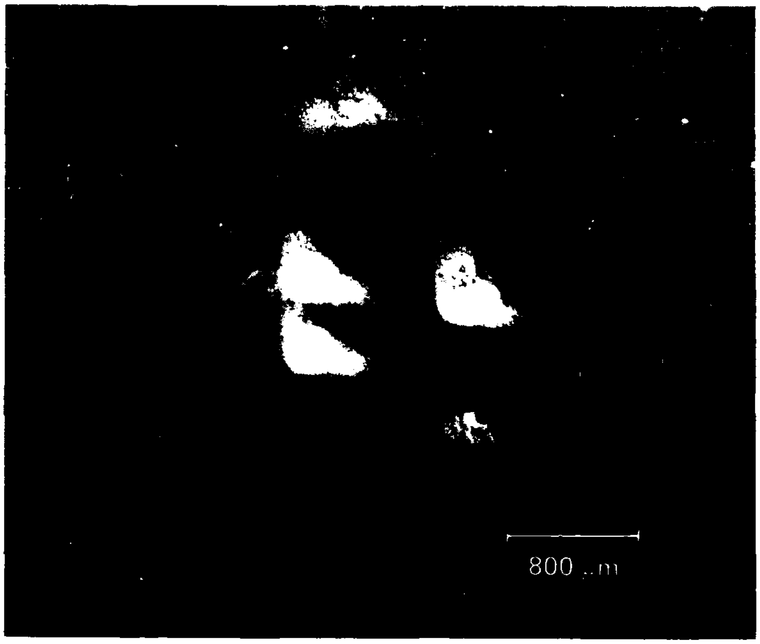

(a) Low-magnification view of the laser-affected region.

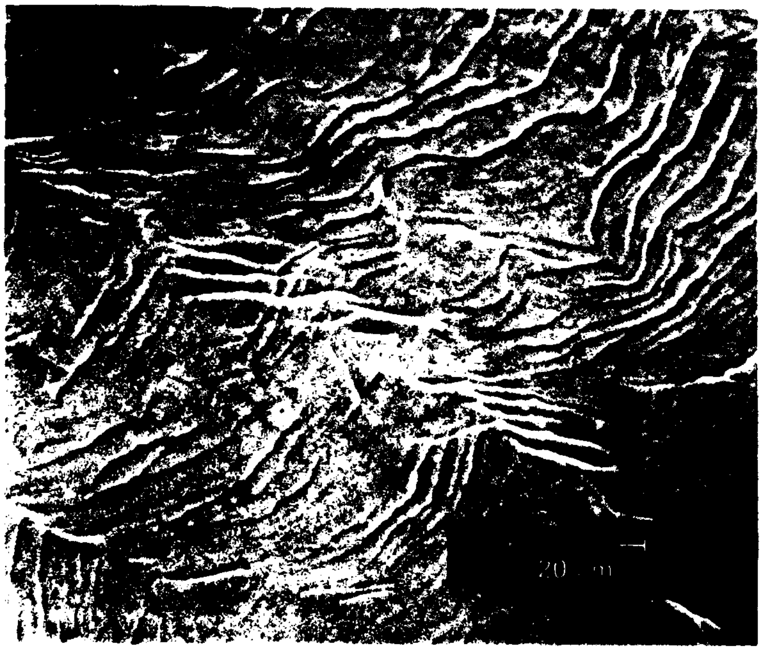

(b) Slip bands formed at the edge of the laser-affected region.

Fig. 21. (continued)

(c) Transition area from slip to a deformed recrystallized structure.

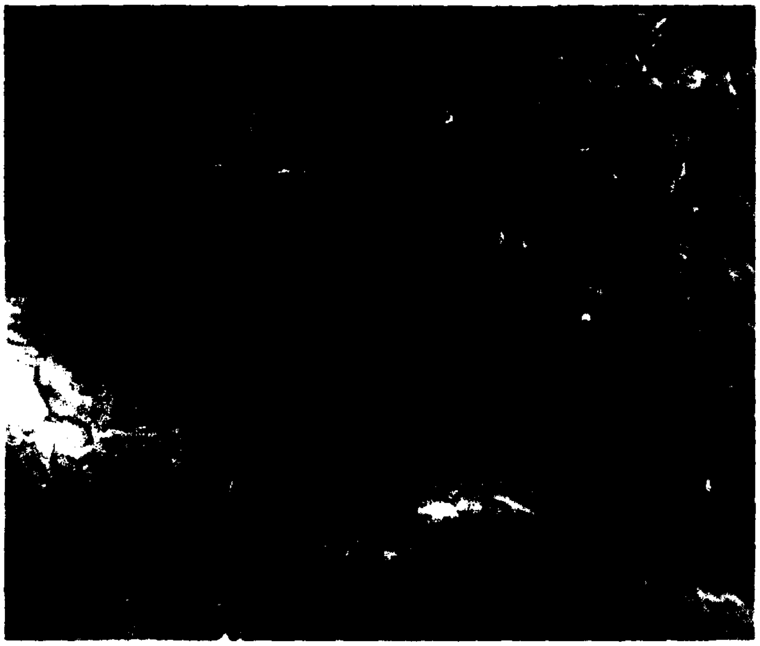

(d) Martensitic structure in the center of the laser-affected region.

the SIMS analyses. Examples of slip bands formed in Iron A are shown in Fig. 21b. These slip bands were found in the lightly damaged areas of the specimen. They are characteristic of the slip bands found around the edges of the laser-affected regions of all of the pure iron specimens. A transition zone between slip and recrystallization in Iron A is shown in Fig. 21c; as can be seen, banded structures usually were associated with the recrystallized structures. Optical metallography indicated that martensite had not formed in this area, so the bands are interpreted to be deformation bands formed by the rapid thermal response of the specimen to the laser beam (Appendix 4). The small area near the center of Fig. 21a, and which also is shown in the optical macrograph in Fig. 2a, appears to have melted. The structure from this region is shown at higher magnification in Fig. 21d. This area shows a fine grain structure, apparently formed by rapid solidification, and optical metallography indicated that the banded structure in this area is associated with martensite platelets and not deformation. Frequently, a mottled structure formed between the recrystallized and the melted areas. Optical metallography indicated that solid-state austenite-martensite transformations had occurred in these areas.

Scanning electron micrographs from the laser-affected region of Iron B are shown in Fig. 22. An optical macrograph of the same region was shown in Fig. 2b. This specimen had been pulsed in argon under the same conditions as Iron A except for a higher beam energy of 40 J. Essentially the same damage zones formed in this specimen as in Iron A, but the higher beam energy produced considerably more surface damage, as can be seen in Fig. 22a. The structure from the central portion of the melted region is shown in Fig. 22b. The structure in this figure is nearly identical to that in Fig. 21d. Again, metallography indicated that the bands were associated with the formation of martensite.

10% Methane/Argon. Surface structures formed on pure iron specimens pulsed in 10% methane/argon are shown in Figs. 23 through 25. The laser-affected region on the surface of Iron 70, which was pulsed 10 times with a 40-J beam at 15 psi, is shown in Figs. 23a through 23d. Areas analyzed by SIMS are again visible. The depth of the crater can be seen to be significantly greater than the small crater that formed in Iron B at 150 psi (Fig. 22a). It also is significantly deeper than the craters formed in the other pure iron specimens pulsed at 150 psi in 10% methane/argon. Evidence of surface melting within the crater is indicated by the globular appearance of the surface structure in Fig. 23b. The globular structure appears to be associated with dendritic solidification, as will be discussed. This contrasts sharply with the structures from the melted regions in Iron A and Iron B in Figs. 21a and 22a, respectively, and demonstrates the sensitivity of surface structures generated by laser-pulsing to the environment. Martensitic banding usually could be seen to be superimposed on the fine globular structure at lower magnification. Figure 23c was taken from an area just outside of the rim of the crater. Recrystallization had occurred, and optical metallography indicated that the bands are associated with martensite. Faint evidence of the globular structure can be seen in some areas of Fig. 23c as if incipient melting had occurred. Figure 23d is from the rim of the crater. Small surface tears appear to have formed in the recrystallized structure in Fig. 23d. This is consistent with the suggestion that the crater formed by the extrusion of material from the center of the crater.

Structures from the melted regions of pure iron specimens that received from one to 50 pulses in 10% methane/argon are shown at intermediate magnifications in Fig. 24 and at higher magnification in Fig. 25. These specimens were laser-pulsed at 150 psi with a 40-J beam. Figure 24a is from Iron 50, which received one pulse, and shows only a recrystallized structure with a superimposed martensitic structure; no evidence of the globular structure was evident. The morphology of the crater definitely indicated that surface melting had occurred. Figure 24b, from Iron 51 which received two pulses, shows a similar structure with faint evidence of the globular structure. Figures 24c and 24d, from Iron 52 which received five pulses and Iron 55 which received 50 pulses, respectively, show well-developed globular structures. For purposes of comparison, additional examples of globular structures are shown at higher magnifications in Figs. 25a through 25d. In Fig. 25a, the globular structure appears to be in the initial stage of formation after two pulses. In Fig. 25b, the globular structure appears to be fairly well formed after five pulses. Figures 25c and 25d show that no further changes have occurred in the appearance of the globular structure after 25 and 50 pulses. These figures indicate that two to five

Fig. 22. Scanning electron micrographs of Iron B, 10 pulses in argon at 150 psi with a 40-J beam.

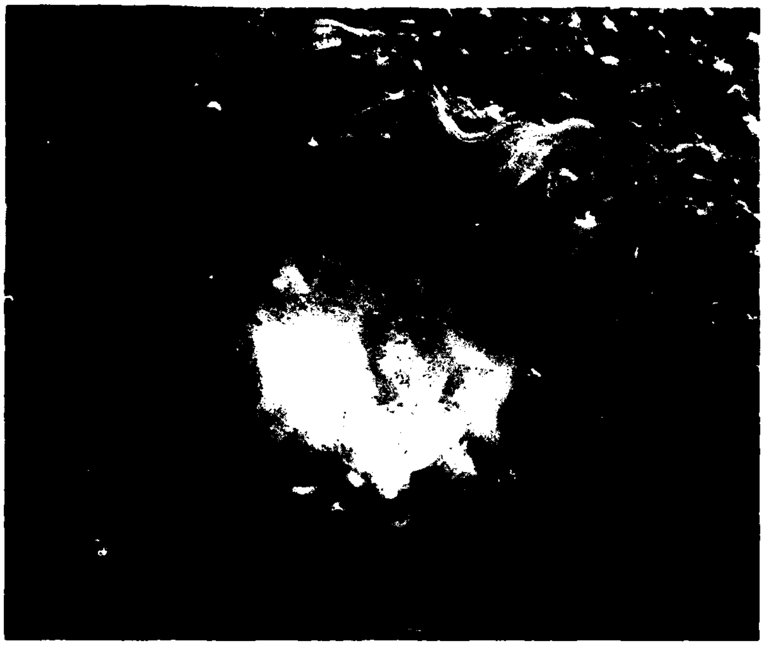

(a) Low-magnification view of the laser-affected region.

(b) Martensitic structure in the center of the melted region.

Fig. 23. Scanning electron micrographs of Iron 70, 10 pulses in 10% methane/argon at 15 psi with a 40-J beam.

(a) Low-magnification view of the crater formed at low pressure.

(b) Evidence of surface melting in the center of the crater.

Fig. 23. (continued)

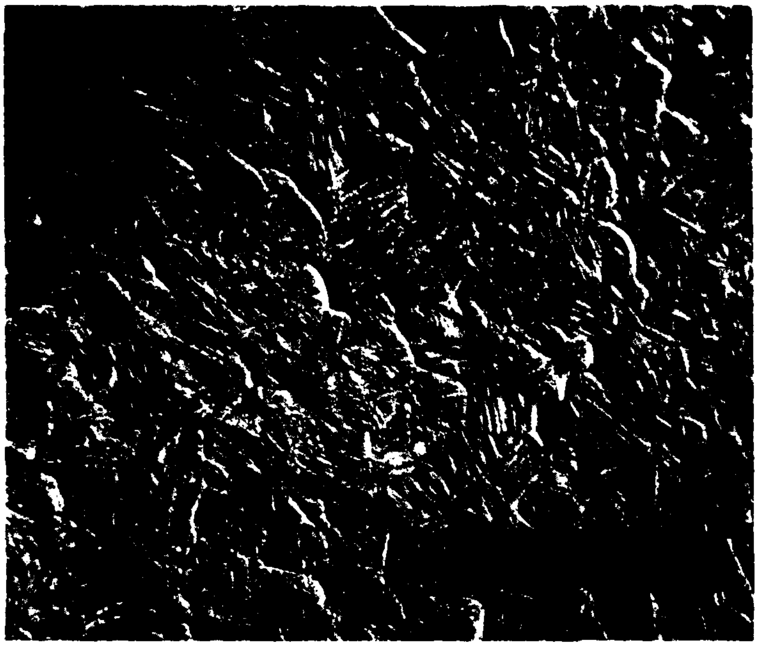

(c) Recrystallized structure at the outer edge of the rim with martensite platelets.

(d) Evidence of surface tearing on the rim.

Fig. 24. Scanning electron micrographs from the centers of the laser-affected regions of pure iron specimens after different numbers of pulses in 10% methane/argon at 150 psi with a 40-J beam.

(a) Iron 50, 1 pulse.

(b) Iron 51, 2 pulses.

Fig. 24. (continued)

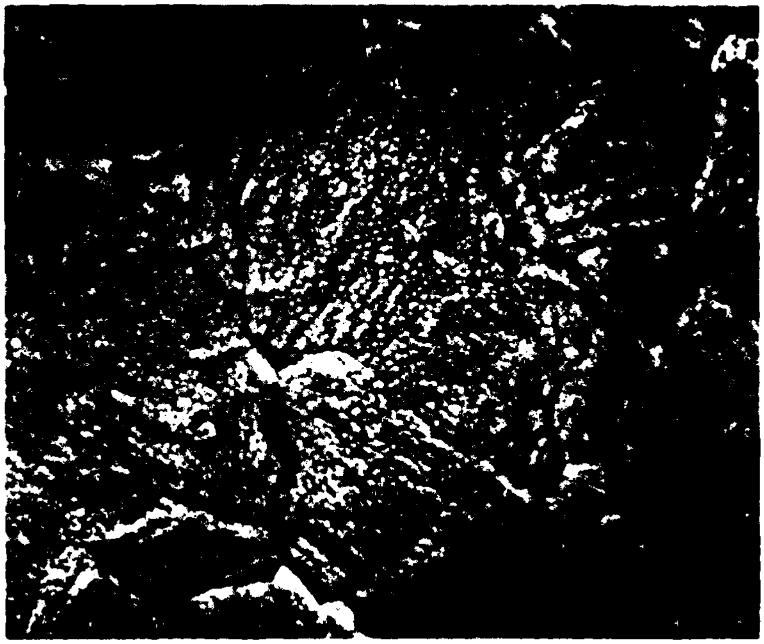

(c) Iron 52, 5 pulses.

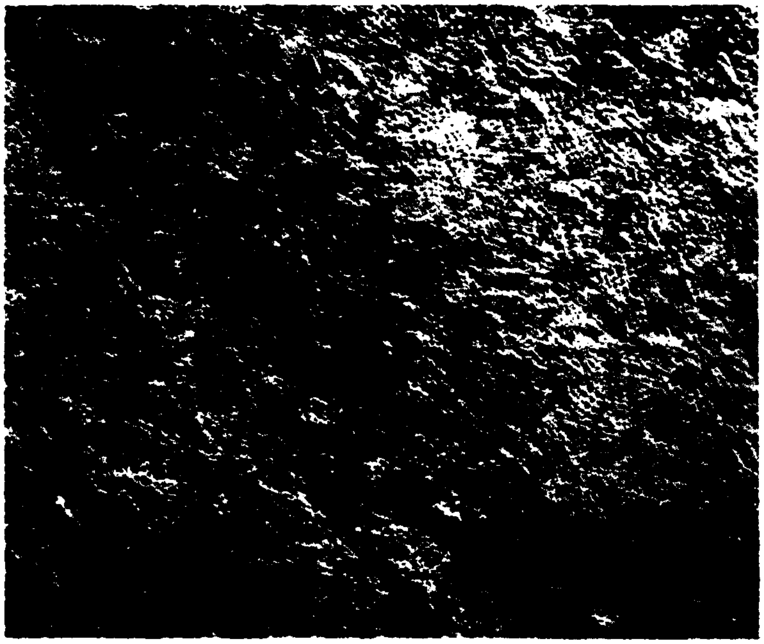

(d) Iron 55, 50 pulses.

Fig. 25. Comparison of surface melting in pure iron specimens after different numbers of pulses in 10% methane/argon at 150 psi with a 40-J beam.

(a) Iron 51, 2 pulses.

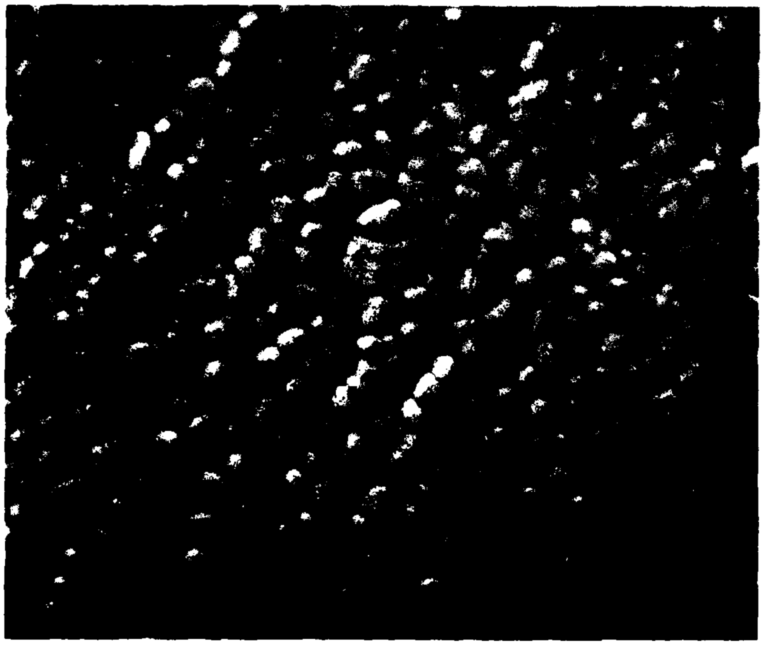

(b) Iron 52, 5 pulses.

Fig. 25. (continued)

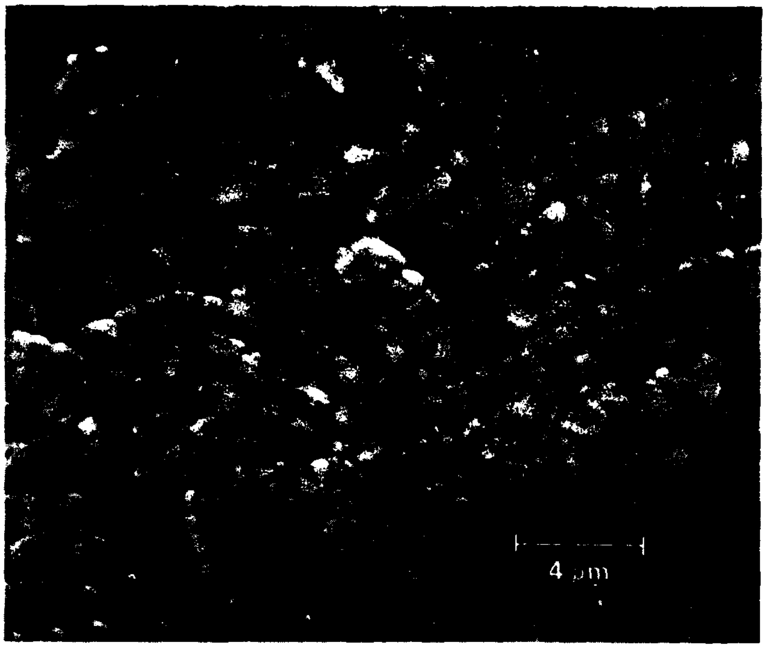

(c) Iron 54, 25 pulses.

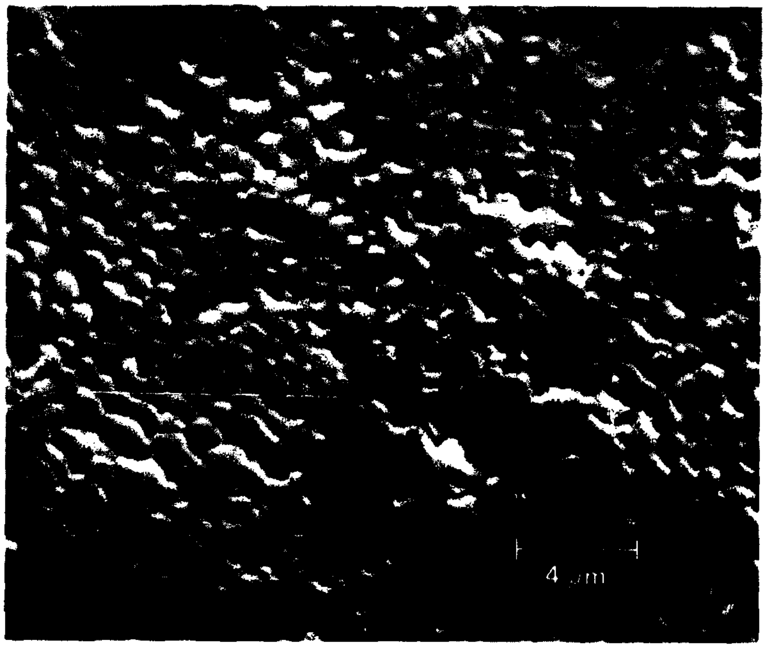

(d) Iron 55, 50 pulses.

pulses were required to form the globular structure, and it remained fairly constant once it formed.

Other Gases. In contrast to the pure iron specimens pulsed in 10% methane/argon, the globular structure did not form in carbon monoxide, nitrogen, or ammonia. This is shown in Fig. 26, from the melted region of Iron 59 which was pulsed 10 times in carbon monoxide at 150 psi with a 40-J beam, and Fig. 27, from Iron 61 which was pulsed 10 times in nitrogen at 150 psi with a 40-J beam. The surface structure in Iron 63, which was pulsed 10 times in ammonia at 100 psi, was nearly identical to that of Iron 61. The martensitic relief in the nitrided specimens appears to be much more sharply delineated than that in the specimens pulsed in 10% methane/argon and argon, and this is consistent with the metallographic observations.

AISI 4340 Steel Specimens

The laser-affected regions from 4340 A and 4340 B, which were pulsed 10 times in argon at 150 psi, are shown in Figs. 28a and 28b, respectively. These figures correspond with the optical macrographs of the same regions in Figs. 7a and 7b, respectively. Slight evidence of melting can be seen in Fig. 28a from 4340 A, which was pulsed with a 10-J beam, and a large melted region is evident in Fig. 28b from 4340 B, which was pulsed with a 40-J beam. Structures from the melted regions of AISI 4340 steel specimens pulsed in both argon and 10% methane/argon at 150 psi are shown at intermediate magnifications in Fig. 29. Figure 29a is from 4340 A, which received 10 pulses in argon with a 10-J beam, Fig. 29b is from 4340 B, which received 10 pulses in argon with a 40-J beam, Fig. 29c is from 4340 50, which received one pulse in 10% methane/argon with a 40-J beam, and Fig. 29d is from 4340 43, which received 10 pulses in 10% methane/argon with a 40-J beam. The same structures are shown at higher magnifications in Figs. 30a through 30d. These figures show that the globular structure did not form in argon with a 10-J beam, but it did form in argon with a 40-J beam, and it also was well developed in 10% methane/argon after only one pulse at 40 J. The fine, bright precipitates visible on the globular structure in Fig. 30b probably are associated with incipient oxidation, as indicated by the increased oxygen content in the SIMS depth profiles.

Preferential Response of Inclusions

One of the observations in the early phases of this study was that inclusions exhibited preferential response to laser-pulsing. This is demonstrated in Fig. 31 for an AISI 4340 steel specimen that had received one pulse in argon at 15 psi. The surface had been ground on a series of silicon carbide papers through 600 grit. The grinding scratches provide a useful reference for the onset of surface damage. The as-ground surface is shown in Fig. 31a. Figure 31b shows preferential response of inclusions at the edge of a lightly damaged area. One of the inclusions near the center of the figure has reacted to damage the surrounding surface. The inclusion is shown at higher magnification in Fig. 31c. The grinding scratches in the immediate vicinity of the inclusion appear to be unaffected by the laser pulse, and this indicates that the inclusion responded to the laser pulse more rapidly than the steel substrate. Figure 31d is from the edge of a melted area and shows that preferential response of inclusions has significantly altered the surface morphology. Additional evidence of preferential response of inclusions to laser-pulsing is shown in Figs. 32a and 32b. Figure 32a is from 4340 50, which received one pulse in 10% methane/argon at 150 psi with a 40-J beam, and Fig. 32b is from 4340 43, which received 10 pulses under the same conditions. Even though this preferential response undoubtedly is enhanced by the optical properties of the inclusions, it strongly suggests that inclusions may seriously affect erosion/corrosion in highly transient environments.

Coating Experiments

As already mentioned, the previous experiments[1] on tungsten-coated AISI 4340 steel specimens indicated that the tendency for tungsten coatings to crack was related to the thickness of the intermediate nickel layer. To duplicate the previous experiments, each tungsten-coated AISI 4340 steel specimen was pulsed 10 times in air at a given laser-beam energy. Nominal beam energies of 10, 20, 30, and 40 J were used. Three specimens with the different intermediate nickel-coating thicknesses of 2, 6, and 10 μm were pulsed at each energy. The test matrix is given in Table 4.

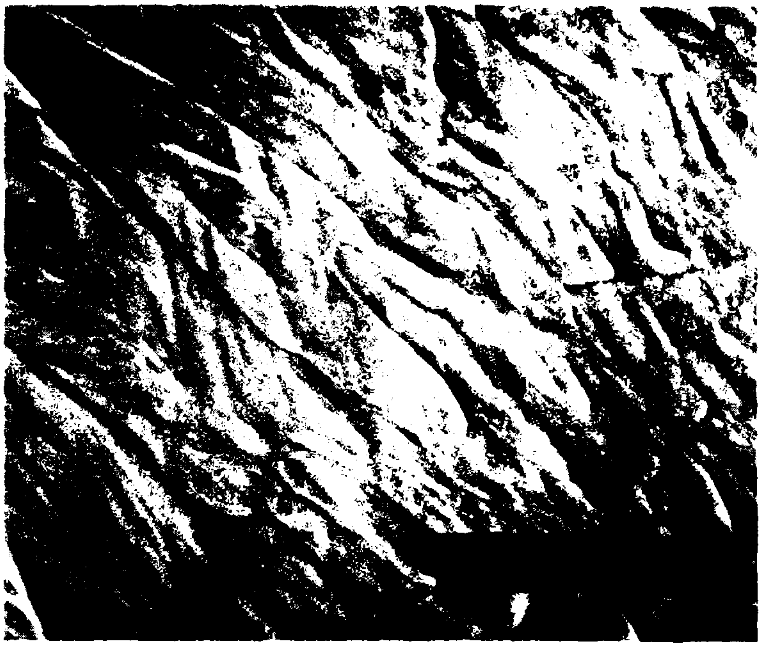

Fig. 26. Structure at the center of the laser-affected region of Iron 59 pulsed in carbon monoxide at 150 psi with a 40-J beam.

Fig. 27. Structure at the center of the laser-affected region of Iron 61 pulsed in nitrogen at 150 psi with a 40-J beam.

Fig. 28. Scanning electron micrographs of the laser-affected regions in AISI 4340 steel specimens after 10 pulses in argon at 150 psi.

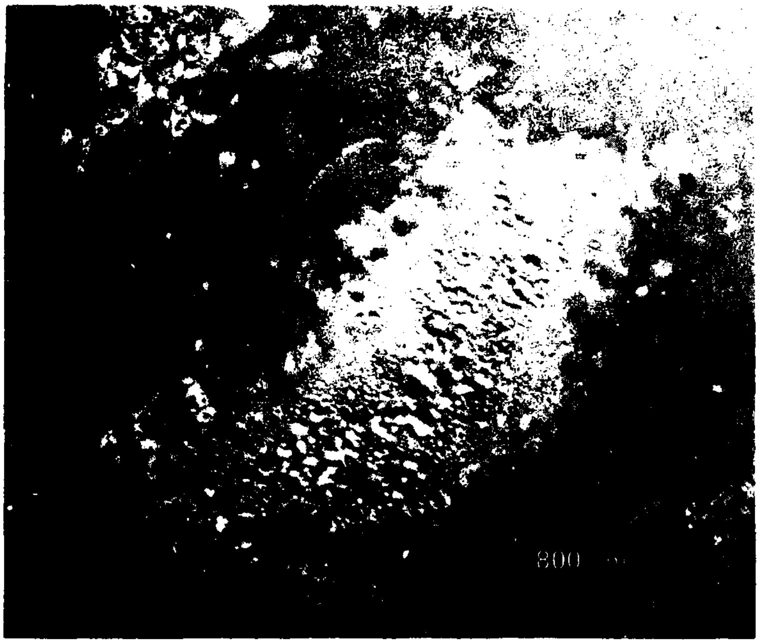

(a) 4340 A, pulsed with a 10-J beam.

(b) 4340 B, pulsed with a 40-J beam.

Fig. 29. Comparison of the surface structures at the centers of the laser-affected regions in AISI 4340 steel specimens.

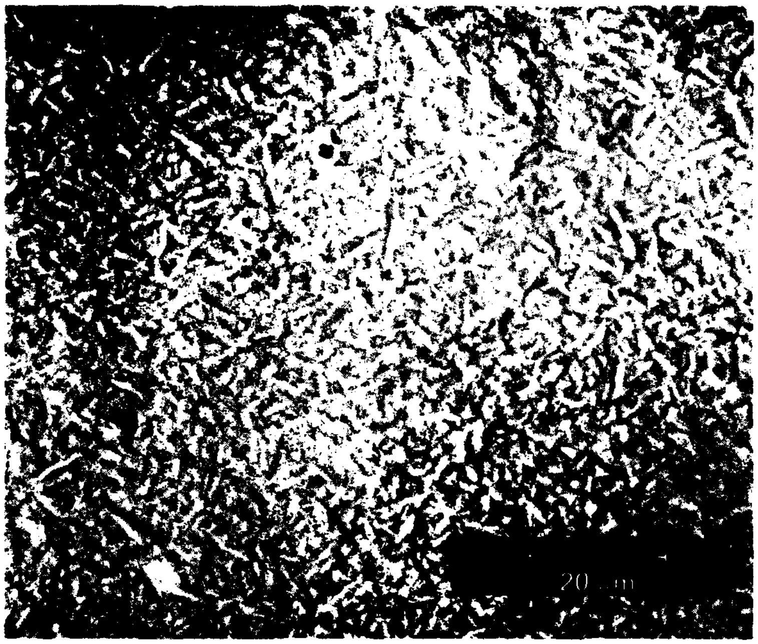

(a) 4340 A, argon, 150 psi, 10 J, 10 pulses.

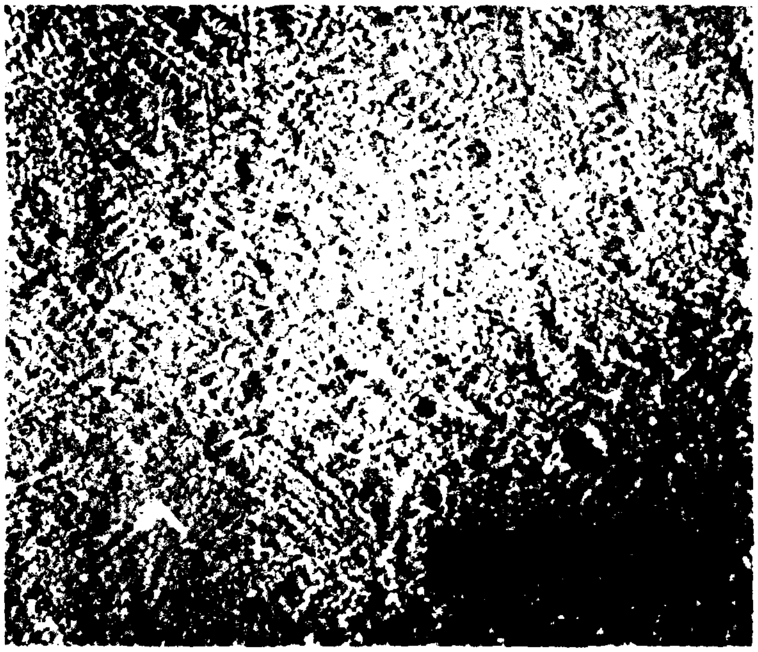

(b) 4340 B, argon, 150 psi, 40 J, 10 pulses.

Fig. 29. (continued)

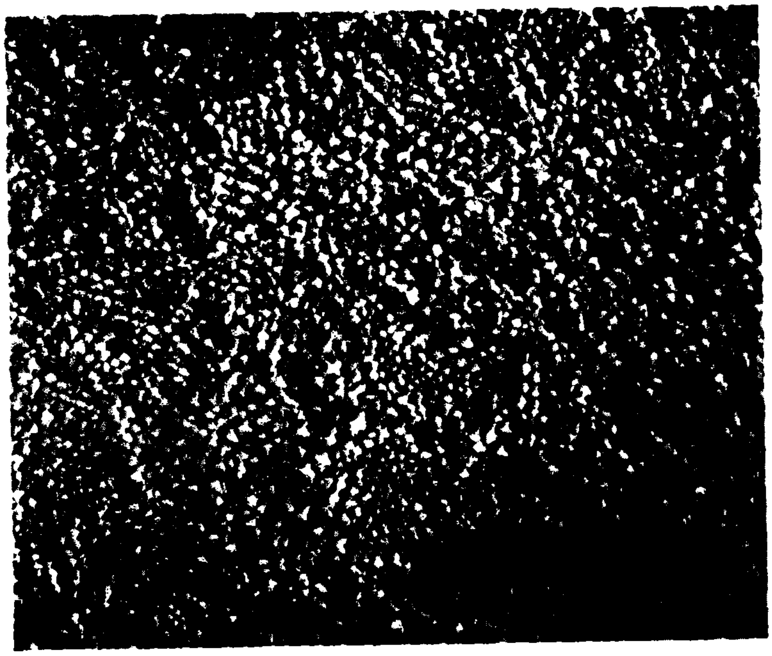

(c) 4340 50, 10% methane/argon, 150 psi, 40 J, 1 pulse.

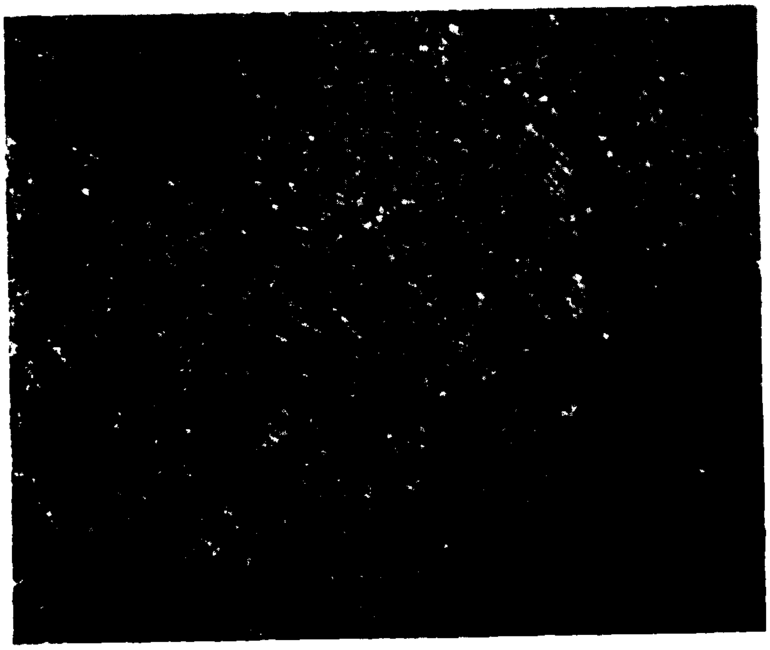

(d) 4340 43, 10% methane/argon, 150 psi, 40 J, 10 pulses.

Fig. 30. Higher-magnification views of the structures shown in Fig. 29.

(a) 4340 A, argon, 150 psi, 10 J, 10 pulses.

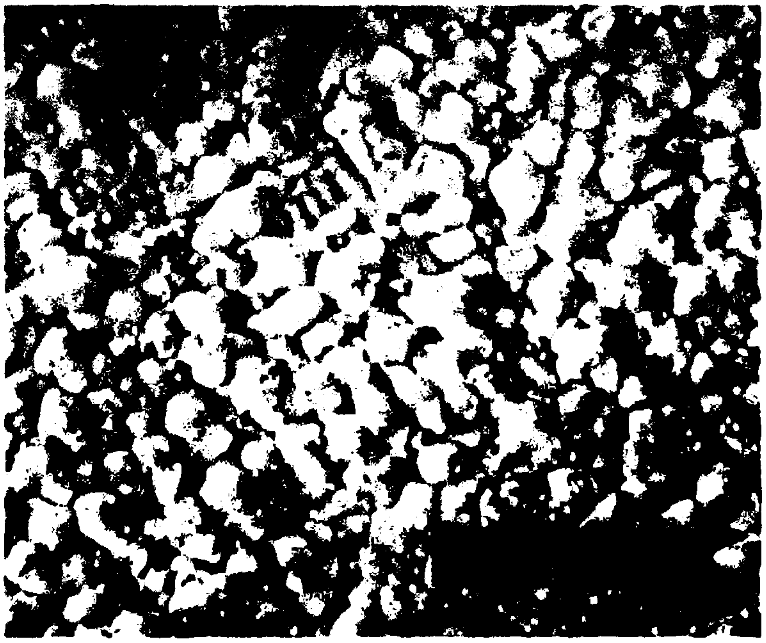

(b) 4340 B, argon, 150 psi, 40 J, 10 pulses.

Fig. 30. (continued)

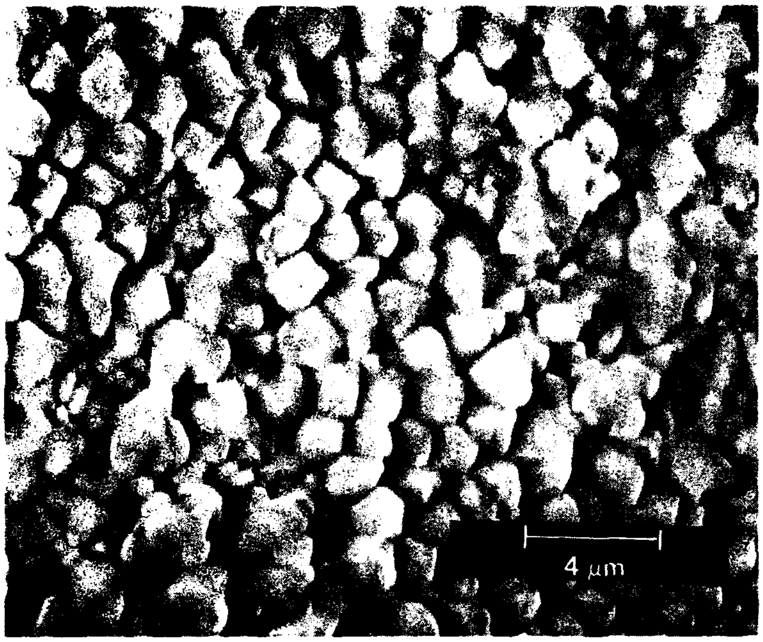

(c) 4340 50, 10% methane/argon, 150 psi, 40 J, 1 pulse.

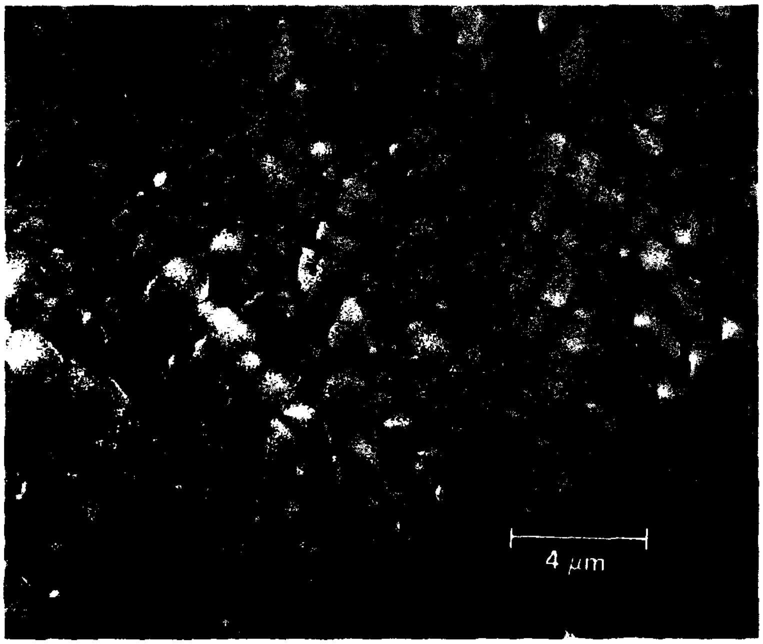

(d) 4340 43, 10% methane/argon, 150 psi, 40 J, 10 pulses.

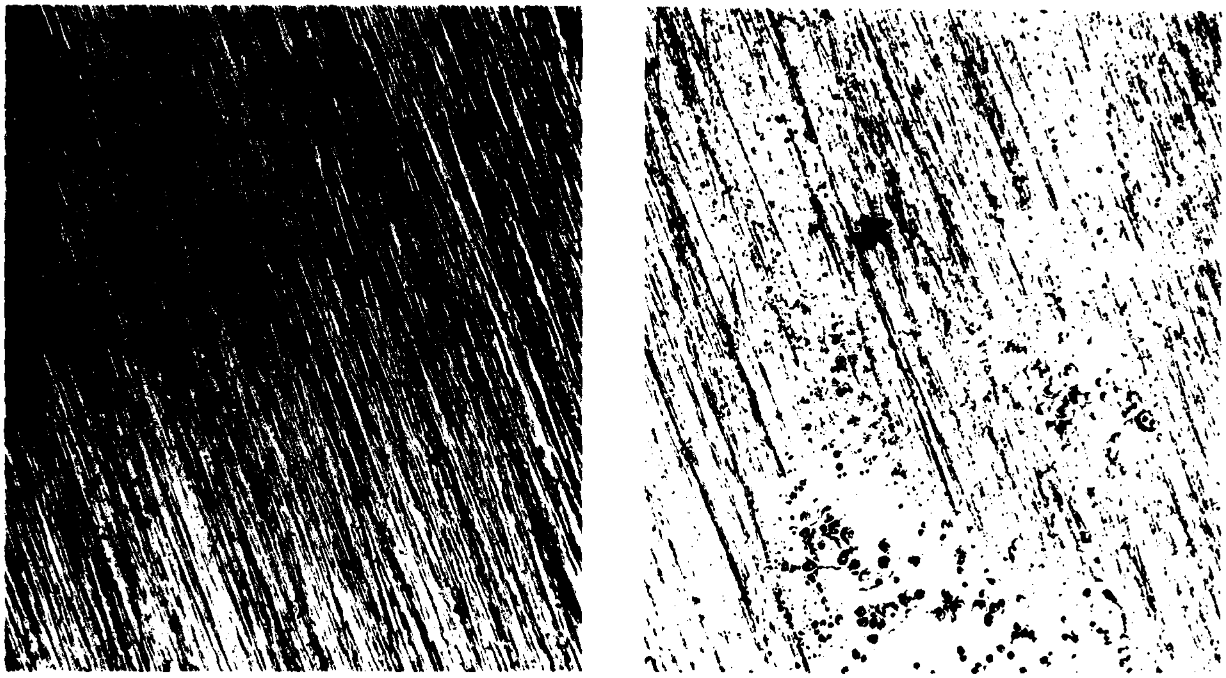

(a) As-ground surface (160×). (b) Edge of a lightly damaged area (80×).

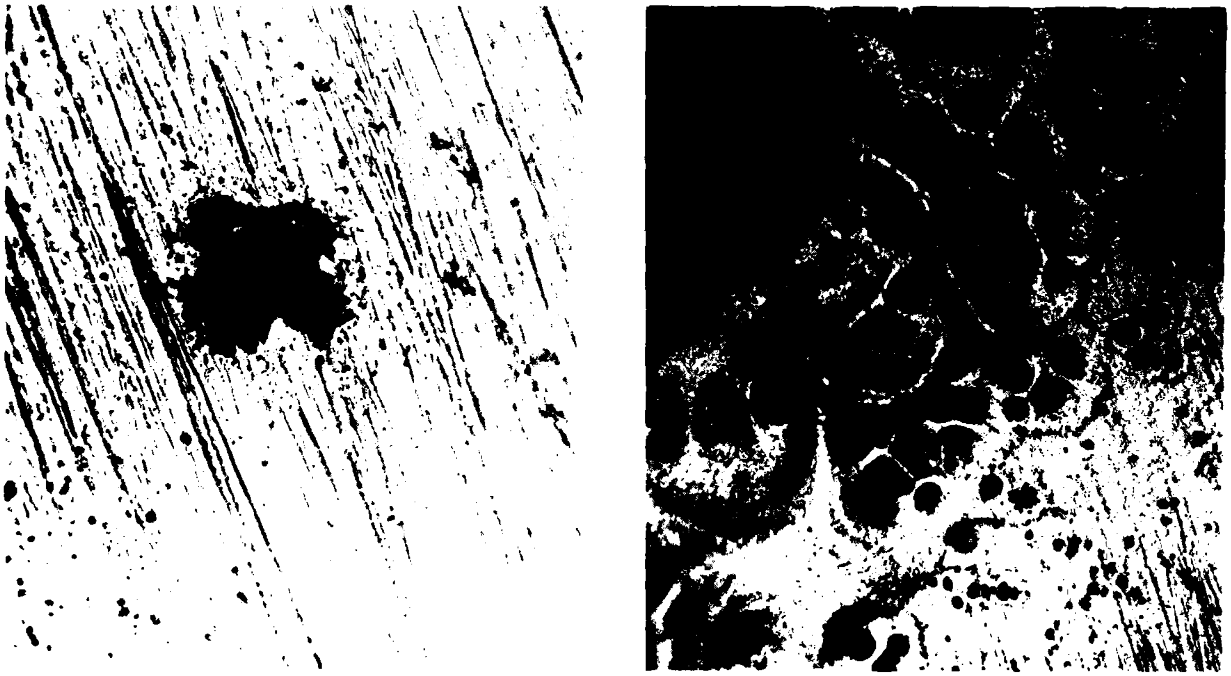

(c) Higher-magnification view of (b) (400×). (d) Edge of a melted area (160×).

Fig. 31. Preferential response of inclusions in AISI 4340 steel.

Fig. 32. Scanning electron micrographs of preferential response of inclusions in AISI 4340 steel.

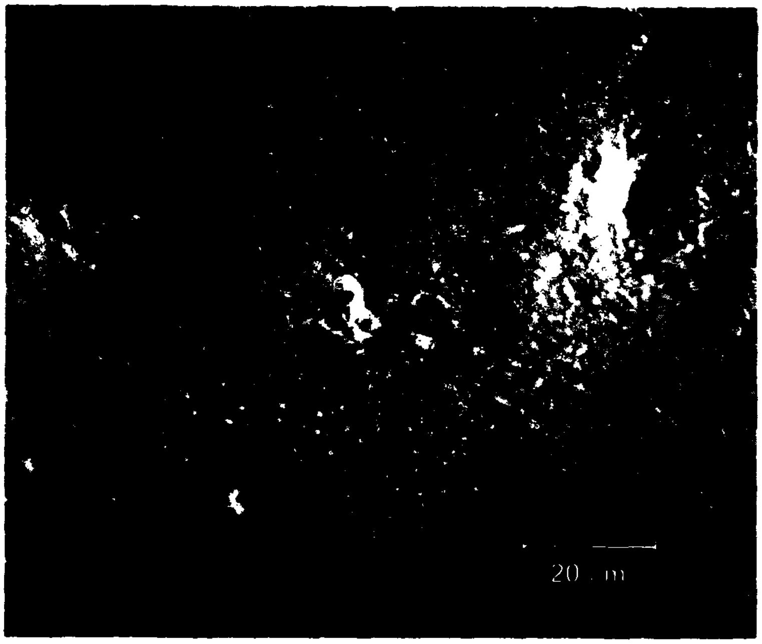

(a) 4340 50, 10% methane/argon, 150 psi, 40 J, 1 pulse.

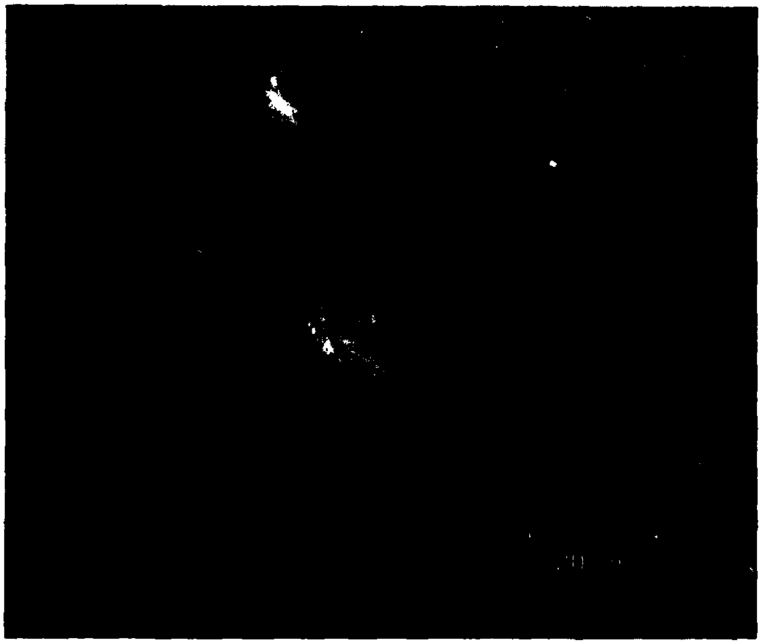

(b) 4340 43, 10% methane/argon, 150 psi, 40 J, 10 pulses.

Table 4. Results of experiments on the tungsten-coated AISI 4340 steel specimens.

Specimen No.	Tungsten thickness (μm)	Nickel thickness (μm)	Laser energy (J)	Evidence of cracking
W-13	244	9.5	41.2	Yes
W-10	231	6.5	41.4	Yes
W-12	212	3.0	42.1	Yes
W-27	224	10.0	32.0	Yes
W-11	226	6.5	32.2	Yes
W-16	208	2.0	32.4	Yes
W-26	224	12.0	22.0	Yes
W-14	220	7.0	20.6	Yes
W-18	200	2.5	21.4	Yes
W-25	220	10.0	12.8	No
W-15	220	6.5	12.8	Yes
W-20	214	3.0	12.7	Yes

The objective of these experiments was to determine if the thickness of the intermediate coating affected the formation of cracks in the tungsten overlay.

After the specimens had been laser-pulsed, the surface of each specimen was examined with an optical microscope for evidence of cracking. Metallographic sections were then taken through the center of the laser-pulsed region in each specimen normal to the coated surface. After polishing, the sections were etched in 2% Nital to delineate the coatings.

The results of the optical examinations are listed in Table 4. Cracks were observed in the tungsten coating of each specimen, except for the specimen with an intermediate nickel coating of 10 μm, which was pulsed at 10 J. The density of cracks appeared to decrease as the beam energy decreased. This was confirmed in the metallographic sections. Representative micrographs from each specimen are shown in Fig. 33, and the density of cracks does appear to decrease with the beam energy. However, a slight anomaly existed in the specimens pulsed at 10 J. The specimen with a 10-μm intermediate nickel coating showed no cracking, but the specimen with a 6-μm intermediate layer exhibited more cracking than the specimen with a 2-μm intermediate layer. This is demonstrated in Fig. 34, which compares micrographs from the metallographic sections of the three specimens with micrographs from the laser-affected regions of the specimens. As is evident in the surface structures, the surface of the specimen with the 6-μm intermediate nickel coating had not been sufficiently ground to remove the surface structure of the CVD tungsten coating. The rougher surface apparently increased the energy coupling between the specimen and the laser beam to produce the increased cracking. Thus, these results confirm the previous finding that increasing the thickness of the intermediate nickel coating does reduce the tendency of the tungsten overlay to crack, but the effect is relatively small.

Discussion

The major topics to be discussed in this section are

1. The use of SIMS for the microanalysis of interstitials.
2. SIMS and metallographic observations.
3. Position of the melt interface and depth of interstitial penetration.
4. Laser damage mechanisms.
5. Laser-induced surface structures.
6. Correlation of laser-induced surface chemistry reactions and damage mechanisms with erosion/corrosion mechanisms.

The Use of SIMS for the Microanalysis of Interstitials

At the outset of this study, some doubt existed about the most suitable technique for the microanalysis of interstitial elements in body-centered-cubic (bcc) metals, particularly in the ppm

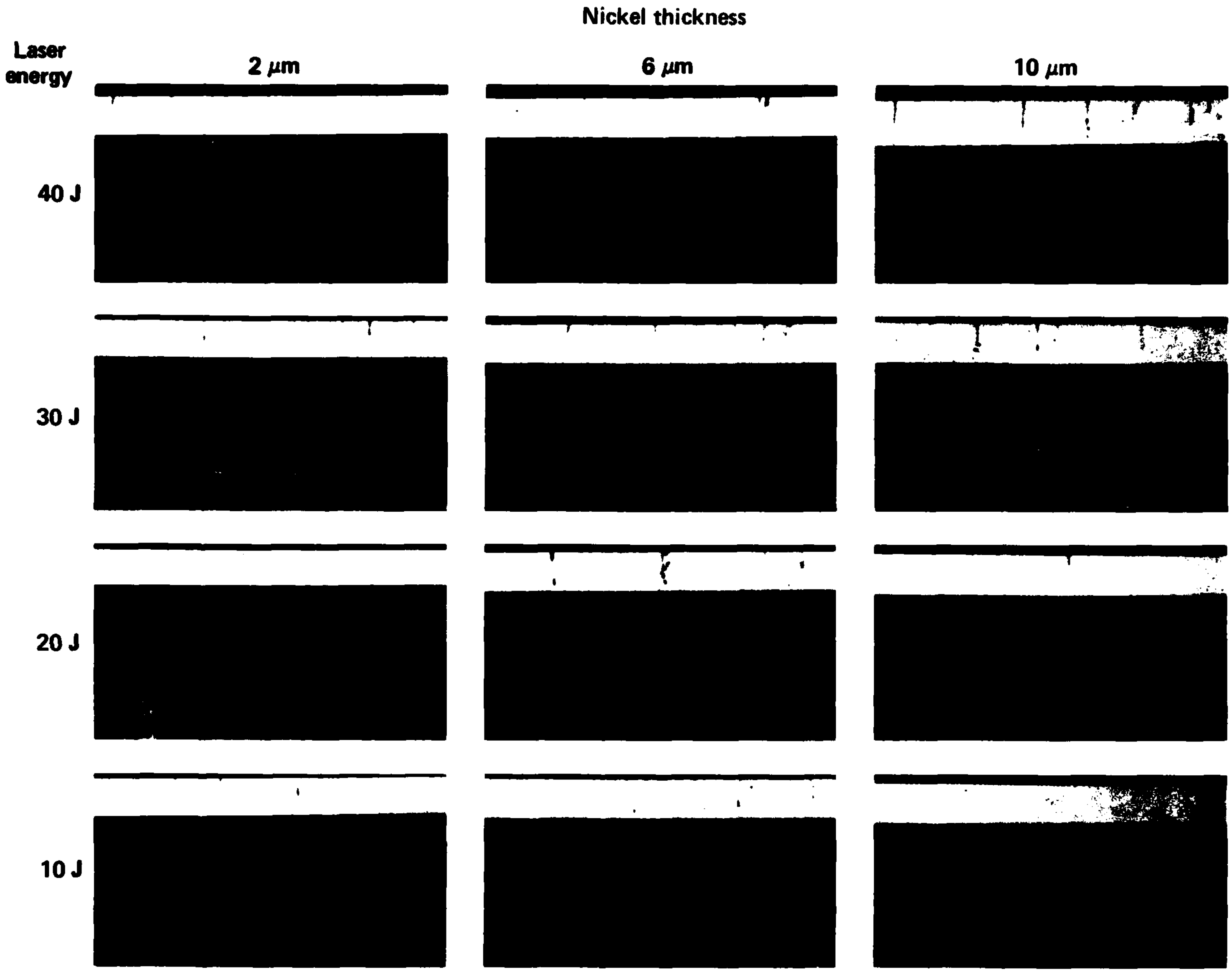

Fig. 33. CVD tungsten on AISI 4340 steel with different thicknesses of an intermediate coating of nickel; the nominal tungsten thickness is 250 μm.

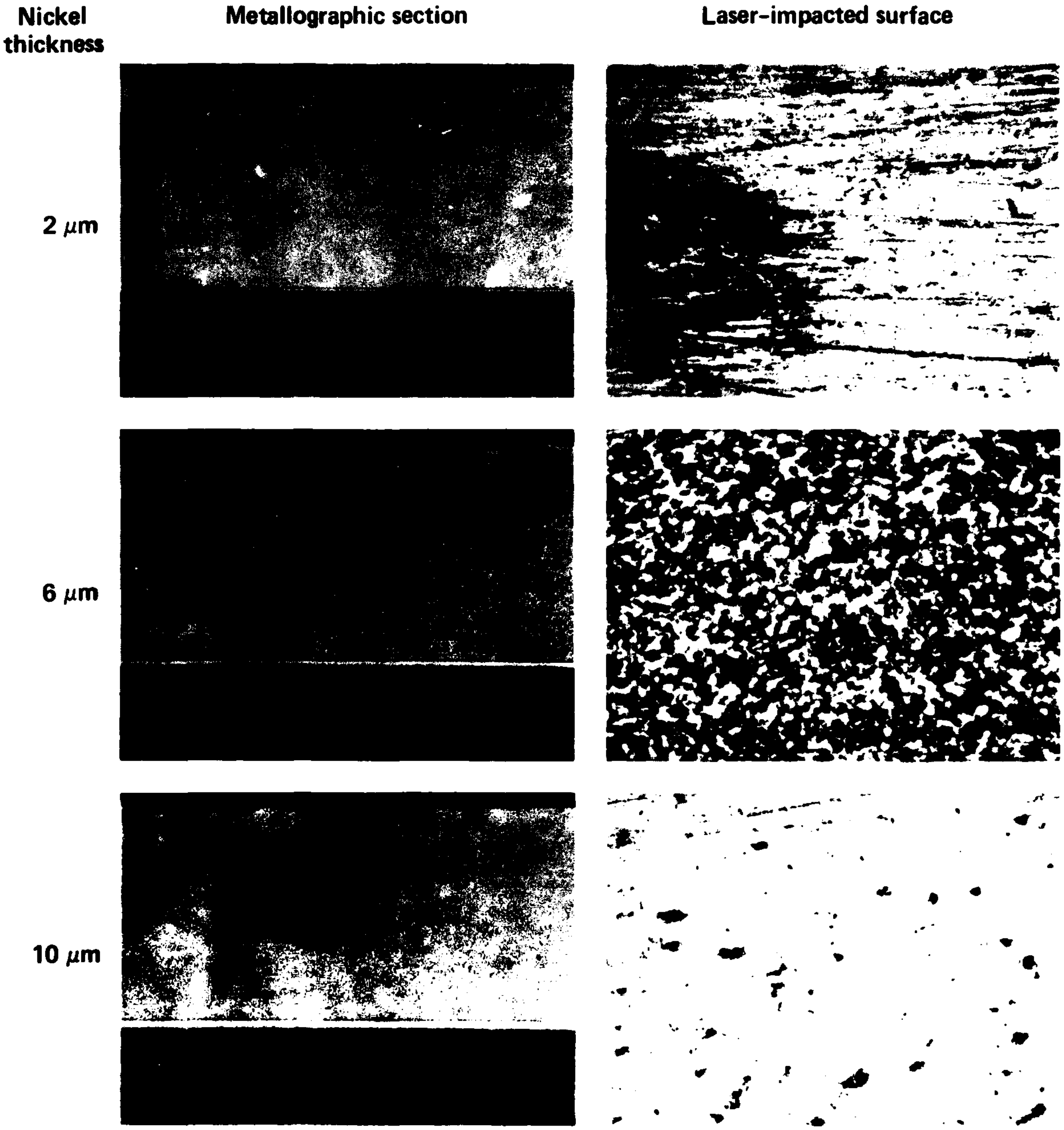

Fig. 34. Tungsten-coated AISI 4340 steel specimens pulsed 10 times with a 10-J laser beam.

range. SIMS was selected because of its exceptional sensitivity and the relatively high sputtering rates that could be achieved to generate depth-profile analyses. The results generated by this technique clearly demonstrate the viability of SIMS for this type of analysis.

Nitrogen is one of the most difficult elements to analyze by SIMS. The results from this study demonstrate that analysis of nitrogen can be conducted by analyzing for mass isotopes corresponding to molecular combinations of nitrogen with other elements. Combinations of nitrogen with both carbon and iron were used in this study. These combinations actually arise from recombination of the sputtered species and are not related to the manner in which the combined elements reside in the base material. Results from these molecular combinations are not totally unambiguous, however, because of interference from other molecular combinations. Consequently, detailed analyses of the interfering elements are required to assess the extent of interference and, as in this study, two or more molecular combinations should be used to verify that indicated compositional fluctuations are related to the appropriate element.

Precautions must be exercised in the interpretation of SIMS data, particularly with respect to the use of the molecular combinations of elements for the analysis of nitrogen. The use of iron in this program circumvented some of these problems. Additional work is required to establish calibration curves to convert intensities to concentrations. In spite of these reservations, the reproducibility of the results clearly demonstrates that the relative changes indicated in the concentration levels of the interstitial elements are real, and SIMS is sensitive to changes in the ppm range. Additional evidence of this sensitivity with regard to the detection of microsegregation of interstitials in cold-worked iron is discussed in Appendix 3. Thus, SIMS appears to be an extremely valuable analytical technique for the microanalysis of interstitial elements in bcc metals.

SIMS and Metallographic Observations

The SIMS depth profiles revealed that significant amounts of interstitial elements can diffuse into metal surfaces during laser-pulsing in reactive environments. However, interstitial diffusion did not occur in specimens pulsed below the threshold energy for surface melting to occur; it was observed only in conjunction with surface melting. Therefore, surface melting was a prerequisite for the diffusion of interstitials to occur. Similar findings were reported by Hoh *et al.*[6] for the diffusion of oxygen into silicon by laser-pulsing.

Good correlation existed between the depths of interstitial penetration determined by SIMS depth profiles and the damage layers revealed by optical metallography. This persisted in spite of the surface roughness of the SIMS craters generated by the primary ion beam. The depth profiles of the interstitial elements exhibited consistent patterns that reflected the sensitivity of specimen response to surface chemical reactions induced by laser-pulsing.

The SIMS results from the specimens pulsed in argon revealed that substantial amounts of oxygen and nitrogen diffused into the specimens, even though purified argon was used. In addition, the pressure chamber was purged several times before initiating the laser-pulsing, and the extent of contamination should have been minimal. The presence of both oxygen and nitrogen indicates that the major source of contamination probably was air. The amount of oxygen and nitrogen that accumulated in the specimens is considered to demonstrate the importance of surface chemical reactions within the relatively short time frame of a laser pulse. This sensitivity is further demonstrated by detection of the slight amount of decarburization that accompanied the oxidation reaction.

The concentration of an element is approximately proportional to the SIMS ion intensity. The ^{16}O ion intensities in Figs. 8b and 8d for Iron A and Iron B, respectively, are higher at the surface than the base level by a factor of approximately 20. Since the base level concentration was analyzed to be 33 ppm (0.0033 wt%), this indicates that the oxygen concentration is increased to about 0.06 wt% at the surface. The equilibrium solubility limit of oxygen in liquid iron increases from 0.16 wt% at 1550°C to 0.34 wt% at 1700°C.[7] However, the maximum solubility in solid solution has been reported to be only of the order of 0.002 wt% in alpha iron at 875°C,[8] and it may be substantially lower.[9] Consequently, the high surface concentration of oxygen in the specimens pulsed in argon and the smoothness of the profile in the surface affected region indicate that oxygen diffuses homogeneously into a molten surface layer, and the homogeneity is retained by the rapid cooling. Thus, a significant amount of oxygen can diffuse into the surface layer if it is molten, but it must be rapidly cooled to maintain a homogeneous distribution. This was verified by the absence of interstitial diffusion into specimens pulsed below the threshhold energy for surface melting.

The profiles for mass isotopes 26 and 70 in Figs. 8b and 8d show increases slightly less than those for the ^{16}O profiles. Although the correlation between concentration and ion intensity of a molecular combination of elements is not well established, the increase of the profiles by a factor of about 10 from base to surface compositions could indicate a surface composition of the order of 10 ppm. The maximum solubility of nitrogen in iron is of the order of 0.004 wt% in alpha iron at 873°C, 0.025 wt% in austenite at 1000°C, and 0.015 wt% in delta iron at 1470°C.[10,11,12] The solubility in liquid iron is only of the order of 0.045 wt%.[13] The low solubility of nitrogen in liquid iron may have limited the extent of laser-induced nitriding reactions. In addition, Grieveson and Turkdogan[11] have shown that the rate of solution of nitrogen in iron can be decreased by impurities such as water vapor. The difference in the ^{16}O profiles in Figs. 12a and 12b supports this possibility in the nitriding experiments.

Substantial amounts of carbon also diffused into molten surface layers when iron specimens were laser-pulsed in 10% methane/argon. Again, the carbon concentration could not be increased unless the energy threshold for surface melting to occur had been exceeded. As mentioned previously, the depth profile in Fig. 9d for Iron 55, which had received 50 pulses, indicated that a quasi-equilibrium surface concentration had been attained. In addition, the maximum ^{12}C ion intensity of most of the other iron specimens that had been pulsed in 10% methane/argon attained a similar level at the surface. SIMS analyses from the AISI 4340 steel specimens indicated that this quasi-equilibrium level was of the order of 0.4 wt%. Carbon has extensive solubility in liquid iron and austenite but limited solubility in delta and alpha iron.[14]

The extensive oxidation and limited carburization that occurred when Iron 59 was pulsed in carbon monoxide was not expected for solid-state reactions. However, for a constant gas composition, thermodynamic studies[15] have established that carbon monoxide can be net-carburizing at low temperatures and net-oxidizing at high temperatures. Since the increase in both carbon and oxygen occurs at high temperature in the liquid phase, the reaction should have been net-oxidizing. The fact that carburization occurred could be a consequence of the rapid decomposition of carbon monoxide on the surface of the specimen.

As has been emphasized, the analysis of nitrogen by the use of molecular combinations of elements is not unambiguous, but the results obtained in this work definitely appeared to be related to nitrogen. The experiments in nitrogen and ammonia verified that laser-pulsing could induce nitrogen to diffuse into melted surface layers, but the reactions did not appear to be as extensive as for the other gases. In fact, the experiments in argon indicated that more nitrogen could diffuse into melted surfaces as a result of air contamination than by laser-pulsing in nitrogen and ammonia. This could be related to the surface catalysis problem alluded to in the "Experimental Procedures" section.

These results demonstrate that substantial surface chemical reactions can occur during laser-pulsing when the energy threshold for surface melting is exceeded. The necessity for surface melting to have occurred was confirmed by the lack of interstitial diffusion in specimens pulsed below the threshold for surface melting. This correlates with the established practice of using high-melting-point nonreactive coatings to achieve resistance to erosion/corrosion. The subtle differences produced in the martensitic structures of the surface damage layers was further indication of the sensitivity of the surface chemical reactions to the environment. In fact, this conforms to theories that the alteration of surface microstructure by surface chemical reactions contributes significantly to erosion/corrosion mechanisms.[16]

Position of the Melt Interface and Depth of Interstitial Penetration

Attempts to determine the extent of melting that may have occurred during laser-pulsing presented an interesting predicament. Evidence of melting was not detected in the optical metallographic examinations of the cross sections, although both optical and SEM examinations of the surfaces did reveal definite evidence of surface melting. At first, the occurrence of recrystallization within the short time frame of the laser pulse was thought to be indicative of melting, but Speich and Fisher[17] have clearly shown that solid-state recrystallization does indeed occur in laser-pulsed Fe–3-1/4Si specimens. Therefore, the recrystallization that occurred in the iron specimens definitely appears to be a solid-state reaction arising from the cold-worked state of the substrate material. It is not an indication of melting.

Attempts to correlate the position of the melting interface with the occurrence of the martensitic zones also were not productive. Austenite reversion must occur before martensite can form in a bcc structure. As the carbon content of iron increases, the reversion initiates on heating at the A_{c1} temperature and is completed at the A_{c3} temperature, although these transformation temperatures may be shifted upward by the rapid temperature gradient induced by the laser pulse. Consequently, interfaces between the martensitic zones corresponding to the A_{c1}, A_{c3}, and melting temperatures should have been observed. Unfortunately, only two interfaces were detected in the AISI 4340 steel specimens, and the interface between the recrystallized layer and the martensitic layer in the iron specimens was not sharply defined. This broad interface in the iron specimens may have corresponded to the A_{c1}–A_{c3} zone, particularly since the carbon profile was relatively low in this region. However, the number of interfaces in the martensitic zones could not be used unambiguously to determine the position of the melting interface. Solid–liquid interfaces in welded steel structures usually are delineated with a debris layer of inclusions and precipitates. Therefore, evidence of the molten interface should have been apparent in the martensitic zone if extensive melting did occur, but no evidence of melting was found. Apparently, the rapid heating and cooling rates in the laser-pulsed specimens must have precluded this.

The positions of solid–liquid interfaces should have been evident in the SIMS ^{12}C depth profiles. Diffusion coefficients in molten material usually are at least a few orders of magnitude greater than bulk diffusion coefficients in the solid state. The increased diffusivity in the molten zone should result in a definite decrease in the ^{12}C profile between the molten and crystalline zones, although the molten interface does sweep in and out of the specimen during the heating and cooling cycles of the laser pulse. Examination of the ^{12}C profiles in the pure iron specimens indicates that this did not occur within the martensitic zones. In fact, the ^{12}C profiles appeared to decrease smoothly through the interface between the martensitic and recrystallized layers and well into the recrystallized layer, although this may be an artifact of redeposition contamination in the ion microanalyzer, as discussed previously. Contrary to previous arguments, this could imply that the entire martensitic layer was molten. Examination of diffusion penetration distances provides some insight to this problem.

The penetration distance of a diffusing species can be approximated by $2(Dt)^{1/2}$ where D is the diffusion coefficient at the diffusion temperature and t is the diffusion time. To simplify this approximation, a square-wave temperature profile will be assumed to persist for $t = 10^{-3}$ s with $T = 1500°C$. This is considered to be a strong overstatement of the actual conditions. The time is slightly longer than the 600-μs duration of the laser pulse, and the temperature is slightly higher than the peritectic temperature for the decomposition of austenite into delta ferrite and liquid iron. The diffusion coefficient for carbon in austenite at a pressure of one atmosphere is taken as $D = 0.15 \exp(-34000/RT)$ cm^2/s where R is the universal gas constant.[18] These values yield a penetration distance for carbon in austenite of 2.0 μm for one laser pulse and 6.3 μm for 10 laser pulses (the penetration distance scales as the square root of the number of pulses). This estimated penetration distance for 10 pulses is considerably less than the actual depths attained in Iron 43 and Iron 50, which were tested at 150 psi. Lazarus[19] has shown that the partial derivative of the diffusion coefficient with respect to pressure is proportional to the negative of the activation volume; the activation volume usually is positive, so an increase in pressure would decrease the penetration distance, but this effect is not very significant. Therefore, the depth of carbon penetration that occurred in the iron specimens does not appear to be related to solid-state diffusion.

Factors that could increase the depth of carburization in the solid state are plastic deformation caused by the pressure wave induced by the laser pulse and the dilatation strain imposed by the martensitic transformation. Wriedt *et al.*[20] have reported the enhancement of nitrogen solubility in shock-loaded iron, and Hirano *et al.*[21] observed a definite increase in the self-diffusivity of gold and silver due to concomitant plastic flow. An important contribution to this enhanced diffusion would be the production of an increased vacancy concentration during the laser pulse. Evidence of vacancy production by laser-pulsing and shock-loading has been described by Metz and Smidt[22] and Murr *et al.*[23,24] In addition, Clinard and Sherby[25] have shown that diffusion can be enhanced by a factor of two by repetitive martensitic transformations. However, these mechanisms would be expected to increase the penetration distances only by a factor of two or three and still do not appear to account for the total penetration distance.

Diffusion coefficients for molten metals usually are two to three orders of magnitude greater than for the metals in their crystalline state. If a diffusion coefficient of 10^{-3} cm^2/s is assumed for molten iron, the approximate penetration distance would be of the order of 20 μm for a single pulse and 60 μm for 10 pulses. This is within the range that occurred in this study, and it is consistent with the observation that surface melting was necessary for the inward diffusion of interstitials to occur. Even though these approximations appear to support the presence of a molten surface layer, they do not unambiguously resolve the question of whether or not a molten layer did form and, if so, the depth to which it may have penetrated.

Laser Damage Mechanisms

Previous laser studies on copper[26] revealed specific beam-energy thresholds existed for the various damage mechanisms to occur. No attempt was made in this study to determine the threshold energy levels, but a similar sequence of damage mechanisms was observed. In the iron specimens, the sequence from low to high energy levels was

1. Plastic deformation.
2. Recrystallization.
3. Recrystallization along with transformation to austenite and subsequent martensite formation during cooling.
4. Surface melting followed by formation of a fine-grained solidified structure on cooling and subsequent martensite formation.
5. Liquid-metal splattering and vaporization.

Vaporization and liquid-metal splattering is a major mechanism for the loss of material from surfaces exposed to high-energy laser beams. Furthermore, this could be an equally important mechanism in high-temperature erosion/corrsion environments, although this mechanism can be controlled by judicious material selection. Since the possibility existed, however, that operation of these mechanisms would remove the evidence of surface chemical reactions that was sought, the laser-pulsing experiments were conducted below the energy threshold for vaporization and liquid-metal splattering.

This sequence of damage mechanisms was slightly modified in the AISI 4340 steel specimens. The yield strength apparently was too high for detectable deformation to occur, and recrystallization did not occur. Thus, only mechanisms 3 and 4 were observed in the AISI 4340 steel specimens. Similar sequences are expected to occur in materials subjected to erosion/corrosion conditions. The difference in the behavior of the iron and AISI 4340 steel specimens demonstrates the important role of microstructure in specimen response, particularly below the energy threshold for surface melting.

In pulsed, high-temperature erosion/corrosion environments, the occurrence of these damage mechanisms would produce cyclic deformation of sufficient magnitude that the formation of fatigue cracks could result. In materials subject to martensitic transformations such as steels, the dilatation that occurs during transformation also would contribute to the cyclic deformation. Compositional changes caused by surface chemical reactions would accelerate these mechanisms and contribute to more rapid deterioration of the material.

The depth of the crater formed by laser-pulsing was considerably greater at 15 psi than it was at 150 psi. This conforms to previous studies of laser-induced crater formation by Rykalin *et al.*[27] As discussed previously, crater formation appears to occur by the extrusion of material from the central portion of the impact area. Therefore, one of the effects of increased gas pressure apparently is to mechanically resist the extrusion.

The preferential response of inclusions to laser-pulsing is another damage mechanism that is considered to be important in this study. As stated previously, this response undoubtedly is related to the optical properties of the inclusions, which would increase energy-coupling of the laser beam with them. However, it demonstrates the potential effect that low-melting inclusions could have.

The change of the reflectivity of metallic surfaces by repetitive laser pulses has been characterized by Ready.[28] The reflectivity of polished surfaces normally decreases, and this increases the energy adsorption of the specimen. However, energy adsorption remained essentially constant in the pressure-chamber experiments for all gases except air (Table 3). Specimens pulsed in air did show a substantial increase in energy absorption during the first few pulses before leveling off. An oxide film formed on these specimens, and this obviously was related to the gradual change in the surface optical properties as the film formed. The fact that increases in energy absorption did not occur with the other gases used in this study indicates that the contamination levels were sufficiently low to prevent film formation.

Laser-Induced Surface Structures

The formation of the fine globular structure on the surfaces of the melted regions appeared to be associated with the presence of carbon. It was present on the AISI 4340 steel specimens laser-pulsed in both 10% methane/argon, which was carburizing, and in argon, which was slightly oxidizing. Previous work indicated that it also formed on AISI 4340 steel specimens laser-pulsed in air. It did not form in pure iron specimens laser-pulsed in argon, carbon monoxide, nitrogen, or ammonia. Even though carbon monoxide is a carburizing gas under reducing conditions, the SIMS analysis revealed that substantial oxidation occurred with carburization in pure iron. The globular structure was present in pure iron specimens only after laser-pulsing in 10% methane/argon, and only after two to five pulses. This implies that the surface carbon content had to increase before the structure formed.

Similar globular structures have been observed on the surfaces of rapidly cooled metallic powder particles,[29,30] and the structures were related to dendritic solidification. Therefore, the globular structure definitely appears to have resulted from dendritic solidification. The interstices in the globular structure probably were formed by the interdendritic precipitation of carbon. Referring to the iron–carbon phase diagram,[14] the relatively small volume of the interstices indicates that they were associated with graphite rather than cementite. This interpretation is supported by the observation of Speich[31] that graphite forms on the surfaces of melted hypoeutectoid steels. The high oxygen content generated during laser-pulsing in carbon monoxide appears to have prevented the retention of graphite. The interstices of the globular structure appear to be voids in the SEM micrographs, and a slight amount of oxidation occurred in nearly all of the experiments. This implies that the graphite was removed by reacting with oxygen to form gaseous carbon monoxide. Furthermore, optical metallography indicated that the globular structure did not penetrate into the specimen but was restricted to the surface. This supports the contention that graphite formed only on the surface.

Correlation of Laser-Induced Surface Chemistry Reactions and Damage Mechanisms to Erosion/Corrosion Mechanisms

The successful culmination of this study ultimately will include meaningful mathematical treatments to simulate the damage mechanisms that operate during erosion/corrosion reactions. Such treatments must include the kinetics of chemical composition changes produced by surface chemical reactions. This normally involves the use of equilibrium reaction-rate constants for isothermal reactions, but equilibrium reaction-rate constants are not formally applicable to the highly transient types of reactions of interest in this study unless instantaneous reaction-rate data are available. An alternate treatment of the data, suggested in Appendix 1, involves formulation of an effective reaction-rate constant. The effective reaction-rate constant closely parallels the equilibrium reaction-rate constant, but it monitors net chemical composition changes on a pulse-by-pulse basis. Effective reaction-rate coefficients should provide reasonable estimates of the amounts of reactive elements that diffuse into a specimen during a single pulse. As suggested in Appendix 1, concentration gradients would be assumed to remain constant during an individual pulse, but the concentration gradient would be adjusted on a pulse-by-pulse basis through the effective reaction-rate constant. This concept would greatly simplify the mathematical modeling of erosion/corrosion reactions.

While material loss by vaporization and surface melting can be reduced in erosion/corrosion environments by proper design and material selection, the plastic deformation of the substrate material that accompanies these reactions is difficult to eliminate, particularly in highly transient pressure and flow environments. Accumulation of plastic deformation ultimately will lead to crack formation, and crack formation can be accelerated significantly in a reactive environment. At the outset of this program, we hoped to generate information on the extent to which surface chemical reactions affected plastic deformation. Unfortunately, work has not progressed to that point, and the effect of surface chemical reactions on the material parameters that control erosion/corrosion is difficult to assess. This issue is addressed in Appendix 5, which presents a simplified dislocation dynamics model for erosion/corrosion and discusses possible effects of surface chemical reactions on many of the material parameters involved.

Deep craters formed at low pressure in these experiments appeared to be enhanced by the extrusion of material by the stress waves generated by the laser pulse. The extruded material was deposited on the rim of the crater. This suggested that a similar effect could be of importance in erosion/corrosion mechanisms caused by a simultaneous pressure and thermal pulse. If the thermal pulse precedes the pressure pulse, molten material could be extruded slightly ahead of the pressure pulse in the pulse direction. If the pressure pulse precedes the thermal pulse, the molten material would be extruded in the back direction, and this probably would produce periodic asperities. These asperities could then be subjected to material removal by the next pressure pulse. Although this extrusion mechanism is speculative, it correlates with the frequently observed fact that erosion/corrosion rates are accelerated when surface melting occurs. This mechanism would be accelerated by the inward diffusion of surface reaction products such as carbon and nitrogen that lower the melting point.

Although the preferential response of inclusions in the laser-pulsing experiments may have occurred largely because of the optical properties of the inclusions, this nevertheless implicates the importance of inclusions in erosion/corrosion mechanisms. Inclusions represent a point of elastic/plastic incompatibility that can be magnified by differences in the thermal coefficients of expansion and diffusion between the inclusions and the base metal. This difference creates local stress concentrations that are conducive to crack formation. Consequently, inclusions can be an important source of crack initiation, particularly in pulsed erosion/corrosion environments.

These experiments also provided some information on the use of refractory coatings on materials to be used in pulsed, high-temperature erosion/corrosion environments. The experiments on the tungsten-coated steel specimens demonstrated the viability of the laser system for testing the mechanical stability of coatings. The observation that the products of surface chemical reactions did not penetrate significantly into the substrate unless surface melting occurred correlates with the use of refractory coatings to increase the melting point of the surface. If coatings are applied to substrates such as steel that are subject to solid-state transformations, the results of this study also indicate that the coating should be sufficiently thick to prevent the critical transformation temperatures from being reached in the substrate. This will eliminate the contribution of the dilatation strains associated with the transformation to the cyclic stresses on the coating, although a trade-off may be necessary since the brittleness of many refractory coatings increases with thickness.

Summary and Conclusions

The results generated in this study verify that gaseous erosion/corrosion surface reactions can be sustained in the laser pressure-chamber system and that specimen response is extremely sensitive to the environment. These results also demonstrate that reliable and consistent data can be generated with the laser pressure-chamber system.

Iron was an ideal modelling material for these experiments. The purity was sufficiently high to permit unambiguous detection of the various damage mechanisms that operated and microanalysis of the chemical composition changes that occurred.

SIMS ion microanalysis has excellent sensitivity for the detection of changes in the concentration of interstitial elements that result from laser-induced surface chemical reactions. Nitrogen is difficult to analyze by SIMS, but reliable information on nitrogen was obtained from the analyses of molecular combinations of nitrogen with other elements.

Surface chemical reactions induced by laser-pulsing resulted in the inward diffusion of interstitial elements, providing the energy threshold for surface melting was exceeded. Reactions involving carbon, nitrogen, and oxygen were detected, depending on the environment, and significant amounts of these elements diffused into the specimens even within the short time frame of the laser pulse. This demonstrated that specimen response was highly sensitive to the environment.

Laser-pulsing in argon resulted in significant increases in oxygen and nitrogen in the surface layers. This is suspected to arise from air contamination and perhaps some water contamination.

Laser-pulsing in 10% methane/argon resulted in a significant increase in carbon in the surface layer, along with minor and somewhat sporadic amounts of oxygen.

Laser-pulsing in carbon monoxide resulted in an unexpectedly high concentration of oxygen in the surface layer, and significantly less carbon than produced by 10% methane/argon.

Laser-pulsing in nitrogen and ammonia did yield higher nitrogen levels in the surface layers, but not nearly to the same extent as carbon in the carburizing gases. The nitrogen level appeared to be slightly higher in the specimen pulsed in nitrogen than in the specimen pulsed in ammonia.

Carbon did not appear to diffuse into the AISI 4340 steel specimens laser-pulsed in 10% methane/argon, although oxygen did. This indicated that the quasi-equilibrium level for 10% methane/argon in these experiments was of the order of 0.4 wt%.

In addition to the chemical composition changes, the sensitivity of specimen response to the environment during laser-pulsing also was reflected in subtle differences in both the surface structures and the subsurface martensitic structures.

The position of the interface between the melted surface layer and the substrate was difficult to detect.

The damage mechanisms observed to operate in the laser-pulsed specimens appeared to correlate reasonably well with damage mechanisms that are expected to operate in erosion/corrosion environments.

The sequence of damage mechanisms observed in iron specimens with increasing beam energy was (1) plastic deformation, (2) recrystallization, (3) recrystallization and transformation to austenite on heating and transformation to martensite on cooling, and (4) surface melting on heating, and formation of a fine-grained solidified structure and subsequent martensite formation on cooling. The beam energy was held below the threshold for liquid-metal splattering and vaporization.

The sequence of damage mechanisms observed in the AISI 4340 steel specimens was (1) transformation to austenite on heating and transformation to martensite on cooling, and (2) surface melting on heating, and formation of a fine-grained solidified structure and subsequent martensite formation on cooling.

The slightly different specimen response between iron and AISI 4340 steel specimens demonstrated the importance of the role of microstructure in specimen response, particularly below the energy threshold for surface melting.

The fraction of the beam energy absorbed by a specimen was surprisingly constant during a series of shots except for the samples tested in air (Iron 68 and Iron 69). The formation of an oxide film in the air tests caused a substantial increase in energy absorption during the first few shots before leveling off.

The laser system can produce useful data on the performance of candidate coating materials for erosion/corrosion applications. The results of this study confirm the previous finding that increasing the thickness of the intermediate nickel coating does reduce the tendency of the tungsten overlay to crack, but the effect is relatively small.

Acknowledgments

I gratefully acknowledge the many helpful and stimulating discussions with A. C. Buckingham during the course of these experiments. I am also grateful for the experimental assistance provided by R. H. Cornell and G. W. Carter in conducting the laser experiments, R. P. Kershaw in performing the metallography, J. R. Walton in performing the scanning electron microscopy, and many members of Charles Evans and Associates (San Mateo, CA), who performed the SIMS analyses and provided technical expertise in the interpretation of the results. The preparation of the tungsten-coated specimens by F. J. Huegel and E. B. Stiles is also gratefully acknowledged.

References

1. A. Goldberg and R. H. Cornell, *Pulsed-laser Heating--A Tool for Studying Degradation of Materials Subjected to Repeated High Temperature Excursions*, Lawrence Livermore National Laboratory, Livermore, CA, UCRL-53074 (1980).
2. *Metals Handbook*, Eighth Ed., Vol. 2 (Am. Soc. Metals, Metals Park, OH, 1964), p. 85.
3. E. Zinner, in *Scanning*, Vol. 3 (G. Witzstrock Publishing House, Inc., 1980), p. 57.
4. T. R. Anthony and H. E. Cline, *J. Appl. Phys.* **48**, 3888 (1977).
5. Ruth Chatterjee-Fischer, *Metall. Trans.* **9A**, 1553 (1978).
6. K. Hoh, H. Koyama, K. Uda, and Y. Miura, *Jap. J. Appl. Phys.* **19**, L375 (1980).
7. E. S. Tankins, N. A. Gokcen, and G. R. Belton, *Trans. Metall. Soc. AIME* **230**, 820 (1964).
8. A. U. Seybolt, *Trans. Metall. Soc. AIME* **215**, 298 (1959).
9. R. Sifferlen, *Compt. Rend.* **247**, 1608 (1958).
10. R. W. Fountain and J. Chipman, *Trans. Metall. Soc. AIME* **212**, 737 (1958).
11. P. Grieveson and E. T. Turkdogan, *Trans. Metall. Soc. AIME* **230**, 407 (1964).
12. P. Grieveson and E. T. Turkdogan, *Trans. Metall. Soc. AIME* **230**, 1604 (1964).
13. R. D. Pehlke and J. F. Elliot, *Trans. Metall. Soc. AIME* **218**, 1088 (1960).
14. M. Hansen, *Constitution of Binary Alloys* (McGraw-Hill, New York, 1958), p. 353.
15. *Metals Handbook*, Eighth Ed., Vol. 2 (Am. Soc. Metals, Metals Park, OH, 1964), p. 71.
16. I. Ahmad, in *High-Temperature Gas-Metal Reactions in Mixed Environments*, S. A. Jansson and Z. A. Foroulis, eds. (Gordon and Breach, 1973), p. 391.
17. G. R. Speich and R. M. Fisher, in *Recrystallization, Grain Growth and Textures* (Am. Soc. Metals, Metals Park, OH, 1966), p. 563.
18. I. I. Kovenski, *Fiz. Metal. i Metalloved* **16**, 613 (1963).
19. D. Lazarus, in *Diffusion in Body-Centered Cubic Metals* (Am. Soc. Metals, Metals Park, OH, 1965), p. 155.
20. H. A. Wriedt, R. J. Sober, and W. C. Leslie, *Metall. Trans.* **1**, 3351 (1970).
21. K. Hirano, M. Cohen, B. L. Averbach, and N. Ujiiye, *Trans. Metall. Soc. AIME* **227**, 950 (1963).
22. S. A. Metz and F. A. Smidt, Jr., *Appl. Phys. Lett.* **19**, 207 (1971).
23. L. E. Murr, O. T. Inal, and A. A. Morales, *Acta Metall.* **24**, 261 (1976).
24. O. T. Inal and L. E. Murr, *J. Appl. Phys.* **49**, 2427 (1978).
25. F. W. Clinard and O. D. Sherby, *Trans. Metall. Soc. AIME* **233**, 1975 (1965).
26. J. O. Porteus, D. L. Decker, J. L. Jernigan, W. N. Faith, and M. Bass, *IEEE J. Quantum Electronics* **QE-14**, 776 (1978).
27. N. N. Rykalin, A. A. Uglov, and M. M. Nizametdinov, *Sov. J. Quantum Electron.* **8**, 46 (1978).
28. J. F. Ready, *IEEE J. Quantum Electronics.* **QE-12**, 137 (1976).
29. R. M. German and J. E. Smugeresky, *Metall. Trans.* **9A**, 405 (1978).
30. M. A. Meyers, B. B. Gupta, and L. E. Murr, *J. Metals* **33**, 21 (Oct. 1981).
31. G. R. Speich, *Trans. Metall. Soc. AIME* **221**, 417 (1961).

CJT/jf

Appendix 1

Possible Gaseous Surface Chemical Reactions in Erosion/Corrosion

Introduction

Various types of gaseous surface chemical reactions that may occur in erosion/corrosion reactions are presented in this appendix. The primary gaseous products generated in many erosion/corrosion environments are CO, CO_2, H_2, H_2O, N_2, and NO_x. In reducing environments that would occur with O_2 depletion or incomplete combustion, carburizing and nitriding reactions probably would be the dominant surface reactions. Under certain temperature and pressure conditions, however, the environment can be net-oxidizing with oxidation being the dominant surface reaction. Impurities or minor constituents can significantly modify these surface chemical reactions. One of the more important minor constituents could be H_2S or related sulfur-bearing compounds. The presence of S in hot corrosion, even in trace amounts, can significantly increase corrosion rates and may form highly deleterious, low-melting-point compounds along the grain boundaries of the substrate. Although impurity effects were not included in this program, they definitely should be considered in future studies of this nature.

The reactions described in this appendix are generally equilibrium reactions. The kinetics of these reactions usually are determined in steady-state isothermal experiments, and reaction rate constants obtained from these experiments are rigorously applicable only under the restricted set of conditions that existed in the experiments. Both the thermal and the pressure pulses that occur in many erosion/corrosion environments are highly transient; therefore, the kinetics approach under equilibrium conditions is not rigorously applicable. At best, equilibrium reaction-rate data may serve as a useful first-order approximation to estimate instantaneous reaction rate kinetics. Since reaction rate kinetics are important in the quantitative analysis of erosion/corrosion data, a modified technique will be suggested that should be particularly applicable to mathematical modelling.

Carburizing Reactions

Carburizing reactions involve the decomposition of either gaseous or solid carbonaceous products in a reducing atmosphere. Some of the major carburizing reactions of interest in erosion/corrosion are

$$CH_4 \rightarrow \underline{C} + 2H_2 \tag{1}$$
$$2CO \rightarrow \underline{C} + CO_2 \tag{2}$$
$$CO + H_2 \rightarrow \underline{C} + H_2O \tag{3}$$
$$CO_2 + H_2 \rightarrow CO + H_2O \tag{4}$$

Reaction (4) is generally referred to as the water–gas reaction, and the CO produced by this reaction is considered to decompose by reaction (2). The reactants and products in these reactions are gaseous except for $\underline{C}$, which is underlined to indicate that it is in solution either in the molten or the solid substrate.

Nitriding Reactions

The most common gaseous reaction used in industrial nitriding involves the dissociation of NH_3. Other reactions of interest in erosion/corrosion involve the dissociation of N_2 and the reduction of gaseous NO_x:

$$NH_3 \rightarrow \underline{N} + 3/2\ H_2 \tag{5}$$
$$N_2 \rightarrow 2\underline{N} \tag{6}$$
$$NO_x + xH_2 \rightarrow \underline{N} + xH_2O \tag{7}$$
$$NO_x \rightarrow \underline{N} + x/2\ O_2 \tag{8}$$

As in the carburizing reactions, $\underline{N}$ indicates N in solution in either the molten or the solid substrate.

Oxidizing Reactions

Whereas the reactive atmoshpere in many erosion/corrosion environments may be net-reducing within one temperature range, the same atmosphere can be net-oxidizing in other temperature ranges. Therefore, oxidizing reactions also must be considered in erosion/corrosion reactions. These reactions can be quite complex if an oxide scale forms. Examples of typical reactions to be considered in erosion/corrosion are

$$O_2 \rightarrow 2\underline{O} \qquad (8)$$
$$CO \rightarrow \underline{C} + \underline{O} \qquad (9)$$
$$H_2O \rightarrow \underline{O} + H_2 \qquad (10)$$
$$Fe + H_2O \rightarrow FeO + H_2 \qquad (11)$$
$$3FeO + H_2O \rightarrow Fe_3O_4 + H_2 \qquad (12)$$
$$Fe + CO_2 \rightarrow FeO + CO \qquad (13)$$
$$FeO + CO_2 \rightarrow Fe_3O_4 + CO \qquad (14)$$

Again, $\underline{O}$ indicates O in solution. If O is introduced into solution by reactions (8) through (10), it could subsequently react with C and N in solution to form gases such as CO and NO_x. If such reactions do occur, they would lead to the formation of subsurface porosity, which would contribute to and possibly be a major factor in erosion/corroson mechanisms. Although such a reaction is hypothetical, it is mentioned here to demonstrate the high degree of complexity of erosion/corrosion reactions.

Many materials such as steel are susceptible to hydrogen embrittlement. H_2 gas can dissociate on the surface and be absorbed into the substrate. The dissociation is given by:

$$H_2 \rightarrow 2\underline{H} \qquad (15)$$

Sulfidizing Reactions

Sulfur-bearing gases such as H_2S and SO_2 can be extremely deleterious to many materials at elevated temperatures. Sulfur is known to cause hot shortness in steels, and sulfur-bearing gases can increase the rate of scale formation. The presence of SO_2 can promote the formation of both NiS and NiO in high-Ni steels and form an alligator surface. Such surfaces are observed in the early stages of gun-barrel erosion/corrosion. Reactions of interest are

$$H_2S \rightarrow H_2 + \underline{S} \qquad (16)$$
$$2SO_2 + 3Fe + 2Ni \rightarrow Fe_2O_3 + FeS + NiO + NiS \qquad (17)$$

Kinetics

Many of the reactions listed in this appendix have been studied extensively under equilibrium conditions, and equilibrium reaction-rate constants have been determined for a wide range of conditions. As mentioned in the introduction, these equilibrium reaction-rate constants are not formally applicable to the highly transient response that occurs in erosion/corrosion reactions. Therefore, an alternate treatment is required, particularly for the ultimate goal of modelling erosion/corrosion reactions. The most obvious approach is to develop an effective reaction-rate constant that relates the amount of reactant injected into a specimen to the energy released during the erosion/corrosion event (the laser-pulse energy in these experiments), the duration of the pulse, and the partial pressures of the reacting gases.

For a first approximation in mathematical modelling, instantaneous reaction rates could be ignored, and the effective reaction-rate constant could be related to the amount of reactant accumulated in the substrate during a single pulse. In a treatment such as is outlined in Appendix 5, the composition gradients would be held constant during the computer simulation of a single pulse, and the composition gradient would be adjusted through use of the effective reaction-rate constant prior to the next pulse simulation. This will be a reasonable approximation if the amount of reaction products injected into a substrate during a single pulse is small. This should be the case for most erosion/corrosion reactions.

Appendix 2
Engineering Safety Evaluation of the Pressure-Chamber System

LAWRENCE LIVERMORE LABORATORY - UNIVERSITY OF CALIFORNIA **ENGINEERING NOTE**		FILE NO. ENS 79-968	PAGE 1
SUBJECT ADDENDUM TO MECHANICAL ENGINEERING SAFETY NOTE		NAME D. I. Chambers	
5-PORTED VESSEL		DATE Feb. 18, 1982	

ADDENDUM TO ENS79-968

5-PORTED VESSEL

Prepared by: Diane I. Chambers
Diane I. Chambers
Responsible Individual
Engineering Sciences Division

Checked by: James C. Swingle
James C. Swingle, Section Leader
Authorized Individual
Engineering Sciences Division

Reviewed by: Roger W. Werne
Roger W. Werne, Division Leader
Engineering Sciences Division

Distribution:

A. Buckingham
G. Carter
D. Chambers
C. Price
R. Sherry
J. Swingle
R. Trusty
R. Werne/J. Mahler
ME Library

MAWP = maximum allowable working pressure

MOP = maximum operating pressure

MESM = Mechanical Engineering Safety Manual

LAWRENCE LIVERMORE LABORATORY · UNIVERSITY OF CALIFORNIA **ENGINEERING NOTE**		FILE NO. ENS 79-968	PAGE 2
SUBJECT ADDENDUM TO MECHANICAL ENGINEERING SAFETY NOTE		NAME D. I. Chambers	
5-PORTED VESSEL		DATE Feb. 18, 1982	

A. DESCRIPTION

This safety note addresses the modification of the 5-ported pressure vessel assembly in B131, Room 1441, used to study the mechanisms of gun barrel erosion. The vessel itself remains unchanged (Dwg. 70-105078-00) but in place of the sapphire window at the lower port (indicated in Figure 1) a tube extension (Figure 2) will be added, through which a sample on a long attenuation rod will be inserted. The vessel end of the extension has an O-ring seal; the far end is sealed with a Conax fitting TG20B4V rated for 10 ksi (69 Mpa). The MAWP and MOP of the assembly will remain at 2500 psi (17.2 MPa) and 2000 psi (13.8 MPa) respectively as described in ENS 79-968. The gases to be used have been narrowed down to argon, carbon dioxide, carbon monoxide and moist air; nitrogen and oxygen have been eliminated; argon with 1% methane has been substituted for methane. All gases (except moist air) will be dispensed from size N gas cylinders (13 ft^3 (.368 m^3) at S.T.P.). A 100 Joule laser with a 1 ms pulse length replaces the 15 Joule laser with a 40 ns pulse length. The effect of this laser change on the sapphire window is examined and its safeness verified should the assembly ever revert back to its original configuration. The responsible operating persons are Bob Trusty and Gary Carter of Mechanical Engineering for Cliff Price and Al Buckingham of Chemistry.

B. HAZARDS

The hazards remain the same as cited in ENS 79-968, those hazards associated with high pressure gases, chemical reactivity and toxicity, and high power lasers.

The tube extension, since it is occupied by the attenuation rod during pressurization, contributes very little extra volume to the system and so the energy content of the compressed gas remains as calculated in ENS 79-968

$$U = .55 \text{ g TNT}$$

C. CALCULATIONS

Tube Extension Wall Strength

The strength of the tube extension must be examined. The thinnest wall section occurs at the O-ring seat where

d_o = 1.25 in
d_i = .9375
d_o/d_i = 1.33 ⟶ thick walled vessel

The MAWP is given by the MESM as

$$\text{MAWP} = \frac{\sigma_u}{SF}\left[\frac{d_o^2 - d_i^2}{d_o^2 + d_i^2}\right]$$

For a safety factor of 4 and σ_u = 85 ksi for 304 stainless steel.

$$\text{MAWP} = 5.95 \text{ ksi } (41 \text{ MPa})$$

The length of thread engagement of the tube extension exceeds that of the port nut previously used hence yielding of these threads is very unlikely.

SUBJECT ADDENDUM TO MECHANICAL ENGINEERING SAFETY NOTE
5-PORTED VESSEL

NAME D. I. Chambers
DATE Feb. 18, 1982

Laser Effect on Sapphire Window

A 100 J laser with a 1.06 μm wavelength has replaced the 15 J laser and pulse duration τ has been increased from 40 ns to the range between 600 μs and 1 ms. The 100 J laser will be operated at a maximum energy of 50 J and in general the beam will be collimated to some lower energy level before being focused down to a minimum spot size of .375 in (.95 cm) diameter. For the uncollimated beam (worst case) an effluence (energy per unit beam area) E and flux (power per unit beam area) F can be calculated and compared to the previous operation mode of the 15 J laser.

15 J Laser Mode:

$E_1 = 15$ J

$A_1 = \frac{\pi}{4}(.75\text{in})^2 = .44\text{in}^2\ (2.85\text{cm}^2)$

$\tau_1 = 40$ ns

$E_1 = \frac{E_1}{A_1} = 5.3\ \text{J/cm}^2$

$F_1 = \frac{E_1}{\tau_1} = 1.3 \times 10^8\ \text{W/cm}^2$

100 J Laser Mode:

$E_2 = 50$ J

$A_2 = \frac{\pi}{4}(.375\text{in})^2 = .11\text{in}^2(.71\ \text{cm}^2)$

$T_2 = 600\ \mu\text{s} - 1\ \text{ms}$

$E_2 = \frac{E_2}{A_2} = 70\ \text{J/cm}^2$

$F_2 = \frac{E_2}{\tau_2} = 1.2 \times 10^5 - 7.0\text{x}10^4\text{W/cm}^2$

A comparison of modes of operation shows that with the 100 J laser the flux drops significantly (due mainly to the lengthened pulse) but the effluence rises an order of magnitude. Unfortunately, in the long pulse regime failure mechanism are energy rather than power dependent. Data are unavailable for damage thresholds, E_{max}, for pulses as long as 600 μs - 1 ms; however, the literature tends to agree that this threshold scales with $\sqrt{\tau}$ in the 0-1 μsec regime.* Information in the 600 μs to 1 ms range must be extrapolated.

---

*Information from David Milam, "Y" Division, Feb. 23, 1982.

The effluence with the 15 J laser mode will be used as the damage threshold baseline for this scaling. (This assumption is conservative since no damage was found in the windows after having been subjected to 5.3 J/cm^2)

$$\frac{E_{max} @ 600\ \mu sec}{E_{max} @ 40\ ns} = \sqrt{\frac{\tau_2}{\tau_1}} = \sqrt{\frac{600 \times 10^{-6}}{40 \times 10^{-9}}} = 122$$

$$E_{max} @ 600\ \mu sec = 650\ J/cm^2$$

$$\frac{E_{max} @ 1\ ms}{E_{max} @ 40\ ns} = \sqrt{\frac{\tau_2}{\tau_1}} = \sqrt{\frac{1 \times 10^{-3}}{40 \times 10^{-9}}} = 158$$

$$E_{max} @ 1\ ms = 840\ J/cm^2$$

This 650-840 J/cm^2 damage threshold is 9.3 to 12 times the 70 J/cm^2 effluence anticipated in the 100 J laser operation mode. This factor can not, however, justifiably be called a "safety factor". The scaling $E_{max} \sim \sqrt{\tau}$ has only been verified in the regime 0-1 μsec. The presence of a 2000 psi (13.8 MPa) MOP further complicates the dubious calculation of a "safety factor".

To compensate for these uncertainties the stainless steel blast tube described in ENS 79-968 will remain installed between the laser optics and the sapphire window to protect from any generated chips. A catastrophic failure is unlikely <u>UNLESS</u> the laser beam is actually focused ON the window itself. A checkout of the optics as described in the associated Operational Safety Procedure (OSP) must be completed after each new set up to avoid this hazardous situation. The procedure of inspecting the window before each day of use will continue. The window will also be allowed to cool completely before each shot.

D. PRESSURE TESTING

The test chamber inlet manifold, tube extension and Conax fitting shall be tested as a single unit. The assembly shall be "bagged" with a helium leak detector and pressure tested with helium gas to 150% MAWP, 3750 psi (26 MPa). At all times during pressure testing care will be taken to maintain the oxygen compatible cleanliness of the assembly. The testing will be done under the supervision of authorized B343 personnel.

E. LABELING

The LLNL Pressure Inspector will certify the vessel by attaching a "LLNL Pressure Tested" label with the following information:

Assembly AAA70-105012-00
Safety Note ENS 79-968 + Addendum
MAWP 17.3 MPa (2500 psi)
Fluid: Air, CO, CO_2, CH_4, Ar
Temperature: -20° to 100°C
Remark: Manned Area

F. ASSOCIATED PROCEDURES

Operational Safety Procedure

LAWRENCE LIVERMORE LABORATORY - UNIVERSITY OF CALIFORNIA

ENGINEERING NOTE

FILE NO.	ENS 79-968
PAGE	7
SUBJECT	ADDENDUM TO MECHANICAL ENGINEERING SAFETY NOTE 5-PORTED VESSEL
NAME	D. I. Chambers
DATE	Feb. 18, 1982

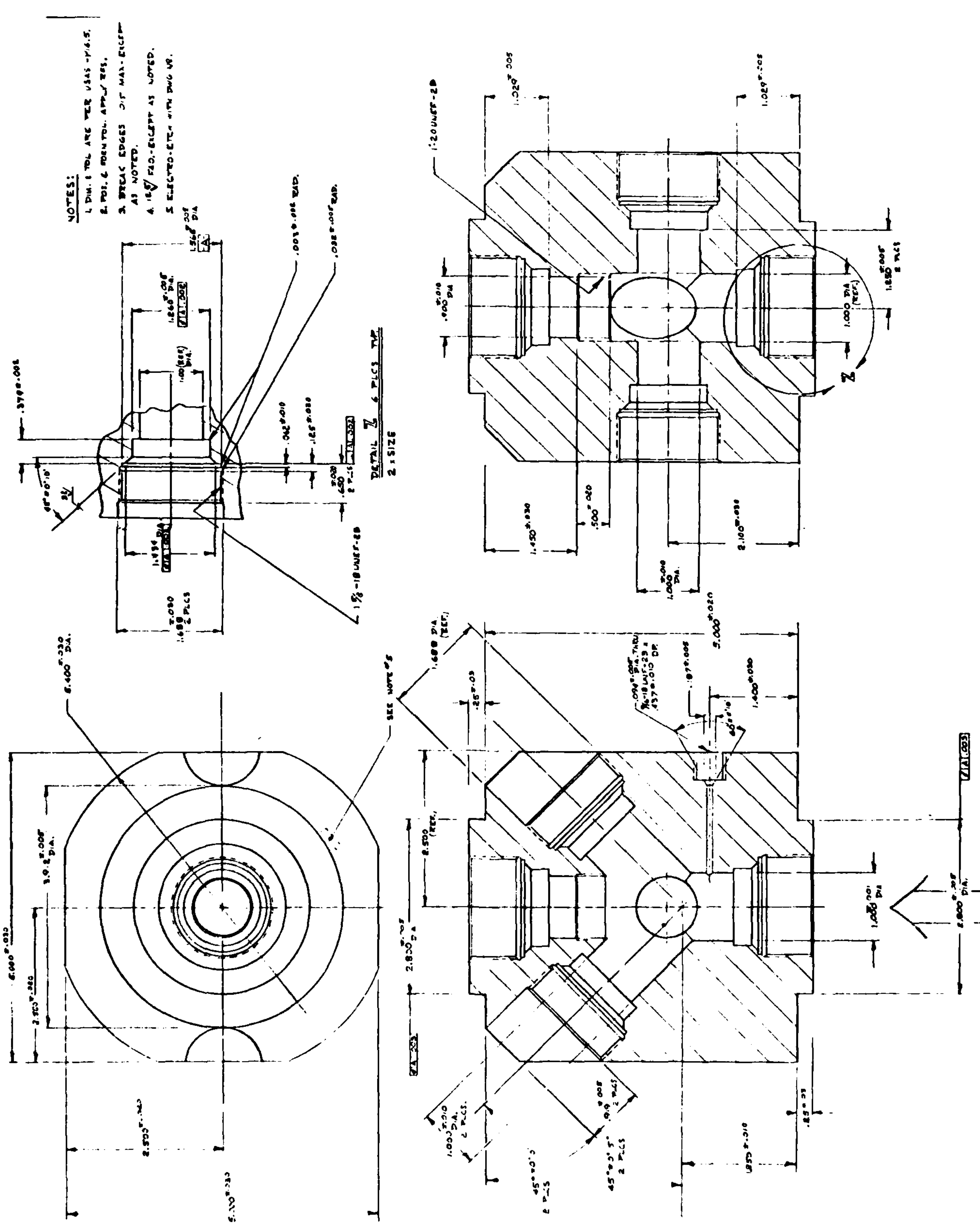

Figure 1

RL-39H (Rev.4/67)

LAWRENCE LIVERMORE LABORATORY · UNIVERSITY OF CALIFORNIA **ENGINEERING NOTE**		FILE NO. ENS 79-968	PAGE 8
SUBJECT ADDENDUM TO MECHANICAL ENGINEERING SAFETY NOTE		NAME D. I. Chambers	
5-PORTED VESSEL		DATE Feb. 18, 1982	

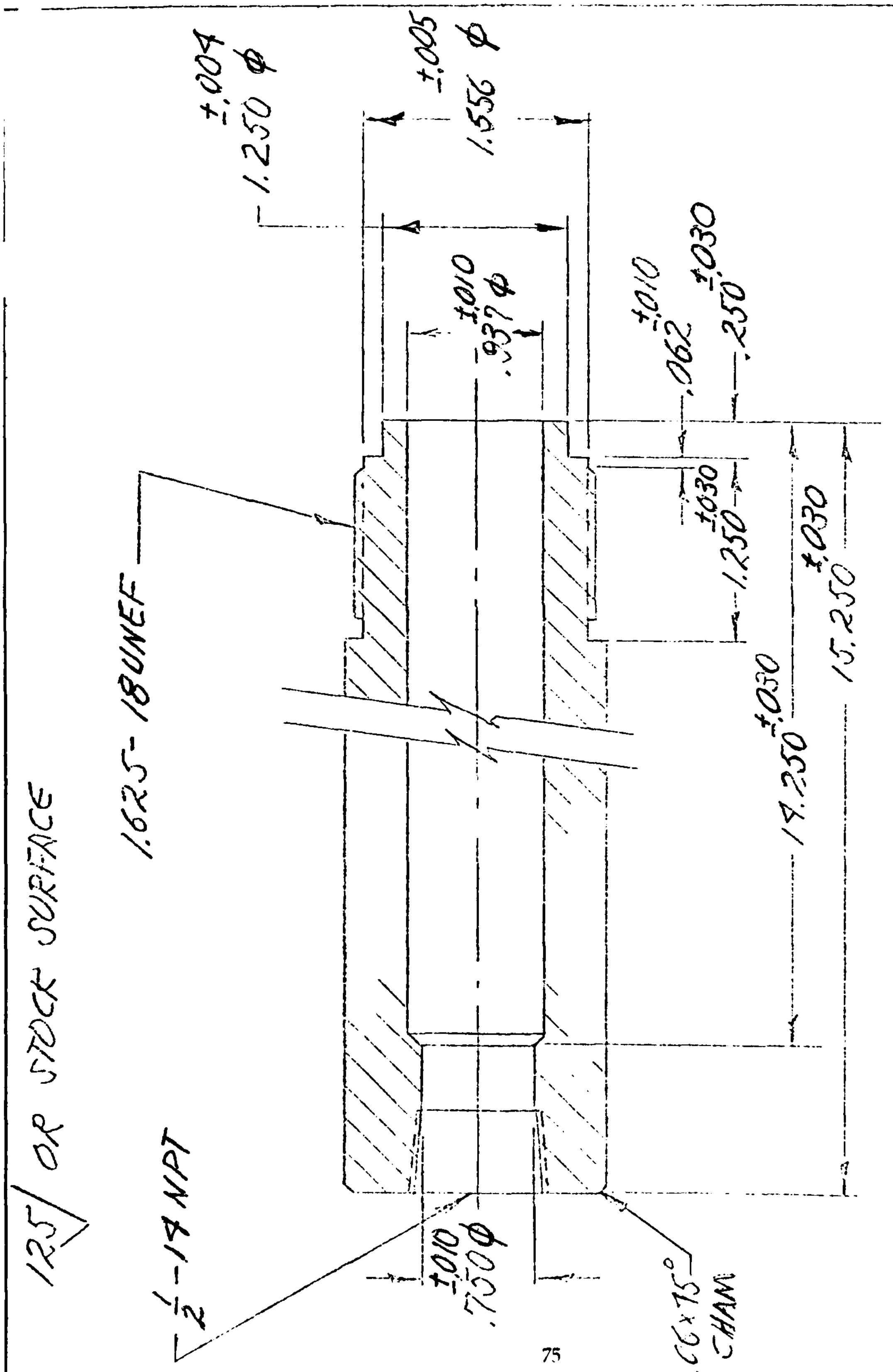

Figure 2

MAT'L: CRES 304

Appendix 3
Evidence of Interstitial Microsegregation in Iron, Obtained by Ion Microscopy

Introduction

Segregation of impurity atoms to the strain fields of dislocations and the effective locking of the dislocations by the impurity "atmospheres" was first suggested by Cottrell[1] and Nabarro.[2] The formation of interstitial atmospheres and their effect in iron was first treated by Cottrell and Bilby.[3] Further importance of interstitial effects and experimental evidence demonstrating the effects have been reviewed by Hirth and Lothe.[4] This paper describes additional evidence of microsegregation of several interstitial elements in iron that has been detected using secondary ion mass spectroscopy (SIMS).

Experimental Procedure

The iron specimens used in this study had been exposed to a pulsed laser beam in different gases. The purity of the iron was nominally 99.96%. The carbon and oxygen contents were 18 and 33 ppm, respectively, and both the nitrogen and the hydrogen contents were reported to be less than 1 ppm. These concentrations were sufficiently low to facilitate the detection of small changes in the concentrations of these elements induced by laser-pulsing, but they were still sufficiently high to be easily analyzed by SIMS. The specimens were sectioned from a 1/2-in.-diameter bar and were approximately 1/8-in. thick. The bar had been cold-swaged, and the microstructure was composed of severely elongated grains. The cold-worked structure provided the necessary dislocation structure for the occurrence of microsegregation. The surface of each specimen was metallographically polished prior to laser-pulsing. This enhanced detection of surface damage and also provided a more uniform surface for SIMS analysis. The directions of the laser-pulsing and the SIMS profiles were parallel to the axis of the bar.

The specimens were pulsed with a two-stage neodymium-glass laser capable of generating a pulse of up to 100 J in the normal mode; the pulse duration was 600 μs, and the initial beam diameter was 19 mm. An aperture and lens were used to focus the beam to 3.2-mm diameter on the specimen surface. The specimens were pulsed in a pressure chamber filled with argon and a 10% methane/argon mixture at 150 psi.

SIMS depth-profile analyses were performed with a CAMECA IMS-3f ion microanalyzer using a Cs^+ primary ion beam. The Cs^+ ion beam yields high sensitivity for elements with high electron affinities. This is particularly desirable for the analysis of electropositive elements, including hydrogen, carbon, oxygen, and silicon. Nitrogen has both a very low electron affinity and a high ionization potential and is one of the more difficult elements to analyze with SIMS. Nitrogen information was obtained by analyzing for molecular combinations of nitrogen with carbon and iron. Mass isotopes 26 ($^{12}C + ^{14}N$) and 70 ($^{56}Fe + ^{14}N$) were used. Some caution had to be exercised in the interpretation of the mass isotope 26 and 70 data, however, because of interference with other molecular combinations (e.g., $^{10}B + ^{16}O$, $^{12}C_2 + ^{1}H_2$, $^{54}Fe + ^{16}O$, and $^{58}Fe + ^{12}C$). The depth profiles were conducted with high sputtering rates of the order of 0.05 μm/s. The diameter of the area analyzed was estimated to be 2 to 3 μm.

Results and Discussion

The specimens were analyzed for mass isotopes ^{1}H, ^{12}C, ^{16}O, $^{26}[CN]$, ^{28}Si, ^{34}S, ^{56}Fe, and $^{70}[FeN]$. In addition, mass isotope ^{11}B was analyzed in some of the specimens. Up to nine elements could be analyzed sequentially at each step in the profile. The depth concentration profiles were normalized to ^{56}Fe equivalence. This was an attempt to compensate for irregularities in the profiles caused by factors such as the depths of the craters formed by the primary ion beam and surface irregularities caused by laser-beam-induced melting. It was effected by arbitrarily plotting the ^{56}Fe data along a straight line at a fixed intensity level and proportionally adjusting the other intensity data by the relative amount required to shift the ^{56}Fe data. This is only an approximate correction, however, since the relative ion extraction efficiencies also can be affected by concentration changes.

Depth profiles from a specimen laser-pulsed in argon at 150 psi with a beam energy of 10 J are shown in Fig. A3-1. Fig. A3-1a is from the unexposed region, and Fig. A3-1b is from the laser-pulsed region.

Surface melting had occurred in the region Fig. A3-1b was taken from, and the depth profile extended through the melted zone.

The point of major concern in this paper is the short-range intensity fluctuations in the ^{12}C and ^{16}O profiles in Figs. A3-1a and A3-1b. The sampling points in the depth profiles were at approximately 2-μm intervals, and the periodicity of the intensity fluctuations was approximately 4 μm. This indicates that the segregation patterns are of the order of a few micrometers, and this corresponds with the size of the dislocation cell structure found in cold-worked iron.[5-8]

The intensity fluctuations were much greater than the instrument noise level and were consistently observed in the base material of the cold-worked iron. Corresponding intensity fluctuations also occurred in the mass isotope 26 and 70 profiles. As can be seen in Fig. A3-1b, these fluctuations disappeared in the laser-pulsed regions whenever surface melting occurred. This obviously was related to the rapid quenching of the surface region after exposure to the laser beam. Thus, the intensity fluctuations were real and related to the cold-worked structure. Furthermore, their absence provided an indication of the depth to which carbon and oxygen were homogeneously redistributed into solution by surface melting.

Depth profiles from specimens laser-pulsed in 10% methane/argon at 150 psi with a nominal beam energy of 40 J are shown in Fig. A3-2. Fig. A3-2a is from a specimen which received 10 pulses, and Fig A3-2b is from a specimen which received 50 pulses. These figures show the reproducibility of the intensity fluctuations in the ^{12}C, ^{16}O, $^{26}[CN]$, and $^{70}[FeN]$ profiles in the base material. Similar fluctuations also are evident in the ^{11}B profile in Fig. A3-2a. The intensity of the ^{11}B profile is sufficiently low that the contribution of instrument background has become apparent, particularly in the portion of the profile corresponding to surface melting. This is further verification that the intensity fluctuations in the other profiles are real, since the other profiles are significantly higher than the background level.

Other observations made from the profiles are discussed briefly to demonstrate the excellent sensitivity of SIMS in the analyses of these elements. Comparison of Figs. A3-1a and A3-1b shows that laser-pulsing in argon significantly increased the oxygen concentration when surface melting occurred. The depth of oxygen penetration indicated in Fig. A3-1b was about 20 μm. Fig. A3-1b also shows that the oxidation was accompanied by a slight amount of decarburization. The profiles for mass isotopes 26 and 70 in Fig. A3-1b show increases near the surface nearly identical to the ^{16}O profile. This implies that nitrogen contamination also occurred, and that the source of contamination was probably air. The ^{1}H profiles in this specimen did not appear to be affected by laser-pulsing. In addition, the intensity fluctuations were almost nonexistent in the ^{1}H profile.

Figs. A3-2a and A3-2b, for specimens pulsed in 10% methane/argon, demonstrate that significant increases did occur in the carbon content as the number of pulses increased. Comparison with depth profiles from AISI 4340 specimens indicated that the maximum carbon level reached in these figures was approximately 0.40%. The flat ^{12}C profile projecting from the surface of the specimen pulsed 50 times in Fig. A3-2b indicates that saturation occurred, and this could correspond to a quasi-equilibrium value for these specific conditions. The ^{1}H profiles also appeared to increase slightly near the surfaces, probably the result of residual water contamination, but this did not consistently correspond to the increase in the ^{16}O profiles.

The intensity fluctuations in the carbon, oxygen, nitrogen, and boron profiles are considered to be evidence of microsegregation. The fluctuations in the ^{16}O, $^{26}[CN]$, and $^{70}[FeN]$ profiles almost exactly coincide, and the fluctuations in the ^{11}B profile also show a strong tendency to coincide with them. The ^{28}Si profiles also show very slight fluctuations that coincide with them, but these are suspected to be related to $^{12}C + {}^{16}O$ and not to ^{28}Si. In contrast, the fluctuations in the ^{12}C profiles have a different and apparently unrelated pattern. This strongly suggests that oxygen, nitrogen, and boron segregate to a common site, and carbon is segregating to a different site. The intensity fluctuations are significantly greater for oxygen, nitrogen, and boron than they are for carbon. This could indicate that oxygen, nitrogen, and boron form clusters or fine precipitates, whereas carbon segregates in a more uniform configuration such as Cottrell atmospheres along dislocations in cell walls.

Surprisingly, the hydrogen profiles did not exhibit evidence of segregation. Whether this is related to the rapid diffusion of hydrogen during the analysis, insensitivity of SIMS to detect hydrogen segregation because of a high hydrogen background, or the lack of hydrogen segregation requires further study.

Obviously, additional work is required to positively identify the sites for interstitial segregation, but these results demonstrate the potential for SIMS microanalysis to detect interstitial segregation.

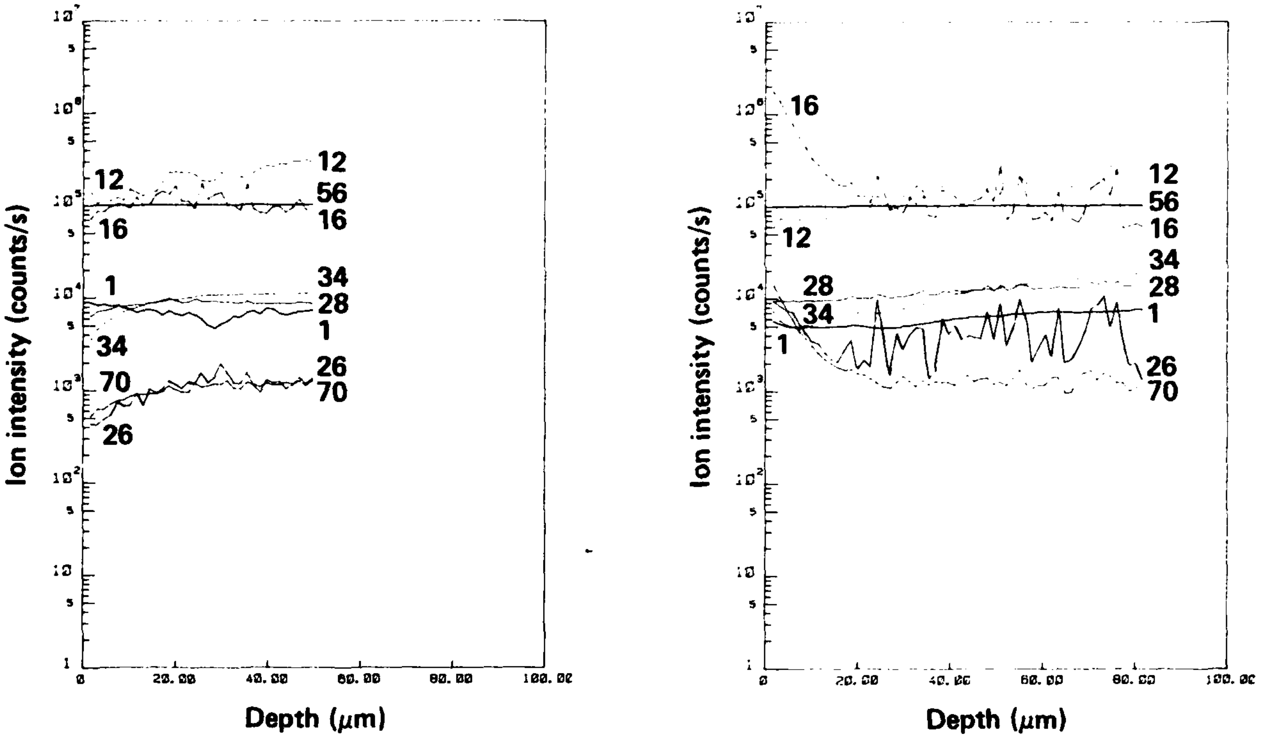

(a) Unexposed area.

(b) Laser-pulsed region.

Fig. A3-1. SIMS depth profiles from a specimen laser-pulsed in argon at 10 J.

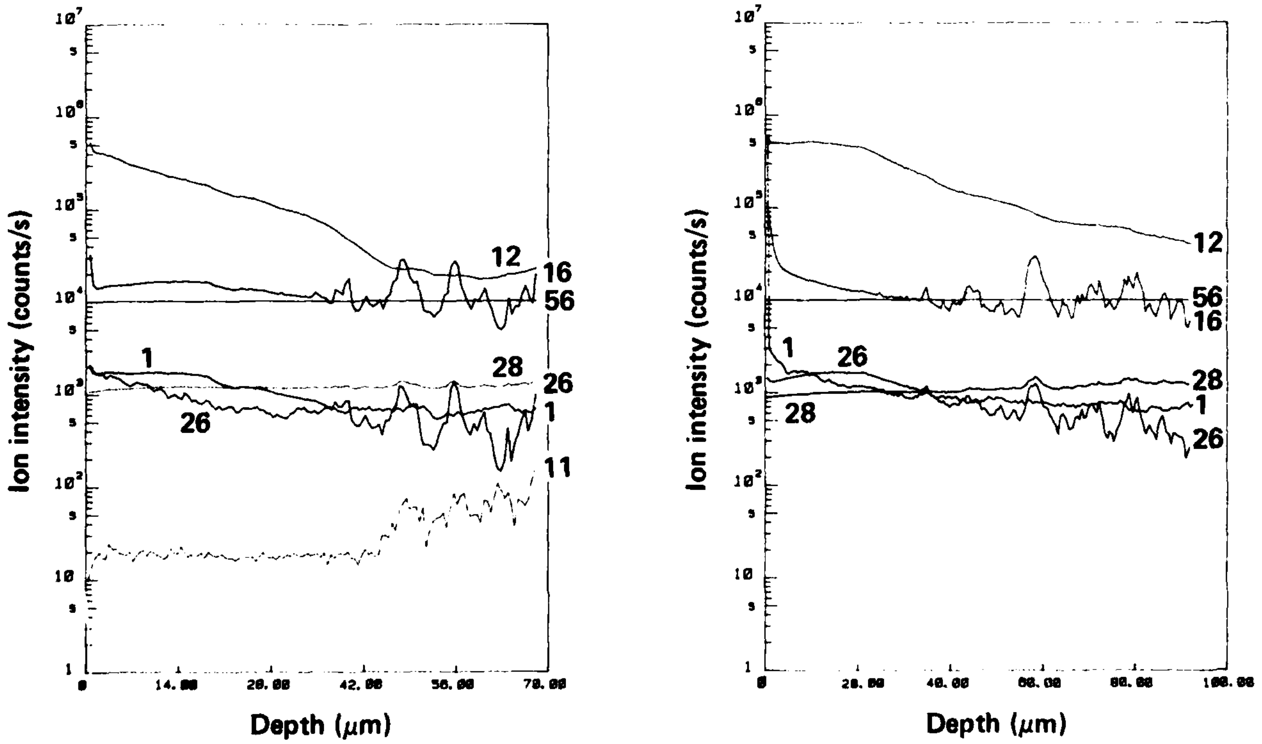

(a) 10 pulses.

(b) 50 pulses.

Fig. A3-2. SIMS depth profiles from iron specimens pulsed in 10% methane/argon.

Acknowledgments

This work was performed under the auspices of the U. S. Department of Energy by the Lawrence Livermore National Laboratory under Contract #W-7405-Eng-48 and supported by the U. S. Army Research Office (ARO) and U. S. Army ARRADCOM Laboratory, Dover, NJ, under Contract #15812-MS. The SIMS profiles were generated at Charles Evans and Associates (San Mateo, CA).

References

1. A. H. Cottrell, *Proc. Conf. Strength of Solids*, Bristol, 1948 (Physical Society, London, 1949), p. 30.
2. 2. F. R. N. Nabarro, *Proc. Conf. Strength of Solids*, Bristol, 1948 (Physical Society, London, 1949), p. 38.
3. A. H. Cottrell and B. A. Bilby, *Proc. Phys. Soc.* **A62**, 49 (1949).
4. J. P. Hirth and J. Lothe, *Theory of Dislocations* (McGraw-Hill, New York, 1968), p. 466–468, 584–633.
5. D. G. Brandon and J. Nutting, *J. Iron Steel Inst.* (London) **196**, 160 (1960).
6. W. Carrington, K. F. Hale, and D. McLean, *Proc. Roy. Soc.* (London) **A259**, 203 (1960).
7. A. S. Keh, *Direct Observations of Imperfections in Crystals*, J. B. Newkirk and J. H. Wernick, eds. (Interscience Publishers, New York-London, 1962), p. 213.
8. A. S. Keh and S. Weissmann, *Electron Microscopy and Strength of Crystals*, G. Thomas and J. Washburn, eds. (Interscience Publishers, New York-London, 1963), p. 231.
9. E. W. Johnson and M. L. Hill, *AIME Trans.* **218**, 1104 (1960).
10. C. A. Wert, *Phys. Rev.* **79**, 601 (1950).

Appendix 4

Dynamic Response of a Thin Disk Subjected to a Thermal Pulse

UCID-19448

DYNAMIC RESPONSE OF A THIN DISK SUBJECTED TO A THERMAL PULSE*

CLARENCE A. CALDER
Department of Mechanical Engineering
Oregon State University
Corvallis, OR 97331

RAY H. CORNELL
Mechanical Engineering·Department
Lawrence Livermore National Laboratory
Livermore, CA 94550

May, 1982

---

*Work performed under the auspices of the U.S. Department of Energy by Lawrence Livermore National Laboratory under contract #W-7405-Eng-48, and supported by the U.S. Army Research Office, Research Triangle Park, North Carolina under contract #15812-MS.

ABSTRACT

The dynamic response of a thin steel disk to a transient thermal pulse induced by a pulsed neodymium-glass laser was studied experimentally and compared with numerical results from a finite element code. The experiment was designed to provide data for use in code development work for erosion/corrosion studies.

INTRODUCTION

Material degradation due to erosion/corrosion processes occurring at very high temperatures and pressures (up to thousands of degrees K and hundreds of MPa) is a serious problem encountered in various applications of combustion. The metal and nonmetal surfaces containing the combustion in such applications as rocket nozzles, internal combustion engines, gas turbine combustors, and flow metering orifices degrade by material blow-off, fissuring, and other related mechanisms. The rate and degree of erosion and corrosion occurring is directly dependent on the combined effects of the heating and cooling rates, temperature peak, gases and particulates present, peak pressures, and the cycles of combustion to which the surface has been subjected. Due to the complexity and severe environment in which the erosion/corrosion phenomena occur, little experimental data are available for use in numerical code development work.

To provide data for modeling the fundamental mechanisms of erosion/corrosion, an approach using high energy pulsed laser deposition on various samples at differing levels of energy and in different atmospheres and pressures was considered. This relatively inexpensive method of testing can produce many of the relevant phenomena present by subjecting the sample to laser deposition through a transparent window of a pressure vessel container. The environment and pressure of the vessel can be easily changed and monitored to give desired test conditions. These tests would induce highly transient temperatures with possible melting and vaporization as well as the corresponding thermal stresses and chemical reactions at the specimen surface.

The purpose of this segment of the study was to evaluate a thin metal disk sample subjected to laser energy deposition as a suitable specimen geometry for providing usable data for the development of erosion/corrosion models to be used in numerical analysis.[1,2] The transient temperature, strain, and stress were measured using conventional transducers and the corresponding specimen surface degradation was studied. The transient response results were then compared with the predictions of a finite element code (DTVIS2) where the specimen was subjected to a transient energy flux input.

LASER-MATERIAL INTERACTION

Laser energy deposition will produce a thermal compressive stress on the deposition side of the disk sample. That is, the sudden heating causes the metal surface to want to expand but it is confined by surrounding unheated metal. At high laser pulse energies, specimen melt, vaporization, and momentum transfer due to the resulting blow-off are known to occur.[3,4]

In particular, earlier work has shown that compressive stress waves are induced in the sample when subjected to a Q-pulsed laser deposition with a pulse duration of about 30 nsec. Response to a much longer normal mode pulse (about 600 μsec) has not been as thoroughly studied but it would be expected to be more quasi-static in nature. Certainly, considerably more energy is available in the normal pulse mode of operation.

The surface degradation due to laser deposition will depend on the flux intensity, absorptivity of the surface, and the specimen environment. A range of flux intensities can be achieved by focusing or expanding the laser beam and by changing the laser beam energy. Successive depositions can be easily accomplished using repeated pulsing of the laser. As would be expected, increasing the pulse energy and the number of depositions will result in a corresponding increase in specimen surface damage. The laser-induced transient heating undertaken on various samples at suitable pressures and gaseous environments should provide meaningful data for computer model development.

TRANSIENT HEATING OF A THIN DISK

When one side of a thin disk specimen is suddenly heated, the induced compressive thermal stress causes an outward cupping of the disk. The opposite cooler side, curved inward, is correspondingly subjected to an initial compressive strain. As heat flows through the disk thickness and radially, a tensile thermal strain will result throughout. A strain gage mounted on the back side of the disk specimen will, therefore, respond to the suddenly increasing compressive strain which peaks at the end of the laser pulse. The gage output will then be decreasingly compressive and gradually go tensile as thermal equilibrium is established.

Whereas relatively slow surface heating would be expected to result in a quasi-static type response, the very rapid heating from a Q-pulsed laser configuration could excite vibrations in the disk corresponding to its fundamental natural frequency. A freely supported, circular disk will vibrate with a fundamental natural frequency in Hz given by[5]

$$f = \frac{1.45}{a^2}\sqrt{\frac{D}{\rho h}} \qquad \text{Eq. (1)}$$

where a = sample radius

D = flexural rigidity, $Eh^3/12(1-\nu^2)$

h = sample thickness

ρ = mass density

and E, ν are Young's modulus and Poisson's ratio.

When vibratory modes are excited by the laser heating, a strain gage mounted at the center of the rear face will detect the gross compressive strain level with a superposed oscillating strain having a frequency equal to that given by Eq. 1.

The transient response of the disk sample will also be affected by the speed of heat transmission through the sample. This is determined by the magnitude of the diffusivity of the sample material given by the relation

$$\alpha = \frac{k}{\rho c} \qquad \text{Eq. (2)}$$

where k = the conductivity

and c = the specific heat.

The time at which the back surface temperature has reached one-half the peak temperature amplitude can be shown to be

$$t_{1/2} = \frac{0.138\ h^2}{\alpha} \qquad \text{Eq. (3)}$$

A thermocouple attached at the back center of the specimen will give the temperature-time data from which $t_{1/2}$ can be measured and the value of determined.

EXPERIMENTAL ARRANGEMENT

Specimens for testing were fabricated from 4340 steel alloy and were 19 mm in diameter by 1.6 mm thick. Both surfaces were finished to a 600 grit. A neodymium-glass laser capable of a 10-15 Joule pulse in the Q-switched mode (30 nsec) and up to a 100 Joule pulse in the normal mode (600 μsec) was used. The 19 mm beam was directed through a glass beam-splitter sending a small portion of the output to a photodiode to provide a trigger pulse for the recording oscilloscope. The main beam then passed through a converging lens, an aperture, and was deposited on the specimen. The specimen had either a thermocouple, strain gage, or stress transducer mounted on its rear face and the corresponding output was fed into an oscilloscope. A schematic diagram of the test facility is shown in Fig. 1 with the sample located at the extreme left.

SAMPLE PROPERTIES

Samples for all tests were fabricated from 4340 alloy steel in the form of disks 19 mm in diameter by 1.6 mm thick. Table properties for the samples were taken to be:

$E = 200$ GPa

$\nu = 0.285$

$\rho = 7840\ \mathrm{kg/m^3}$

$k = 41.8\ \frac{\mathrm{W}}{\mathrm{m \cdot K}}$

$c = 502\ \frac{\mathrm{J}}{\mathrm{kg \cdot K}}$

For these values, Equations 1-3 give the fundamental frequency for a freely supported plate and the half-time back surface thermal response to be,

$f = 38{,}600$ Hz

and $t_{1/2} = 33$ msec.

TEST PROCEDURE

The 4340 steel disk samples were prepared for testing by attaching an intrinsically mounted thermocouple (type E, chromel-constantan), a 1.6 mm gage length semiconductor strain gage, or an ultrasonic transducer wrung on the rear surface using vacuum grease. The transient signals from the transducers were recorded on an oscilloscope simultaneously with the photodiode output of the laser pulse (used as a timing fiducial). The prepared sample was then carefully aligned with the high energy laser beam path using a helium-neon alignment laser. A focusing lens and aperture were used to give the desired intensity and spot size. (See Figure 2).

Tests were conducted by subjecting the sample to either a normal mode pulse of up to 100 Joules and 600 μsec duration or a Q-pulse of up to 15 Joules and 30 nsec duration. The sample was found to absorb only 20%-50% of the laser energy, the balance being reflected or blocked by the plume developed. Figure 3 shows a time integrated photograph of a normal mode deposition and illustrates the plume developed during the pulse. The sample was held in place by the three nylon supports shown. The laser beam does not appear in the photograph as the film is not sensitive to the 1.06 μm wavelength of the neodymium glass laser.

Tests were numerically modeled using a finite element code (DTVIS2) capable of dynamic response calculations with a specified thermal flux input. The 48 element grid layout is shown in Fig. 4 with deposition indicated over the central area of the sample. The flux-time variation given in Fig. 4 is for a normal mode pulse.

RESULTS AND DISCUSSION

Table I gives typical data from selected experimental and computational runs.

AD-A143 001 SIMULATIONS OF EROSION/CORROSION SURFACE CHEMICAL 2/2
REACTIONS WITH A LASER BEAM(U) LAWRENCE LIVERMORE
NATIONAL LAB CA C W PRICE 01 NOV 83 UCRL-53468
UNCLASSIFIED ARO-15812.7-MS MIPR-26-78 F/G 7/4 NL

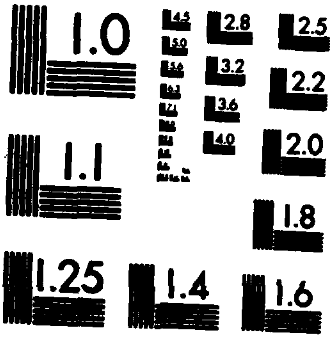

MICROCOPY RESOLUTION TEST CHART
NATIONAL BUREAU OF STANDARDS-1963-A

TABLE I

Selected Experimental (EXP) and Computational (COMP) Results

Run	Energy,J	Deposition Area	Rear ΔT,K	$t_{1/2}$,ms	Rad Strain	Vib Freq
EXP1	80	Full Face	21	33	-280 με	-----
EXP2	80	Center 6.3 mm	103	34	-460 με	-----
EXP3	80	Center 6.3 mm	---	--	------	38000 Hz
EXP4	40	Center 6.3 mm	79	33	-370 με	-----
EXP5	9 (Q)	Full Face	---	--	------	38500 Hz
COMP1	40	Full Face	22	36	-195 με	-----
COMP2	40	Center 6.3 mm	168	34	------	-----

Of particular note from the table is the excellent agreement between analysis, experiment and numerical results for the half-time temperature rise on the back face of the sample (about 33 msec). The rear surface temperature rise for a 40 Joule computational run (22K) was about the same as found experimentally for an 80 Joule input pulse (21K). This would indicate about 50% of the total energy was coupled into the specimen -- the balance being lost through reflection, vaporization, and blowoff. For these same deposition energies, the finite element run predicted a considerably larger back face temperature rise. This was due to extensive surface vaporization not accounted for in the numerical theory. The two runs showing induced vibration were also in close agreement with the analytical calculation of fundamental plate frequency of 38,600 Hz. The vibration was excited by a normal mode, 80 Joule pulse in one run and by a Q-pulse mode, 9 Joule pulse in another run.

Rear surface thermocouple temperature measurements for normal mode deposition showed rapid temperature rise to a peak temperature occurring at about 80 msec. Subsequent decay to room temperature due to thermal equilibrium and heat transfer from the sample occurred by 2-3 seconds after pulse time. As would be expected, much higher peak temperature was reached for the focused beam. Temperature history is shown in Fig. 5 and compared to predictions of the finite element code. Quite good agreement is indicated with the $t_{1/2}$ values essentially the same. Successive shots on the same disk typically showed progressive increases in the peak temperature due to increased absorptivity. For example, tests at 80 Joules focused to a 6.3 mm diameter gave a 40 K temperature rise on the first shot and a 93 K rise on the tenth shot. This is due to oxidation of the deposition area as later testing (not reported here) in an inert or evacuated environment showed little change in absorptivity and the corresponding peak temperature rise between the first and tenth shot.

Strain histories were recorded for both 600 μsec and 30 nsec pulses. The response to the focused normal mode pulse showed an immediate compressive strain which peaked shortly after the end of the laser pulse (about 1 msec) and then decayed to zero strain as temperature equilibrium was reached. However, in all cases the gage output returned compressive rather than going tensile as expected from the final thermoelastic tensile strain. This result was apparently due to thermal effects on the semiconductor strain gage as the higher temperatures reached the back face. The computer code predicted the expected strain history with initial compressive strain followed by decay and a subsequent tensile strain. The deformed shape history for the disk subjected to a central flux with energy of 40 Joules and duration of 600 μsec is shown in Fig. 6. The series of disk profiles show a maximum cupping shape at 600 μsec with the disk nearly flat again by two seconds.

Although plate vibrations were not readily evident for normal mode tests, appropriate signal amplification and low frequency filtering produced a superposed high frequency signal of about 38,000 Hz - the fundamental natural frequency of the plate. Similar testing in the Q-switched mode excited strong vibration at the fundamental frequency. This is illustrated in Fig. 7 at two sweep rates with the expanded rates given at the beginning (A) and at 540 μsec after deposition (B). Fig. 7A shows a superposed higher mode of vibration present. This higher mode has damped out by the time of the Fig. 7B trace.

Three types of piezoelectric stress gages were mounted to the back face of the sample by wringing them on, using vacuum grease. The configuration was then subjected to a 40 Joule, 600 μsec pulse (see Fig. 8) and the output recorded. Although ultrasonic transducers in general do not give a true history of the actual transient stress, all three transducers used indicated a compressive stress state generated during the laser pulse duration. The trace data for a one-inch diameter, five MHz commercial transducer is shown in Fig. 9.

CONCLUSIONS

The general dynamic behavior of a thin disk subjected to a laser energy deposition pulse can be described in terms of its thermal and mechanical response. The thermal response can be accurately predicted using an analytical half-time temperature relation or a finite element thermoelastic code. Strain gage response is valid until heat transmission through the sample thickness affects the gage output. Laser deposition can excite the fundamental mode of plate vibration - especially when subjected to a Q-switched pulse. With the dynamic response of the thin disk reasonably well understood, this sample configuration should be a suitable form for erosion/corrosion testing using laser energy disposition.

ACKNOWLEDGEMENT

The authors wish to acknowledge guidance provided through technical discussions with A. Buckingham and A. Goldberg during the course of this study. We are also grateful to G. Carter for his assistance with the experiments and operation of the laser system.

REFERENCES:

1. A. C. Buckingham, et. al., "Investigation of the Fundamental Mechanisms of Hot Flow, Multi-Phase Erosion/Corrosion", Lawrence Livermore National Laboratory, LLL-Prop. 150, March 1977.

2. A. Goldberg and R. H. Cornell, "Pulsed-Laser Heating -- a Tool for Studying Degradation of Materials Subjected to Repeated High Temperature Excursions", Lawrence Livermore National Laboratory, UCRL-53074, August 1980.

3. C. A. Calder and W. W. Wilcox, "Noncontact Material Testing Using Laser Energy Deposition and Interferometry", Materials Evaluation, V 38:1, January 1980, pp. 86-91.

4. C. A. Calder and W. W. Wilcox, "High Temperature Noncontact Material Testing", Characterization of Materials for Service at Elevated Temperature, G.V. Smith, Ed., ASME Series MPC-7, 1978, pp. 169-181.

5. S. Timenshenko, et. al., Vibration Problems In Engineering, 4th Edition, John Wiley, 1974, pg. 497.

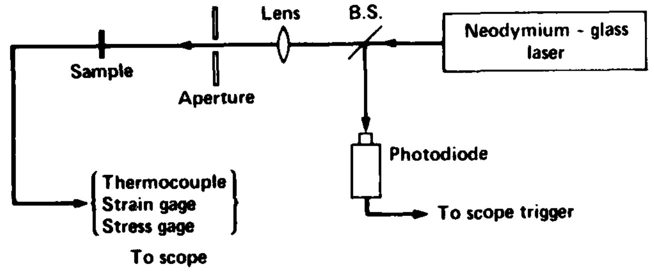

Fig. 1. Schematic diagram for pulsed laser deposition experiments.

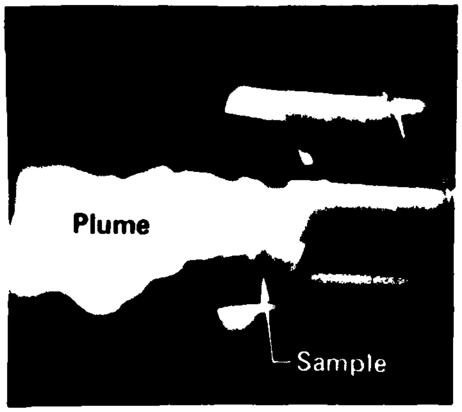

Fig. 2. Time-integrated photo showing plume.

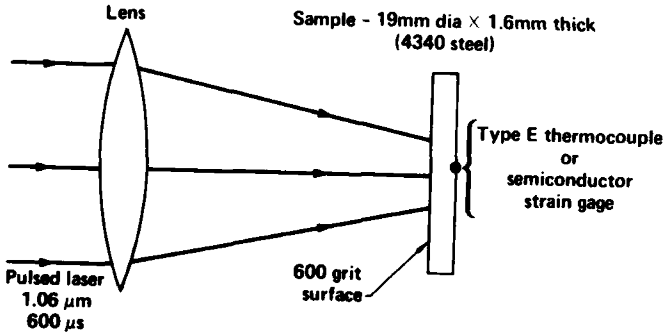

Fig. 3. Specimen configuration for laser deposition experiments.

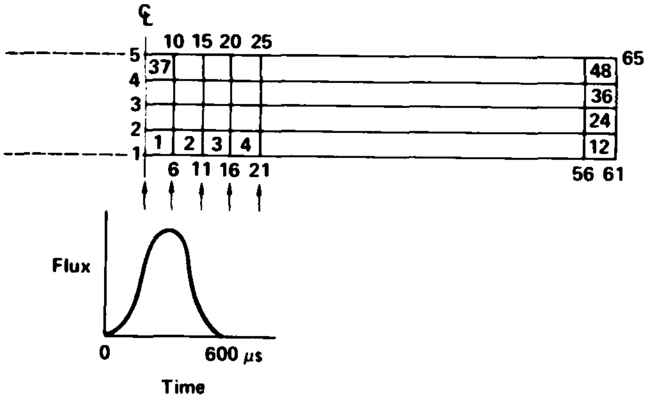

Fig. 4. Finite element mesh showing normal mode thermal flux.

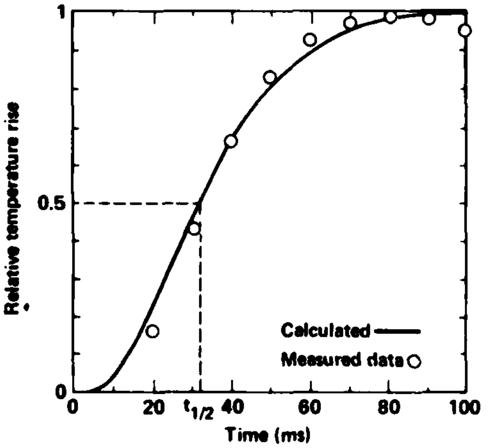

Fig. 5. Back surface temperature history comparing experimental measurements with finite element prediction.

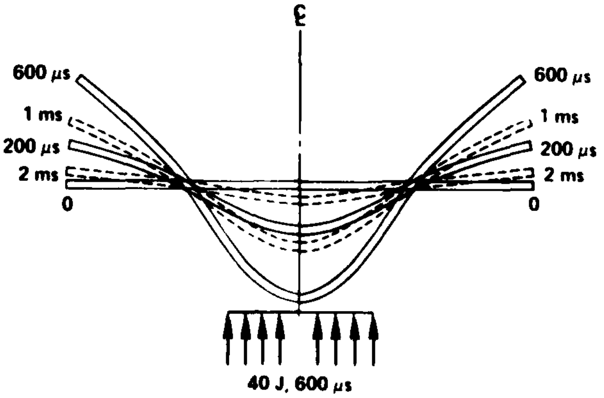

Fig. 6. Magnified deformed shape histories predicted by finite element code.

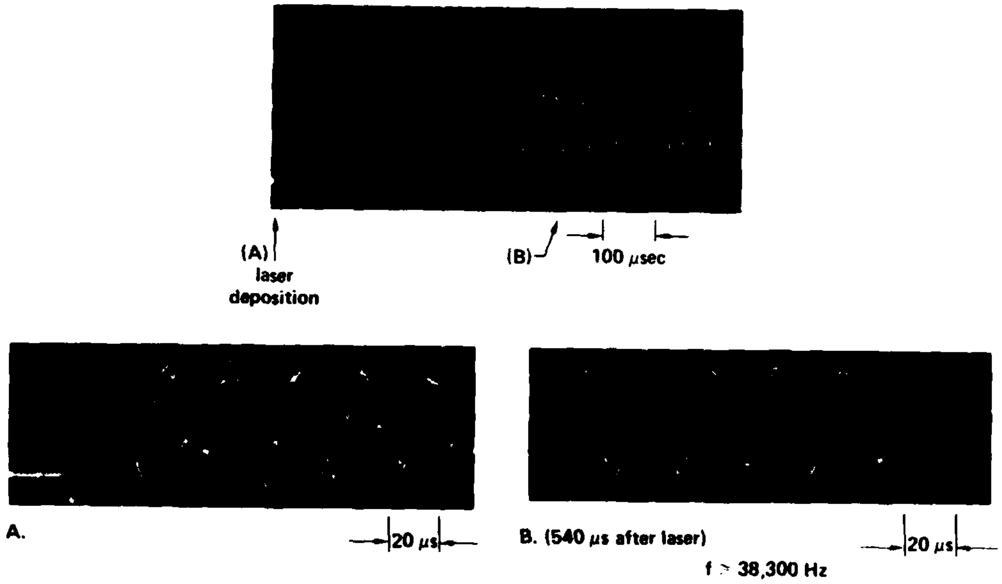

Fig. 7. Disk back-surface strain response to Q-switched laser deposition on full face of specimen.

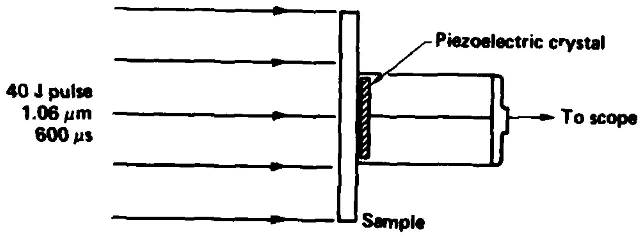

Fig. 8. Stress gage test configuration.

Fig. 9. Signal from piezoelectric ultrasonic stress gage resulting from normal mode laser deposition.

Appendix 5
Application of Dislocation Dynamics to Erosion/Corrosion

One of the mechanisms of primary concern in erosion/corrosion is plastic deformation, particularly as a precursor to crack initiation and subsequent material loss. The purpose of this appendix is to discuss a simplified dislocation dynamics approach for the simulation of plastic deformation that occurs during erosion/corrosion. Other constitutive treatments of plastic deformation such as the phenomenological approach developed by Hart,[1] empirical approaches,[2] or other dislocation models[3] may be considered for modelling plastic deformation in erosion/corrosion reactions, but the dislocation dynamics approach was selected for this discussion because of its more explicit incorporation of material parameters. The objective of this discussion is to indicate how various material parameters may interact during erosion/corrosion, how they may be modified by surface chemical reactions in a reactive environment, and the type of data that must be generated by experiment.

One of the first constitutive relations based on dislocation dynamics for the plastic strain rate of materials was developed by Johnston and Gilman.[4] They related the plastic strain rate of a crystal to the strength or Burgers vector of a dislocation, the number of mobile dislocations, and the average velocity of dislocations:

$$\dot{\epsilon}^P = b\, n\, v \tag{1}$$

$\dot{\epsilon}^P$ = plastic strain rate
b = Burgers vector
n = number of glissile dislocations per unit area
v = average dislocation velocity

Johnston and Gilman also suggested that edge and screw components of dislocations should be treated separately since edge dislocations are more mobile than screw dislocations. Their relation neglected work hardening. Gillis[5] used a modified Johnston-Gilman relation that included work hardening terms:

$$\dot{\epsilon}^P = \Phi\, b(\rho_0 + \alpha\, \epsilon^P)\, v^*\, \exp\,(-D^*/\tau) \tag{2}$$

Φ = orientation factor
ρ_0 = initial dislocation density
α = dislocation multiplication coefficient
ϵ^P = plastic strain
v^* = apparent limiting dislocation velocity
D^* = characteristic drag stress
τ = maximum shear stress

The form of the dislocation drag stress term was proposed to be:

$$D^* = D_0^* + H^* \epsilon^P \tag{3}$$

D_0^* = constant
H^* = strain hardening coefficient

This relation provided reasonable agreement with the experimental Hugoniot elastic limit determined for tantalum specimens that had been impacted with a gas propellent gun. The general form of Eq. (2) is frequently used in dislocation dynamics, although the individual terms still are subject to much debate.[6,7]

Thermal effects can be included in Eq. (2) by substituting a frequency factor and an Arrhenius term as discussed by Conrad[8]:

$$v^* = \nu\, \exp\,[-Q(\sigma)/kT] \tag{4}$$

ν = frequency factor
$Q(\sigma)$ = activation energy
k = Boltzmann constant
T = absolute temperature

The activation energy $Q(\sigma)$ decreases with the applied stress σ. The drag stress term, D^*, can include the concept of activation area. Properties which affect plastic deformation such as stacking fault energy for fcc materials usually are incorporated in α, D^*, and possibly v^*. Chemical effects which occur with erosion/corrosion as discussed in Appendix 1 will modify the dislocation multiplication coefficient, α, and the drag stress terms, D_0^* and H^*. For example, hydrogen in steel may decrease D^* and increase α, whereas carbon and nitrogen in solution can form Cottrell atmospheres which decrease D^* until dislocation breakaway occurs (i.e., serrated yielding). Other factors such as the Hall-Petch grain-size effect could be included in α and H^*.

Grain-boundary sliding often contributes to plastic deformation, particularly at elevated temperatures. Grain-boundary sliding can be incorporated in Eq. (2) by considering plastic strain to be a function of the normal plastic strain in the bulk lattice plus the grain-boundary contribution, composed of a grain-boundary sliding term and an interaction term:

$$\epsilon^P = f(\epsilon_b, \epsilon_g, \epsilon_a) \tag{5}$$

ϵ_b = bulk plastic strain
ϵ_g = grain-boundary sliding
ϵ_a = interaction term

The interaction term includes contributions such as the generation of bulk dislocations to accommodate nonconservative gliding of grain-boundary dislocations (GBDs) which occurs along curved grain boundaries at grain-boundary junctions. Since grain-boundary sliding is related to the glide of GBDs along the grain boundaries at low and moderate temperatures, the various terms in Eq. (2) should be modified to include the properties of GBDs and appropriately weighted for the relative contributions of bulk dislocations and GBDs. The terms for GBDs will be affected in ways similar to those already discussed for bulk dislocations. The collective treatment of bulk dislocations and GBDs should properly reflect the dominant deformation mechanisms that operate. This is analogous to the deformation mechanism maps developed by Ashby.[9]

Diffusional flow can be an important contribution to grain-boundary sliding for temperatures in excess of 0.85 T_m (T_m = melting point), as indicated by Ashby's deformation mechanism maps. This could require either separate treatments as used by Ashby or the addition of terms to Eq. (2) for Cobble and Nabarro-Herring creep. However, these mechanisms may not be dominant within the short time frame of the transient response of concern in this program, and additional terms may not be required for mathematical simulations. Nonetheless, they demonstrate the flexibility and versatility that this approach could have.

The application of Eq. (2) to erosion/corrosion will require a finite difference technique to properly compensate for the transient fluctuations that occur in stress, temperature, and chemical composition during a pulse. The pulse could be divided into finite time increments. The stress and temperature at each point in the modelled specimen would be estimated at the beginning of each time increment. Both experimental data reduced from experiments such as those conducted in this program and finite element computations of stress and temperature distributions could be used for the estimates.

Because of the sensitivity of Eq. (2) and, hence, erosion/corrosion response to chemical composition, proper treatment must be accorded to compositional fluctuations induced by surface chemical reactions during erosion/corrosion. Enhanced diffusional flow of surface reaction products into the specimen is expected to occur during erosion/corrosion and significantly affect the resultant composition gradient. Therefore, additional mechanisms that must be considered are (a) excess vacancy production caused by both the effect of thermal pulsing on the equilibrium vacancy distribution and nonconservative dislocation glide during plastic deformation, (b) dislocation drag of impurities by gliding dislocations, and (c) pipe diffusion down the cores of the large numbers of dislocations that are generated during each pulse.

Obviously, detailed analyses of experimental data will be required to affix proper values to the various terms in Eq. (2). Once these values are established at the beginning of a time increment, the strain that occurs during the increment could be computed from the integration of Eq. (2) over the interval of the increment. The values of the terms in Eq. (2) could then be recalculated and set for the next time increment. The program would be reiterated for the required number of time increments to correspond to the effective pulse time (i.e., from the time the pulse is initiated to the time that plastic deformation and diffusional flow become minimal during cooling).

For repetitive pulsing, both the dislocation distribution and the composition gradient (i.e., the concurrent accumulation of damage and reaction products in a real specimens) accumulated at the end of the previous pulse simulation would be called from storage to reset the starting values for the terms in Eq. (2), and the next pulse would be simulated. The program would be repeated for the desired number of pulses. If required, the terms could be modified for post-pulse annealing effects such as dislocation annihilation or even recrystallization.

Alternate deformation and fracture mechanisms may become important as damage accrues. At elevated temperatures, for example, high carbon and nitrogen contents could occur along the grain boundaries as a result of preferential grain-boundary diffusion. When the carbon and nitrogen contents become sufficiently high, adiabatic grain-boundary sliding could induce incipient melting along the grain boundaries. This would be similar to liquid-metal embrittlement and could constitute an important mechanism for erosion/corrosion material loss. This mechanism would be accelerated by deleterious impurities such as sulfur, arsenic, antimony, bismuth, etc. The dislocation dynamics approach outlined in this appendix could predict the amount of plastic deformation and the compositional change required to cause crack initiation. A crack growth model could then be developed to predict erosion/corrosion material loss.

We wish to emphasize that this model has been discussed in detail to demonstrate the complex interaction of various material parameters in erosion/corrosion. This program has progressed to the point where such a model could be developed.

References

1. E. W. Hart, *Acta Metall.* **15**, 351 (1967).
2. M. E. Kassner, A. K. Miller, and O. D. Sherby, *Metall. Trans.* **13A**, 1977 (1982).
3. W. G. Hoover, *Dislocation Motion and Plastic Flow*, Lawrence Livermore National Laboratory, Livermore, California, UCRL-50028-788-3 (1978), pp. 26–27.
4. W. G. Johnston and J. J. Gilman, *J. Appl. Phys.* **30**, 129 (1959).
5. P. P. Gillis, *J. Appl. Phys.* **42**, 2145 (1971).
6. U. F. Kocks, A. S. Argon, and M. F. Ashby, *Prog. Mater. Sci.* **19**, (1975).
7. U. F. Kocks and H. Mecking, in *Dislocation Modelling of Physical Systems*, M. F. Ashby, R. Bullough, C. S. Hartley, and J. P. Hirth, eds. (Pergamon Press, Oxford and New York, 1981), p. 173.
8. H. Conrad, *J. Metals* **16**, 582 (1964).
9. M. F. Ashby, *Acta Metall.* **20**, 887 (1972).

U.S. Government Printing Office: 1984/4-787-002/A4036

END

FILMED

8 [illegible]

DTIC